A Systematic Investigation on Piezoelectric Energy Harvesting with Emphasis on Interface Circuits

LIANG, Junrui

A Thesis Submitted in Partial Fulfilment
of the Requirements for the Degree of
Doctor of Philosophy
in
Mechanical and Automation Engineering

The Chinese University of Hong Kong

September 2010

ProQuest LLC.
789 East Eisenhower Parkway
P.O. Box 1346
Ann Arbor, MI 48106 - 1346

Thesis/Assessment Committee

Professor HUANG, Jie (Chair)

Professor LIAO, Wei-Hsin (Thesis Supervisor)

Professor LIU, Yunhui (Committee Member)

Professor SHU, Yi-Chung (External Examiner)

論文評審委員會

黃捷 教授 （主席）

廖維新 教授 （論文導師）

劉雲輝 教授 （委員）

舒貽忠 教授 （校外委員）

Abstract

Owing to the great reduction on power consumption of integrated circuits (ICs) and miniaturization during the past decades, the energy harvesting technique has gained much interest recently with the inspiration that more devices in wireless sensor networks as well as mobile electronics could power themselves by scavenging the ambient energy in different forms. Piezoelectric energy harvesting (PEH) is one of the most widely studied techniques to scavenge energy from ambient vibration sources. With the electromechanical nature, a PEH device can be divided into mechanical and electrical parts. The two parts are linked by the piezoelectric transducer. Literatures on PEH are reviewed and discussed. In the research of PEH, generally there are four different research foci on: mechanical part, electrical part, piezoelectric transduction, and system.

This thesis provides new insight into the research of piezoelectric energy harvesting from some systematic viewpoints. The modeling process of a single degree-of-freedom (SDOF) PEH system is firstly discussed. It shows how the model of a PEH device is built from the material level to element level, and then to device level. In the systematic analysis to PEH devices, the energy flow and impedance based analysis are highlighted. A detailed analysis on the energy flow within the PEH system provides good understanding on the system. However, up to now, most of the researches on PEH have been mainly concerned with the absolute amount of energy that can be harvested from vibrating structures; the detailed energy flow within the system as well as its effect on the vibrating structure, were seldom discussed. By studying the energy flow within three applications of standard energy harvesting (SEH), resistive shunt damping (RSD), and synchronized switching harvesting on inductor (SSHI), it can be concluded that, in a PEH system, the two functions of energy

harvesting and dissipation are coexistent. Both of them bring out structural damping. New factors are defined to give a more comprehensive evaluation on the energy flow in PEH systems.

To enhance the harvesting power by using the impedance matching is not new; yet, previous literatures on impedance matching for PEH oversimplified the problem. Without clarification on the energy flow in the PEH system, their objectives on power optimization were ambiguous. Some literatures even assumed that the harvesting interfaces, which are nonlinear in nature, can be equalized to linear loads, and the load impedance can be arbitrarily set. With the understanding on energy flow within piezoelectric devices, we clarify the objective of impedance matching, and further demonstrate that the range of equivalent impedance of existing harvesting interfaces is in fact constrained, rather than unlimited. The analyses on system level provide guideline to improve the harvesting performances. Improvements can be made with innovative designs in either mechanical configuration, piezoelectric transducer, or interface circuit.

Besides system level analyses, some implementation issues on switching interface circuits are also investigated. These interfaces show a great potential on harvesting efficiency improvement. Based on the experimental observation, it is found that there is a voltage reversion after every inversion in SSHI, which weakens the harvesting performance. This influence is caused by the dielectric loss in piezoelectric material. A revised model as well as detailed analysis are proposed to evaluate the influence of dielectric loss over the harvesting power degradation.

Considering the practical implementation, a modified self-powered switching interface circuit is proposed. It can achieve better isolation among components and involve less dissipative components. Improved analysis on this self-powered switching interface circuit is also provided. It is shown that the higher the excitation level, the more beneficial for replacing the SEH interface with the self-powered switching interface; meanwhile, the closer between the performances of self-powered and ideal (external powered) switching interfaces.

摘　要

近十年來，隨著集成電路對功耗的要求不斷降低與電子設備的微型化，使得通過收集環境中的能量為一些低功耗的無綫傳感器和便攜式電子裝置供電變得可能。各種形式的能量收集技術吸引了人們的廣泛關注。壓電能量收集技術被深入研究用於收集環境中的振動能量。作爲一個機電系統，壓電能量收集裝置可以被分解為機械和電氣兩個部分。這兩部分通過壓電換能器連接起來。通過對關於壓電能量收集的文獻進行回顧和整理，可以概括出四個研究重點：機械部分，電氣部分，壓電換能器，和系統的視角。

本論文從系統的角度出發，提出了一些對壓電能量收集的新見解。文中首先討論了對壓電能量收集系統的單自由度近似，以及如何從材料的本構方程得到壓電器件模型，進而得到壓電裝置的模型。在對壓電能量收集裝置的系統分析當中，本論文突出了能量流的概念和基於阻抗的分析方法。對壓電能量收集裝置中能量流的仔細分析有利於對整個能量收集裝置的根本認識。然而，迄今爲止，大部分關於壓電能量收集的文獻把注意力集中在收集的絕對能量上。系統中能量流動的細節以及能量收集對振動結構的影響很少得到討論。經過對標準能量收集（SEH）、壓電分流減振（RSD）、電感同步開關收集（SSHI）三種壓電設備中能量流的分析發現，在一個能量收集系統當中，能量回收和消耗兩者會共同存在，它們的共同效應體現為對結構的減振作用。爲了對能量收集系統中的能量流進行綜合評價，文中定義了新的評價因子。

在本論文之前，有個別文獻提出使用阻抗匹配的原理對收集功率進行優化。然而，這些文獻都將能量收集界面電路過度簡化了。由於缺乏對壓電能量收集系統中能量流的全面理解，他們未能清晰地給出在能量收集系統當中功率優化的確切目標。一些文獻甚至假設非綫性的收集界面電路可以等效為阻抗值可以任意指定的綫

性負載。基於對壓電設備中能量流的認識，阻抗匹配的目標得到澄清。進一步的分析指出，現有收集界面電路的等效阻抗是受約束的，並非可以任意選取的。從系統角度出發的分析對改進能量收集系統的收集性能具有指導意義。收集系統的性能可以通過對機械結構，壓電換能器，以及界面電路三方面的合理設計得到提升。

除了在系統的層面分析壓電能量收集系統，本論文亦探討了開關界面電路的一些實施細節。採用這些界面電路可以大大提升能量收集的效率。在電感同步開關收集界面的實驗中，一個輕微的電壓逆轉被發現總是跟隨在每次的電壓翻轉之後。這一小逆轉削弱了能量收集的性能。通過分析，這一現象歸因於壓電材料的介電損失。爲了評估介電損失對收集功率的影響，本論文給出了修正的模型和詳細的分析。

考慮到在實際收集系統中的應用，本論文提出了一個改進的自供電開關界面電路。這一電路更好地隔離了電路中不同器件的干擾，而且減少了使用帶來損耗的電阻器件。對此自供電開關界面的分析表明，激勵幅度越大，相比于標準收集界面，使用此自供電開關界面將會收到越好的效果；同時，自供電電路在收集性能上的表現也會更接近于理想（外部供電）的開關界面電路。

Acknowledgements

I would like to give my sincere appreciation to Professor Wei-Hsin Liao, my thesis supervisor, for his enlightenment, encouragement, and support over these years. I am also very grateful to Professor Jie Huang, Professor Yun-Hui Liu, and Professor Yi-Chung Shu for serving as my committee members and providing comments on this research. Thanks are due to all SMS Lab members for their valuable comments and discussions throughout these years.

I also thank my family, relatives and friends for their love as well as understanding and encouragement on my study and work. Finally, I appreciate my hometown Shunde in Guangdong Province for her motto to all her offsprings, "Once say yes, then do your best; If unfortunately fail, don't be overwhelmed."

致　謝

首先由衷的感谢導師廖維新教授在這些年來對我的啓蒙，鼓勵與支持。感謝黃捷教授，劉雲輝教授和舒貽忠教授在百忙中撥冗參加我的答辯並對此研究給予寶貴的意見。這些年在香港中文大學智能材料與結構實驗室學習，做研究，在與各位成員的討論交流中獲益良多，在此一併致谢。

研究以外，感謝我的家人與眾親朋好友對我的關愛以及對我的學業和工作的理解與支持。最後，想起我的家鄉，以及每個順德人都熟知那句話，"話得就係一定得，唔得可以返順德"。她的精神一直勉勵著我踏實並竭盡所能地走好每一步。

Table of Contents

List of Figures

List of Tables

Chapter 1

Introduction

1.1 Background

The technologies of *energy harvesting* (also known as *power harvesting* and *energy scavenging*) provide the possibility that ambient energy in different forms is converted, captured and stored (usually in electrical energy). The most investigated ambient energy sources include solar energy, kinetic energy, thermal energy, and RF radiation (Mateu and Moll, 2005; Thomas et al., 2006; Penella and Gasulla, 2007; Cook-Chennault et al., 2008; Hudak and Amatucci, 2008; CATRENE, 2009). The scattering nature of ambient sources makes the energy harvesting systems different from the conventional centralized power generations. These harvesting systems are more suitable to be equipped as the power supplies in low power wireless autonomous devices. Ubiquitous deployed *wireless sensor networks* (WSNs) (Gilbert and Balouchi, 2008; Mathuna et al., 2008; Bogue, 2009; Op het Veld et al., 2009) and *portable electronics* (Paradiso and Starner, 2005; Mitcheson et al., 2008; Cook-Chennault et al., 2008; Jia and Liu, 2009) are the most potential applications which might gain benefit from the development of energy harvesting technologies.

Conventionally, the devices in both categories of WSNs and portable electronics are powered by batteries. Because of the limitation on battery energy density, the use of batteries in these devices restricts their lifetime. For WSNs, short lifetime nodes require frequent battery replacements, which might increase the maintenance cost; while for portable electronics, the mobilities of the devices are constrained by the batteries' lifetime. The emergence of the energy harvesting technologies provides various approaches to alleviate the devices' dependence on batteries, or even get rid of them. Yet, there is still some gap between the power requirement and generation capability. The average power consumptions

of commercial WSN nodes are around several mW to tens of mW (Gilbert and Balouchi, 2008); while those of portable devices are larger, from tens of mW to several W (Jia and Liu, 2009). On the other hand, the generated power in most energy harvesting systems are at μW to mW levels (Beeby et al., 2006; Hudak and Amatucci, 2008). Therefore, up to now, only a few of wireless autonomous devices are able to be fully powered with the energy that is harvested from ambience. Yole Development, a market research and business development consulting company in France, proposed a market report on energy harvesting devices in 2009 (Hamza and Robin, 2009). They have surveyed the development status of 44 groups in vibration and thin film thermal energy harvesting. According to their report, out of the 44 groups, only eight of them were in production. The technologies of these eight groups were all in vibration energy harvesting (five piezoelectric and three electromagnetic). Other groups were all under the status of small production, or R&D. Further research and development on different harvesting technologies as well as low power electronics can help to narrow the gap between the power requirement of end-devices and the supply capability of harvesting systems. In the research of energy harvesting, two orientations are usually highlighted, i.e., miniaturization (Beeby et al., 2006; Arnold, 2007; Cook-Chennault et al., 2008; Hudak and Amatucci, 2008; Hamza and Robin, 2009) and human-powered mechanism (Starner, 1996; Mitcheson et al., 2008; Jia and Liu, 2009). These two orientations are closely related to the target applications in WSNs and portable electronics.

Mechanical movement or vibration can be found everywhere in our daily life. It is one of the promising ambient sources to be exploited (Sodano, Inman and Park, 2004; Beeby et al., 2006; Arnold, 2007; Anton and Sodano, 2007; Priya, 2007; Khaligh et al., 2010; Rodig et al., 2010). Generally speaking, any electromechanical transducer can be utilized to harvest vibration energy; but three transduction mechanisms, i.e., piezoelectric, electromagnetic, and electrostatic, are most studied. Among generators based on these three mechanisms, the piezoelectric ones (Sodano, Inman and Park, 2004; Anton and Sodano, 2007; Priya, 2007; Khaligh et al., 2010; Rodig et al., 2010) are the simplest to fabricate; therefore, they are particularly suitable for implementation in microsystems (Beeby et al., 2006). In addition, Mitcheson et al. (2007) analyzed the performance limits of the three transduction mecha-

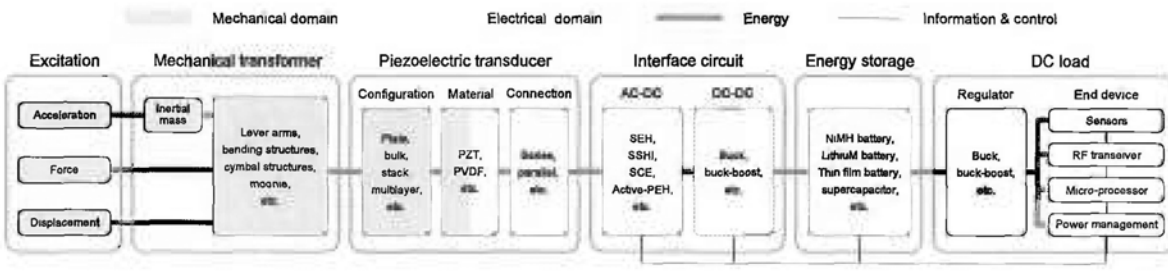

Figure 1.1: Block diagram of a piezoelectric energy harvesting system.

nisms. They found that, in micro-electro-mechanical system (MEMS) scale, piezoelectric generators outperform electromagnetic generators at low frequency; therefore, might be better suited to human-powered applications. According to the market research report from Yole Development (Hamza and Robin, 2009), within the 44 companies they have surveyed, nearly half of them (21 out of 44) focused on piezoelectric energy harvesting (PEH). This number is approximately two times of the electromagnetic ones, three times of the electrostatic ones, and four times of the thin film thermoeletric ones.

1.2 System Overview

From the application point of view, a complete PEH system is broken down into six parts: excitation and mechanical transformer fully in mechanical domain; piezoelectric transducer in half mechanical and half electrical domain; interface circuit, energy storage, and DC load fully in electrical domain. The block diagram of a typical PEH system is shown in Figure 1.1. The piezoelectric transducer is the key component in the harvesting system. It links the mechanical and electrical domains with its piezoelectric effect, which produces electric potential when stress is applied.

For example, Figure 1.2 shows the configuration of a base excited PEH device. Referring to the block diagram in Figure 1.1, the base acceleration $\ddot{y}(t)$, second derivative of the base displacement $y(t)$, is the mechanical excitation. Through mechanical transformation mechanisms (the inertial mass M and the bending cantilever), the base vibration is transformed

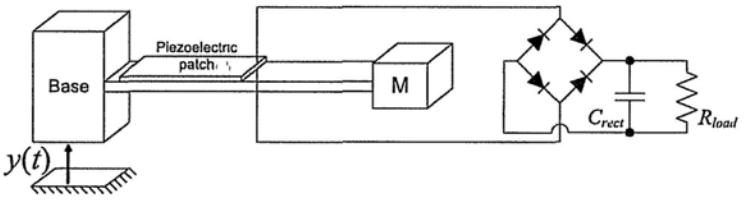

Figure 1.2: A base excited piezoelectric energy harvesting device.

Table 1.1: Components in the base excited PEH device and their corresponding blocks

Component	**Corresponding block**
Base acceleration $\ddot{y}(t)$	Excitation
Mass M and bending cantilever	Mechanical transformer
Piezoelectric patch	Piezoelectric transducer
Bridge rectifier	Interface circuit
Filter capacitor C_{rect}	Energy storage
Resistor R_{load}	DC load

into alternating longitudinal deformation of the piezoelectric patch. Due to the piezoelectric effect, a charge movement is then induced across the element. As far as the end devices are usually digital electronics, which require DC voltage power supply, an interface circuit is followed for AC-DC rectification. The device in Figure 1.2 adopts a bridge rectifier for rectification. It is the most standard interface circuit, which is called standard energy harvesting (SEH) interface in the following chapters of this thesis. The filter capacitor C_{rect} acts as the energy storage; while R_{load} represents the DC load. Table 1.1 summarizes the corresponding relation between the components in the base excited PEH example and the blocks in the block diagram.

For a practical self-powered device, some sub-blocks should be added for harvesting control and power management. The DC-DC sub-block in the interface circuit is selectable. It adapts the harvesting condition by tuning its input DC voltage, which was shown to be

related with the harvesting efficiency (Ottman et al., 2002, 2003). The regulator in the DC load block provides constant output voltage to the following digital electronic components, e.g., micro-processer and RF module. Some of these control and management need to be carried out by the end device.

The block diagram provides an overview to the composition of a PEH device. Every block is crucial towards the implementation of the harvesting device. Based on this overview, we can study the roles of different parts in the research of PEH, as well as further discuss the challenges and opportunities we are facing.

1.3 Literature Review

The research on PEH is multidisciplinary. The researchers working in this field are from diverse disciplines, mainly electrical, mechanical and material engineering. Different people with different backgrounds might put different emphases in their research. Summarizing most of the previous literatures, their emphases were mainly focused on four aspects: the mechanical part, the electrical part, the transducer, and the whole electromechanical system.

1.3.1 Mechanical part emphases

According to Figure 1.1, the excitation, mechanical transformer, and a portion of the piezoelectric transducer are included in mechanical domain. A mechanical configuration should be elaborately designed to:

a) respond to the specified excitation, which might input in different means, e.g., impact, harmonic, or human motion;
b) better transform the excitation energy into strain energy, which is input to the piezoelectric transducer [1].

[1] In this thesis, the verb "transform" specify the energy transfer within one domain; while the verb "transduce" refers to the energy transfer from one domain to another domain.

The design of PEH devices subjects to the excitation patterns in specific applications. Various sophisticated mechanical configurations as well as their corresponding analyses were proposed for the purpose of harvesting energy under different excitations.

Impact excited devices

The earliest investigation to harvest energy from mechanical impacts using piezoelectric materials was introduced by Umeda et al. (1996). In their study, they dropped a 5.5 g steel ball at the height of 20 mm onto a piezoelectric structure. The piezoelectric structure is composed of a bronze disk in 27 mm diameter and piezo-ceramics in 19 mm diameter (both thicknesses are 0.25 mm). The harvesting energy was estimated by directly connecting a resistor to the piezoelectric element as AC load. A maximum 10% harvesting efficiency was achieved in their experiment by tuning the load resistor. Later work involved the standard AC-DC interface for energy collection (Umeda et al., 1997). Results showed that the harvesting efficiency is greatly related to the initial rectified voltage.

Renaud et al. (2007) considered the energy harvesting of a unimorph bending cantilever under shock and impact excitation; and later designed an impact-based PEH device to harvest energy from the motion of human limbs (Renaud et al., 2009). When the device is shacked along with the limb movement, a free moving object within the housing is guided to hit two piezoelectric cantilevers alternately, so as to excite the natural vibration of cantilevers. Experiments showed that the harvesting power is around several hundred μJ and the conversion efficiency is around 10%.

Guigon et al. (2008*a*,*b*) investigated the possibility to harvest energy from rain drops using PVDF polymers, which is also an impact excited case. In their experiment, they harvested 147 nJ energy (corresponding to the voltage of 17.2 V) from the impact of a 3 mm diameter rain drop at 4.5 ms^{-1}.

Beside the above-mentioned studies on the original structures for PEH from impacts, interesting trials to harvest keystroke energy with commercial impact-based piezoelectric igniters were proposed by Paradiso and Feldmeier (2001) and Tan et al. (2006), respectively. They built the circuits and demonstrated that the harvested energy from one strike is enough

to power an encoder and RF transmitter to transmit a 12 bit digital word information.

There are mainly two challenges for the design and analysis of impact-based PEH device. First, the theoretical base of the impact-based device is weak, compared to the harmonic excited devices. Analyses were mostly based on single degree-of-freedom (SDOF) approximation and equivalent circuit simulation, which is difficult to provide ideas for efficiency optimization. Second, the action time of each impact is very short; therefore, it is difficult to convert much energy into electrical form within this short interval. Adding a temporary mechanical storage to fast capture the energy and then slowly release and convert them into electrical form might provide improvement; yet, no such design yet exist.

Harmonic excited devices

Harmonic excited PEH devices were studied in a majority of literatures on PEH. The modeling techniques under harmonic vibration are more mature than those under impact excitations. However, the application of harmonic excited devices is confined by their resonant frequencies and corresponding bandwidths. The major design consideration under harmonic excitation is to design a mechanical structure, whose bandwidth covers the specific excitation frequency in a given application. Some mechanical methods were proposed for structural tuning that makes the resonant frequency adjustable. For example, Leland and Wright (2006); Hu et al. (2007) adjusted the resonant frequencies of a simply supported piezoelectric bimorph vibration energy scavenger by adding different compressive axial preloads to the bimorph. Challa et al. (2008) changed the stiffness of a piezoelectric cantilever by adding magnetic springs to the cantilever end so as to tune their parameters. Peters et al. (2009) proposed a closed-loop wide-range tunable mechanical resonator.

Human excited devices

Human-based excitations represent the excitations, which are characterized as *large amplitude* and *low frequency* (Beeby et al., 2006). Some of the human motions are similar to soft impacts, e.g., keystroke and heel strike; while some are closer to harmonic vibration, e.g., limb swing while walking. Since it is difficult to fabricate a light and small mechanical

structure whose resonant frequency matches the low frequency human motions, different human motions were usually transformed into impacts for exciting the piezoelectric generators.

The most well-known investigation was the piezoelectric-powered RFID shoes developed by MIT's Media Laboratory (Kymissis et al., 1998; Shenck and Paradiso, 2001). Two piezoelectric elements, one PZT dimorph and one PVDF stave, were embedded in the an insole to harvest heel strikes energy. 8.4 mW and 1.3 mW power were harvested at 0.9 Hz walking paces for the PZT dimorph and PVDF stave, respectively. However, no analysis was provided for the mechanical part, since their focus was on the design of the conditioning circuit that powers an RFID transmitter. Yoon et al. (2005) also adopted initially curved piezoceramic unimorphs to harvest heel strike energy. They studied the performances of pre-curved unimorphs at different sizes. They proposed a model to theoretically estimate the generated charge, but discrepancy was observed between experimental and predicted results. Besides the pre-curve structure, Howells (2009) proposed a compact design for heel strike power generation. The generated power is up to 90 mW.

The heel strike was the most investigated motion for human-based PEH, due to its large force feature. Some mechanisms were also utilized to harvest energy from other motions, e.g., the above-mentioned harvesting from keystroke using piezoelectric igniter (Paradiso and Feldmeier, 2001; Tan et al., 2006) and harvesting from limb motion by transforming the swing motion into impacts (Renaud et al., 2009).

Starner (1996) analyzed the potential power that can be harvested along with different human motions in detail. Since energy is the product of force and displacement, the challenge of energy harvesting from human motion using piezoelectric materials lies in that the displacement of a piezoelectric structure is usually constrained. On the other hand, the electromagnetic devices do not have this constraint. This is the advantage of utilizing electromagnetic generators to harvest energy from human motions (Kuo, 2005; Rome et al., 2005; Donelan et al., 2008).

Towards broadband / random excited devices

For harmonic excitation, the resonant frequency of a PEH device can be adjusted to match the excitation requirement by tuning some of its parameters; yet, for broadband excitation, the vibration response is still constrained by the device's bandwidth. To enhance the harvesting capability under broader frequency range, broadband solutions were investigated. The most direct way is to build multiple cantilever harvesters, which cover all the interesting frequencies (Xue et al., 2008; Yang and Yang, 2009). Some special configurations were also investigated to enable a broadband response, e.g., the L-shaped beam-mass structure (Erturk, Renno and Inman, 2009). Besides, the harvesting bandwidth might be broaden by involving some nonlinear mechanisms. Recently, a nonlinear piezo-magneto-elastic configuration attracted much attention (Erturk, Hoffmann and Inman, 2009; Ferrari et al., 2009; Lin and Alphenaar, 2009; Stanton et al., 2009, 2010; Lin et al., 2010). Similar configuration was also investigated in electromagnetic energy harvesting (Barton et al., 2010). The method was derived from the principle of magnetic levitation (Mann and Sims, 2009). The structure was composed of a piezoelectric cantilever and a pair of longitudinal repulsive permanent magnets – one attached at the end of the cantilever, and the other attached on a fixed frame. The nonlinear repulsive magnetic force changes the stable condition of the cantilever and makes it bistable. When a harmonic excitation is applied, this configuration induces large amplitude but chaotic responses under very wide frequency range. The results were encouraging, but since the vibration model is complicated, most studies were based on experimental results. In addition, Zhu et al. (2010) detailed different existing strategies for increasing the operating frequency range of vibration.

The electrical part also has an effect on the resonant frequency and bandwidth of a PEH device. Some discussions on harvesting under broadband random excitations were proposed from the circuit and control points of view (Lefeuvre et al., 2007; Halvorsen, 2008; Adhikari et al., 2009; Scruggs, 2009, 2010). But compared to the mechanical part, the influence of the electrical part is small, because the coupling coefficient is usually low. Therefore, the mechanical design is crucial towards broadening the bandwidth of PEH devices.

Mechanical transformations

Mechanical transformers are known from actuator developments, e.g., lever arms, bending structures, moonie, and cymbal structures (Rodig et al., 2010; Priya and Inman, 2009). In PEH devices, mechanical transformers were adopted to transfer the source energy into strain energy input to the piezoelectric element; at the same time, adapt the input mechanical impedance of the device to match the output impedance of vibration source, so as to ensure that maximum power is delivered to the piezoelectric element. The impedance matching in mechanical domain ensures that the power transferred from source to the piezoelectric element is maximized. Stephen (2006*b*) discussed the general maximum power transfer theorem within electromechanical systems. Nevertheless, few literatures presented the mechanical design whose mechanical impedance matches that of the vibration source. Kim et al. (2007) designed a cymbal piezoelectric transducer, which was optimized and fabricated to match the mechanical impedance of vibration source. Yet, no detailed design procedure was mentioned.

Mechanical part modeling

To analyze the vibration behavior, harvesting power, and conversion efficiency of PEH devices, different modeling techniques were adopted. But different from the models of pure mechanical or electrical systems, the model of PEH device should comprehensively describe the dynamics in the coupled mechanical and electrical domains. Given the parameter distributed nature in mechanical structures and nonlinear nature in real harvesting interface circuits, both of which encumber the model integration, simplification on either mechanical or electrical models are usually taken towards a unified model on both parts in these electromechanical systems.

The most used modeling techniques for the mechanical part are listed below:

a) Experimental method (no model), e.g., Shenck and Paradiso (2001)

b) Neglecting the mechanical dynamics (constant displacement), e.g., Ottman et al. (2002)

c) Lumped models

- SDOF [2] approximation
  - Second order ODE [3], e.g., Shu and Lien (2006*a*)
  - Single RLC [4] equivalent circuit, e.g., Richards et al. (2004)
- MDOF [5] approximation
  - Multiple RLC equivalent circuit, e.g., Elvin and Elvin (2009*b*)

d) Distributed parameter models

- Analytical solution of PDE [6], e.g., Erturk and Inman (2008*b*)
- FEM [7] simulation, e.g., Zhu et al. (2009)

The modeling techniques for the electrical part as well as the coordination between the mechanical and electrical models in existing literatures are discussed in sub-section 1.3.2.

1.3.2 Electrical part emphases

According to Figure 1.1, the electrical part of the PEH device includes the electrical characteristics of the piezoelectric transducer, the interface circuit, the energy storage, and the DC load. Some literatures, e.g., Guyomar et al. (2005), called the input characteristic of the interface circuit as AC load. In this sense, the AC load represents all the characteristics of interface circuit, energy storage, and DC load. The electrical part of the device functions to:

a) elaborately extract energy that outputs from the piezoelectric transducer;
b) transform the AC energy into DC, so as to power the DC load.

Some mechanical part emphasized literatures took a resistor as the AC load to represent the entire shunt circuit, so as to estimate the harvesting power. From the research point of

[2] SDOF is the acronym of single degree-of-freedom.
[3] ODE stands for ordinary differential equation.
[4] RLC stands for resistor, inductor, and capacitor.
[5] MDOF stands for multiple degree-of-freedom.
[6] PDE stands for partial differential equation.
[7] FEM stands for finite element method.

view, it is understandable, in particular when the mechanical model is complicated. However, from practical point of view, Mitcheson et al. (2008) pointed out that a pure resistive AC load is not useful and a typical load will be a diode rectifier and smoothing capacitor. Moreover, this oversimplification might lead to some neglects on the details in PEH.

Interface circuits

The interface circuit directly handles the energy extraction from the transducer, therefore it plays an important role in harvesting power or efficiency optimization. On the other hand, the energy output from the transducer is not fixed, but changes with the dynamics of both the mechanical and electrical parts; therefore, the interaction between these two parts is crucial. Studying the interface circuits may provide more in-depth understanding to this electromechanical interaction.

In the early studies, the conventional half-wave (Elvin et al., 2001) and full-wave (Umeda et al., 1997) rectifiers were adopted to extract energy from vibrating piezoelectric structures. The half-wave rectification was simply implemented with one diode. But since it only makes use of half of the vibration cycle, the harvesting efficiency is lower than the full-wave rectification. The full-wave bridge rectifier, as shown in Figure 1.2, is regarded as the standard energy harvesting (SEH) interface. It is *passive* and easy-to-use, therefore, is widely used to implement PEH devices until now. For SEH, Umeda et al. (1997) pointed out that the harvesting performance largely depends on the rectified voltage. Ottman et al. (2002, 2003) derived the relation between the harvesting power and the rectified voltage, and further implemented a DC-DC stage for adapting the rectified voltage towards maximum harvesting power. Later, by comparing to Ottman et al. (2002, 2003)'s results, Guan and Liao (2007) indicated that, the one-stage scheme, i.e., only bridge rectifier, can achieve higher efficiency than the two-stage scheme.

Based on the capacitive nature of piezoelectric transducers, a category of *semi-passive interface circuits* were proposed to further improve the harvesting capability (Guyomar et al., 2005). The most studied semi-passive interfaces include: parallel synchronized switching harvesting on inductor (P-SSHI), series synchronized switching harvesting on

inductor (S-SSHI), and synchronous charge extraction (SCE). These interface circuits were built by adding a switch path to the SEH interface in different places, so as to synchronously switch the load condition of the transducer. Implementing the synchronized switching action results in the increase of input energy in every vibration cycle. Two valuable comparisons on the conventional SEH and the above-mentioned three semi-passive interfaces were provided by Lefeuvre, Badel, Richard, Petit and Guyomar (2006) and Qiu et al. (2009). It was shown both theoretically and experimentally that the semi-passive techniques can increase the harvesting power by several hundred percents, compared to the passive SEH.

The implementation of the synchronized switching actions is another issue for the semi-passive interfaces. The switching actions take places to quickly invert the voltage across the piezoelectric element whenever the vibration displacement is at its maxima and minima. In most of the studies, a displacement sensor and a computer-based controller were utilized for synchronization and generation of switching commands (Lefeuvre, Badel, Richard, Petit and Guyomar, 2006; Makihara et al., 2006; Neubauer et al., 2010). Lallart and Guyomar (2008) and Qiu et al. (2009) introduced a self-powered SSHI. Liang and Liao (2009*a*) improved the topology as well as the analysis to the self-powered circuit. Ramadass and Chandrakasan (2010) proposed a CMOS based integrated self-powered SSHI circuit [8].

Most of the analyses on SSHI were based on the assumption that the periodic excitation (force) and the speed of mass are in phase, i.e., the electromechanical system is under resonance. It also implies that the mechanical dynamics in fact was neglected in these analyses. Shu et al. (2007) pointed out this and provided an improved analysis to the SSHI interface circuit. The mechanical dynamics in SSHI treatment can also be included with the impedance based analysis (Liang and Liao, 2010*a*). Besides, there are several literatures considered other issues in SSHI. For example, the influence of the damping ratio of the electrical branch, the frequency ratio between the excitation and the switching electrical resonance branch, and the voltage gaps across the rectifier diodes (Neubauer et al., 2010); the way to further increase the extracted power by enhancing the voltage inversion (Lal-

[8] Ramadass and Chandrakasan (2010) called the SSHI interface as bias-flip rectifier in their paper.

lart, Garbuio, Richard and Guyomar, 2010); and the influence of the dielectric loss of the piezoelectric element (Liang and Liao, 2009*b*).

Besides the passive and semi-passive interface circuits, Liu, Tian, Wang, Lin, Zhang and Hofmann (2009) introduced the *active interface circuit*. The circuit is modified from the SEH interface by replacing the passive bright rectifier into active MOSFET H-bridge, which is usually used in motor driver. Liu, Vasic, Costa, Wu and Lee (2009) reached a similar point, but they called their method as velocity-controlled PEH. These ideas were generated for the purpose of achieving rectangular shape ideal electrical work cycle (Liu, Vasic, Costa, Wu and Lee, 2009). Earlier than those, Liu et al. (2007) provided a similar analysis, except that a direct actuator driver instead of an H-bridge driver was used in their proposed setup. In these so called active PEH interfaces, energy is not only extracted from, but also actively input into, the mechanical part. Liu et al. (2007) and Liu, Vasic, Costa, Wu and Lee (2009) provided no analysis on this energy relation. Liu, Tian, Wang, Lin, Zhang and Hofmann (2009) gave analytical equations and also experimental results; however, their agreement was no shown. The improvement of this active interface on harvesting power, compared to other interfaces, was not mentioned either.

All the above-mentioned analyses on interface circuits were based on the condition that the normalized rectified voltage (rectified voltage over open circuit voltage) is constant. This condition is satisfied when both the vibration amplitude as well as the rectified voltage are unchanged. If this condition is not satisfied, the circuit behaviors differ from cycle to cycle. Wickenheiser et al. (2010) and Wu et al. (2009) investigated the transient behaviors of the SEH and SCE interface circuits. Lallart, Inman and Guyomar (2010) considered those of SEH and SSHI interfaces under constant force excitation. Badel et al. (2005) studied the behavior of SSHI after a pulsed force is applied. These investigations are valuable towards better understanding on transient behaviors of the harvesting interface circuits.

Energy storage

In PEH systems, the generated power is usually too low to instantly power the end devices, even with the elaborately designed interface circuits. It is necessary to use energy

storage devices to save the harvested energy for the later releasing in the so called "burst mode" (Ng and Liao, 2005).

Sodano et al. (2005*a*) studied the performances of three piezoelectric devices, i.e., monolithic PZT, bimorph Quick Pack (QP) actuator, and macro-fiber composite (MFC), for recharging nickel metal hydride (NiMH) batteries in different capacities. Based on their experimental results, they concluded that both the monolithic PZT and QP were capable of recharging the batteries; but the PZT outperformed the QP in random vibration environment. On the other hand, the MFC was not well suited for power harvesting.

Guan and Liao (2008) investigated the recharging issue in different aspects. They considered the performance of a PEH devices in recharging three different storage devices, i.e., supercapacitor, NiMH battery, and lithium rechargeable battery. They concluded that supercapacitors are more desirable than rechargeable batteries as energy storage devices in PEH systems.

Both Sodano et al. (2005*a*) and Guan and Liao (2007) used single stage SEH interface for batteries recharging. Guan and Liao (2007) stated that the two-stage SEH charging scheme is not a suitable choice, because the power consumption of the second DC-DC stage is high. Hu et al. (2008) proposed a theoretical analysis on the recharging performance of a double stage SSHI device; yet, the power consumption of the conditioning circuit was not taken into consideration in their analysis.

Thin-film battery is also a candidate storage device in PEH systems (Priya and Inman, 2009). It is compact and easy to be integrated into printed circuit boards (PCBs) and integrated circuit (IC) packaging. Recently, Anton et al. (2009) investigated the self-charging structures, which integrate both the piezoelectric materials and thin-film batteries.

In all these energy storage related literatures, the chemical batteries were directly charged with the output from the harvesting interfaces. Nevertheless, it is known that the voltage and current requirements for recharging chemical cells are usually stringent. Failure to comply with these requirements might greatly influence batteries' capacity and rechargeable cycles. Therefore, when using chemical batteries as the energy storage device in PEH, perhaps the biggest challenge is the design of low power consumption electronics, which, on one hand,

maintain the optimum harvesting conditions; on the other hand, efficiently match the output of the harvesting device with the specific voltage requirements (Priya and Inman, 2009).

Electrical part modeling

Different models or equivalences were adopted to describe the dynamics of the electrical part in the PEH devices. Some commonly used modeling techniques for the electrical part are listed below:

a) Linear resistive equivalence, e.g., Erturk and Inman (2008*b*)
b) Piecewise equations & waveforms, e.g., Ottman et al. (2002)
c) Circuit simulation, e.g., Shu et al. (2007)
d) Equivalent impedance network, e.g., Liang and Liao (2010*b*)

General speaking, the modeling approaches for both mechanical and electrical parts are correlated. By summarizing different combinations of mechanical and electrical models in most of the previous studies, it is found that

- in *structural dynamics emphasized studies*, advanced mechanical models, e.g., distributed parameter models, were usually adopted, but, the electrical part was usually simplified, e.g., taking resistive equivalence;
- in *electrical treatments emphasized studies*, advanced electrical analyses, e.g., piecewise equations, were usually adopted but, the mechanical part was usually simplified, e.g., neglecting the mechanical dynamics.

For instance, Erturk and Inman (2008*a*,*b*,*c*) provided useful insight to analytically model the PEH cantilevers as distributed parameter systems. Their mechanical model was able to better represent the mechanical dynamics; whereas, the electrical part is simplified as a linear resistive load. Ottman et al. (2002) analyzed the performance of the nonlinear SEH interface circuit with piecewise equations and waveforms. In their studies, the mechanical part was modeled as an equivalent current source, which implies that the vibration amplitude

was assumed to be unchanged with the harvesting treatment. In another word, the dynamics of the mechanical part was neglected.

Recently, Elvin and Elvin (2009*a*) made effort to integrate two advanced modeling techniques, i.e., FEM and circuit simulators, for the simulation of PEH systems. This combination avoided the oversimplification in either domain, therefore, it is applicable to accurately represent the overall dynamics of a PEH system with complicated structure and nonlinear treatment. However, the computational cost of this explicit coupled FEM-SPICE model is high. Referring to this drawback of the FEM-SPICE simulation, Yang and Tang (2009) modeled the mechanical part as multiple RLC equivalent circuit, so that the whole system can be efficiently analyzed with only circuit simulator. The parameters in the equivalent circuit were identified by FEM; therefore, as they claimed, this approach can also be used to simulate PEH system with complicated structure and nonlinear treatment.

1.3.3 Transducer emphases

The characteristics of a piezoelectric transducer are divided into three aspects: mechanical, electrical, and electromechanical coupling. The *IEEE Standard on Piezoelectricity* (1988) provided the principle on linear piezoelectricity in detail. The constitutive equations described the piezoelectric coupling effect at material level; on the other hand, at element level, both the geometric configuration of the element and electrical connection of electrodes influence the coupling. Therefore, materials, geometric configuration, and electrical connection are three major considerations in the design or selection of piezoelectric transducers.

Materials

The most commonly used piezoelectric materials are classified into three categories: single crystal, ceramic based, and polymer based (Rodig et al., 2010).

The single crystal materials, e.g., lead magnesium niobate-lead titanate (PMN-PT), are characterized as high conversion efficiency but high cost, compared to the widely used ceramic based materials. Several PEH devices utilizing PMN-PT materials were investigated

(Ren et al., 2006; Sun et al., 2009; Song et al., 2009). Badel et al. (2006) and Mo et al. (2010) compared the the performances of PMN-PT and ceramic PZT harvesters in similar configurations. They both found that the harvesting power of PMN-PT harvesters is at least one order more than that of PZT harvesters. Besides, some other single crystal materials in nano-scale, e.g., zinc oxide (ZnO) and barium titanate ($BaTiO_3$) nanowires, attracted much attentions recently (Wang and Song, 2006; Wang et al., 2007). But there is still a long way to go before implementing these nano-scale transducers in practical PEH devices.

The single crystal materials do have higher coupling coefficient; but their performance-cost-ratios are low. Ceramic based piezoelectric materials are widely used for many years for sensors, actuators, and even generators (piezoelectric igniters). Many ceramic based transducers with different configurations and packagings are commercially available. Within these materials, the lead-zirconate-titanate (PZT) is the most used material for energy harvesting (Ottman et al., 2002; Sodano et al., 2005*a*; Guan and Liao, 2008). In terms of the coupling direction, the ceramic based transducers are usually selectly operated under two modes, i.e., 3-3 mode, and 3-1 mode. For the purpose of increasing the energy conversion, transducers utilizing the 3-3 mode are usually made into stack configuration; while those utilizing 3-1 mode are usually made into cantilever configuration. Generally, it was concluded that in small force, low vibration level environment, the 3-1 mode configuration cantilever proved to be more efficient; but in high force environment, the 3-3 mode stack configuration would be more durable to generate useful energy (Anton and Sodano, 2007). Monolithic ceramics have a significant disadvantage on its brittle nature, which limits their maximum strain level. But with some techniques, the ceramic based materials can be mixed into composites, so as to make more flexible transducers, e.g., micro-fiber composites (MFCs) (Sodano, Park and Inman, 2004).

Polymer based piezoelectric materials provide another option for PEH. It is soft and therefore more flexible than the other categories of materials. One main problem is that the polymer's coupling coefficient is relatively low. Polyvinylidene fluoride (PVDF) is the most investigated piezoelectric polymer. It was more suitable to be implemented in large deformation and high flexibility applications. For example, harvesters imbedded in the shoe

sole (Shenck and Paradiso, 2001); harvesting eel (Taylor et al., 2001); harvesting backpack straps (Granstrom et al., 2007); harvesting from flow induced vibrations (Wang and Ko, 2010).

Mechanical configurations

Piezoelectric materials can be made into transducers in different shapes and sometimes with multiple layers. For PZT transducers, plate and stack configurations were mostly used for 3-1 and 3-3 coupling modes. As ceramics are usually stiff, excitations are seldom directly applied on single ceramic based transducers, but through the mechanical transformers (usually force amplifiers). The plate transducers were mostly integrated with cantilevered structures for transforming the transverse deflection into longitudinal deformation (Ajitsaria et al., 2007). In some applications, two plate layers were integrated to form a bimorph cantilever (Ng and Liao, 2005). Besides, the plate transducers can also be integrated with moonie or cymbal structures as the mechanical transformer (Kim et al., 2007). The stack transducers were integrated with mechanical force amplifiers (Jeong et al., 2008; Feenstra et al., 2008). In addition, in some designs, the transducers were configured to serve as the mechanical transformer at the same time, e.g., the initially curved piezoceramic unimorphs introduced by Yoon et al. (2005).

To improved the flexibility of ceramic based transducers, some piezoelectric composites were introduced. MFC is one of the successful products. In MFC, the PZT was made into fibers and imbedded in Kapton film. These configuration greatly increase the overall strength of the material (Sodano, Park and Inman, 2004). MFC can be utilized to implement PEH devices (Yang et al., 2009; Song et al., 2010); yet, as shown by Sodano et al. (2005*a*), the MFC is not as efficient as the QuickPack actuator and the monolithic PZT in energy harvesting. Besides MFC, recently, Qi et al. (2010) introduced the methodology to print PZT ribbons onto stretchable, bio-compatible rubbers. This technique enables more flexible piezoelectric transducers; therefore, might yield breakthroughs in implantable or wearable energy harvesting systems, as the inventors claimed.

Electrical connections

When the piezoelectric transducers are configured with multiple layers, different connections of electrodes also have an effect on PEH system. Ng and Liao (2005) compared the performances of three cantilevers, i.e., unimorph, series connected triple-layer bimorph, and parallel connected triple-layer bimorph. They concluded that, generally, the unimorph sensor can generate the highest power for low load resistances and frequencies; the parallel triple-layer bimorph generates the highest power for medium load resistances and frequencies; and the series triple-layer bimorph generates the highest power for even higher load resistances and frequencies. Similar conclusions were obtained by Song et al. (2010) in their studies with an MFC bimorph cantilever.

Transducer modeling

Most of the literatures regarded the piezoelectric transducer as ideal transducer, i.e., lossless and linear coupling. In practice, the internal loss and nonlinear coupling might influence the energy harvesting. Liang and Liao (2009*b*) included the transducer loss in the analysis of SSHI, based on which they provided an explanation on the voltage reversion phenomenon in SSHI. Hu et al. (2006) and Triplett and Quinn (2009) analyzed the effect of nonlinear coupling on the performance of PEH. Triplett and Quinn (2009) concluded that when the nonlinear effect is small, the harvesting power slightly increases, compared to the linear model; whereas, as the nonlinearity increases, the harvesting power become much smaller than the linear estimation.

1.3.4 System emphases

As mentioned, the performance of a PEH device depends on its mechanical part, electrical part, and also the electromechanical coupling. Besides the overall dynamics, which was emphasized in many literatures, several systematic issues were also addressed. These issues are crucial towards better understanding and optimization of an overall PEH system.

Electromechanical interaction

The electromechanical interaction in a PEH system is embodied by the structural effect, which is induced by energy harvesting.

Lesieutre et al. (2004) stated that removal of energy from a vibrating system necessarily results in structural damping. They studied the damping effect associated with a SEH system, and found that the additional damping introduced by the harvesting treatment agreed with their theoretical estimation. Later, Liang and Liao (2009*c*) provided a comparative study on the functions of piezoelectric energy harvesting, dissipation, and their joint effect on the structural damping of vibrating structures. It was clarified that the energy harvesting and dissipation functions usually coexist in a PEH treatment, e.g., SSHI. Both of them bring out structural damping. Similar concept was also mentioned by Liao and Sodano (2009). Without the investigation on the energy flow within harvesting circuits, the relations among energy harvesting, energy dissipation, and their effect on structural damping are unable to be quantitatively explained.

Besides structural damping, the harvesting circuit might also influence the effective stiffness of the structure. Liang and Liao (2010*b*) introduced the impedance based analysis for the whole PEH system. They decomposed the electrical part into three components. Two of them, representing the harvesting and dissipation functions, are resistive; while the other is capacitive. The capacitive component in the electrical part functions as additional stiffness to the structure. Owning to this increase on effective stiffness, the resonance frequency might shift. This resonance shift phenomenon was observed by Lesieutre et al. (2004), but has not been explained in detail.

Harvesting power

The harvesting power and efficiency are two major indices, which were usually taken as the optimization objectives for PEH devices.

One widely referred model for vibration energy harvesting and expression on harvesting power were proposed by Williams and Yates (1996). In their model, the vibration power

generators were taken as base excited SDOF mass-spring-damper systems. The damping effect was attributed to two portions, the mechanical damping and the electrical damping (results from energy harvesting). Even since then, many literatures, including a majority of review articles (Beeby et al., 2006; Cook-Chennault et al., 2008; Gilbert and Balouchi, 2008; Hudak and Amatucci, 2008; Mateu and Moll, 2005; Mitcheson et al., 2004, 2007; Priya, 2007; Zhu et al., 2010; Roundy et al., 2004), regarded this as the general model for vibration energy harvesting devices, including piezoelectric, electromagnetic, and electrostatic. Yet, Erturk and Inman (2008*c*) pointed out that the backward coupling effect from electrical to mechanical domain cannot be simply represented by only electrically induced damping; therefore, the expression on harvesting power given by Williams and Yates (1996) needed to be improved for PEH. As mentioned by Erturk and Inman (2008*c*), one of the improved analyses was proposed by Dutoit et al. (2005). Recently, Renno et al. (2009) proposed another power analysis as well as optimization, based on the Karush-Kuhn-Tucker (KKT) method. But these improvements were not complete in fact. The electrical circuit was represented by a linear resistor, which oversimplified the behavior of real harvesting circuits.

As mentioned in sub-section 1.3.2, literatures emphasizing the mechanical part oversimplified the electrical part, and vice versa. In electrical part emphasized literatures, the provided expressions on harvesting power were frequently separated from mechanical dynamics. Uncoupled [9] (Ottman et al., 2002; Wu et al., 2009; Liu, Tian, Wang, Lin, Zhang and Hofmann, 2009) or in-phase (Guyomar et al., 2005) assumptions were made in most of these electrical part emphasized analyses.

Only when the dynamics of both parts are better represented, rather than oversimplified, the harvesting power expression can be obtained more accurately. For example, Shu and Lien (2006*a*) proposed a coupled analysis by taking the the SDOF representation for the mechanical part and the piecewise description for the SEH circuit. The power optimization formula was also provided.

On the other hand, the *maximum power transfer theorem* is well-known for power opti-

[9] Some literatures referred the uncouple assumption as the same as applying constant displacement excitation.

mization, in particular, in electrical engineering. Maximum power is transferred when the load impedance matches the source impedance, i.e., being complex conjugate to the source impedance. Several literatures investigated the power optimization formula based on this theorem. Some literatures investigated impedance matching problem by taking the shunt circuit as a linear resistor (Kim et al., 2007; Op het Veld et al., 2009; Kong et al., 2010); while some considered the matching problem by taking it as general complex impedance, whose values are able to be arbitrarily chosen (Brufau-Penella and Puig-Vidal, 2009; Nakano et al., 2007). Similar analyses were also found for power optimization in electromagnetic energy harvesting (Stephen, 2006*b*; Nakano et al., 2007; Cammarano et al., 2010). One common problem of these literatures on impedance matching for PEH devices was that the equivalent impedances of real harvesting circuits were not reasonably considered. Concerning this issue, Liang and Liao (2010*b*) discussed the impedance matching problem based on the equivalent impedances of real harvesting circuits. They concluded that the equivalent impedance of the electrical part is constrained, rather than able to be arbitrarily set. Besides, considering the energy flow within a PEH system, they also clarified the objective of impedance matching, which would be confused in previous literatures.

Harvesting efficiency

Efficiency is another concern for harvesting optimization. Roundy (2005) investigated the efficiency problem by analyzing the relation between the input and output power of linear transducers. However, the effects of other mechanical and electrical components in PEH systems on the harvesting efficiency were unable to be included in his model. One widely referred (Beeby et al., 2006; Cook-Chennault et al., 2008; Gilbert and Balouchi, 2008; Priya, 2007) explicit expression on optimum conversion efficiency was proposed by Richards et al. (2004), and was derived based on the equivalent circuit analysis. Yet, several insufficiencies were still found with Richards et al. (2004)'s analysis: 1) the electrical circuit was oversimplified as a resistor; 2) maximum efficiency was assumed to occur when the AC load matches the impedance of the piezoelectric capacitance, which would be misleading. Because impedance matching implies maximum transfer power, rather than maximum effi-

ciency. By analyzing the energy conversion efficiency in SEH device, Shu and Lien (2006*b*) made a complement to Richards et al. (2004)'s analysis: the maximum conversion efficiency corresponds to the maximum electrical induced damping as well as the optimal power transfer in the case of *weak electromechanical coupling*; on the contrary, for *strongly coupled electromechanical systems*, the optimal electrical load maximizing the conversion efficiency and induced electric damping is very different from that maximizing the harvested power. Similar conclusions were also drawn by Liao and Sodano (2009). Therefore, even the resistive oversimplification is acceptable, Richards et al. (2004)'s expression on conversion efficiency is only valid under weakly coupled conditions.

1.4 Research Objective

As discussed in Section 1.3, a majority of literatures on PEH tended to either emphasized the mechanical part, but oversimplified the electrical part; or emphasized the electrical part, but oversimplified the mechanical part. The overall dynamics of the PEH devices are unable to be truly represented by these one-sided analyses. In addition, the oversimplification on either part might lead to the neglect of some detailed electromechanical interaction, as well as the inaccurate results on harvesting power and efficiency.

To overcome these insufficiencies in previous studies, two important issues should be investigated from the systematic point of view.

a) Understanding of the detailed electromechanical interaction, in terms of energy.
b) A suitable model which can properly include the dynamics of both the mechanical part and the electrical part with real harvesting circuits.

The investigation on these two issues are highlighted in this thesis. The first issue is explained with the concept of *energy flow*, which gives the qualitative understanding on the behavior of the overall system. The second issue is solved with the *equivalent impedance modeling*, which helps for the quantitative studies on each branch of the energy flow. With these improved analyses, the harvesting power optimization can be carried out. The analyses

on different interface circuits as well as some practical issues on their implementations are also discussed.

1.5 Thesis Outline

This thesis is organized as follows:

Chapter 1 introduces the background of piezoelectric energy harvesting (PEH). An overview to the PEH system is provided. The state of the art in the research of PEH is classified into four aspects, i.e., the mechanical part, the electrical part, the transducer, and the overall system.

Chapter 2 develops an equivalent circuit based piezoelectric device model, which can include the dynamics of both the mechanical and electrical parts. The model can serve as a common base for energy harvesting and dissipation analyses.

Chapter 3 discusses the electromechanical interaction within a PEH device by introducing the concept of energy flow. Terms are specified to clarify some commonly observed confusions among the concepts of energy harvesting, energy dissipation, and structural damping. Based on the definition, two applications of standard energy harvesting (SEH) and resistive shunt damping (RSD) are investigated and compared. Furthermore, in the application of synchronized switch harvesting on inductor (SSHI), it is shown that the two functions of energy harvesting and dissipation are coexistent. Both of them bring out structural damping. Further analyses and optimization for the SSHI technique are performed.

Chapter 4 further models the equivalent circuit into equivalent impedance network, in which both the mechanical and electrical parts of a PEH device are uniformly included. The equivalent impedance model allows the analysis on the dynamics of the overall system with real harvesting circuit. Moreover, some new findings are obtained and discussed towards the power optimization.

Chapter 5 discusses the commonly used installations for energy harvesting under displacement excitation and base excitation. Based on the equivalent impedance model, the dynamics on power harvesting under these two excitations are investigated and compared.

In the experiment of SSHI, it was observed that the voltage across the piezoelectric element has a reversion every time after its inversion, which results in the degradation of harvesting power. Chapter 6 investigates the influence of this phenomenon in PEH with SSHI interface and discusses the possible origin of this phenomenon.

Chapter 7 focuses on the practical implementation of the synchronized switching interface circuit in PEH. A modified self-powered SSHI interface circuit as well as an improved analysis to this circuit are proposed.

Chapter 8 concludes the thesis and provides an outlook to the future work.

□ End of chapter.

Chapter 2

Piezoelectric Device Modeling

As a category of versatile smart materials, piezoelectric materials can be utilized for different sensors and actuators, to suppress structural vibration, to harvest energy from ambient vibration, etc. All these devices can be called piezoelectric devices. To analyze the overall dynamics of piezoelectric devices, we should firstly have a common description on the piezoelectric effect. As given in the *IEEE Standard on Piezoelectricity* (1988), the linear piezoelectricity can be represented by four sets of constitutive equations as follows

$$\begin{bmatrix} T_p \\ D_i \end{bmatrix} = \begin{bmatrix} c_{pq}^E & -e_{kp} \\ e_{iq} & \varepsilon_{ik}^S \end{bmatrix} \begin{bmatrix} S_q \\ E_k \end{bmatrix} \tag{2.1}$$

$$\begin{bmatrix} S_p \\ D_i \end{bmatrix} = \begin{bmatrix} s_{pq}^E & d_{kp} \\ d_{iq} & \varepsilon_{ik}^T \end{bmatrix} \begin{bmatrix} T_q \\ E_k \end{bmatrix} \tag{2.2}$$

$$\begin{bmatrix} S_p \\ E_i \end{bmatrix} = \begin{bmatrix} s_{pq}^D & g_{kp} \\ -g_{iq} & \beta_{ik}^T \end{bmatrix} \begin{bmatrix} T_q \\ D_k \end{bmatrix} \tag{2.3}$$

$$\begin{bmatrix} T_p \\ E_i \end{bmatrix} = \begin{bmatrix} c_{pq}^D & -h_{kp} \\ -h_{iq} & \beta_{ik}^S \end{bmatrix} \begin{bmatrix} S_q \\ D_k \end{bmatrix} \tag{2.4}$$

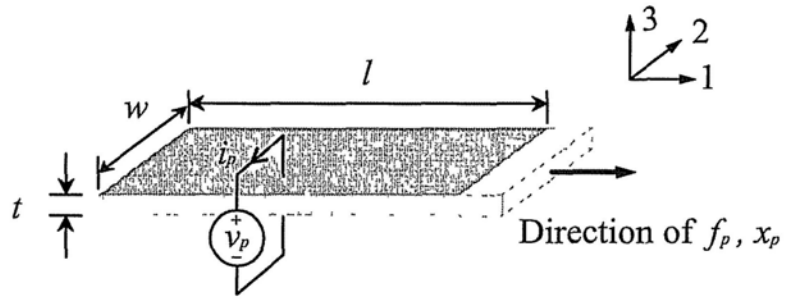

Figure 2.1: Schematic diagram of piezoelectric patch.

where T, S, D and E denote the stress, strain, electric displacement and electric field, respectively; d, e, g and h are piezoelectric constants; c is elastic stiffness constant; s is elastic compliance constant; ε is permittivity constant; β is impermittivity constant; the subscripts are tensor notations; the superscripts T, S, D and E denote the corresponding parameters at constant stress, strain, electric displacement and electric field, respectively. Either one of these fours can be used to describe the same coupling characteristics of piezoelectric materials. In the studies of traditional damping, (2.2) was usually used (Hagood and von Flotow, 1991; Clark, 2000; Moheimani, 2003); while in the studies of energy harvesting, (2.1) was more popular (Badel et al., 2005; Shu et al., 2007); but still, there were exceptions (Lesieutre and Christopher L. Davis, 1997; Ng and Liao, 2005; Roundy, 2005).

This chapter begins with the dynamic representations with these four sets of constitutive equations, in terms of impedance. Based on these, we select one as the common base of our analysis and then obtain the device model and equivalent circuit.

2.1 Dynamic Representations

Suppose a piezoelectric element, whose dimensions are shown in Figure 2.1, is bonded on a vibrating beam, and is working under 3-1 mode. Assuming the motion wavelength is much larger than l; and l, w are much larger than the thickness t, the strain, stress, electrical field and electrical displacement can be regarded to be homogeneously distributed within

the element. Four dimensional relations can be obtained

$$f_p = twT_1\,, \qquad x_p = lS_1\,, \qquad v_p = -tE_3\,, \qquad q_p = wlD_3 \tag{2.5}$$

where f_p, x_p denote the force and displacement of the piezoelectric patch in the "1" direction; v_p, q_p denote the voltage across and charge stored in the "3" direction. Substituting (2.5) into (2.1) yields the macroscopic piezoelectric equations.

$$\begin{bmatrix} f_p \\ q_p \end{bmatrix} = \begin{bmatrix} \frac{tw}{l}c_{11}^E & we_{31} \\ we_{31} & -\frac{wl}{t}\varepsilon_{33}^S \end{bmatrix} \begin{bmatrix} x_p \\ v_p \end{bmatrix} \tag{2.6}$$

(2.6) does not explicitly show the dynamic behavior of the piezoelectric patch. To study the dynamic behavior, two derivative relations between electrical current and charge, mechanical velocity and displacement are needed, i.e.,

$$i_p = \frac{\mathrm{d}}{\mathrm{d}t}q_p\,, \qquad \dot{x}_p = \frac{\mathrm{d}}{\mathrm{d}t}x_p \tag{2.7}$$

where i_p denotes current, $\dot{x}_p$ denotes velocity. Substituting (2.7) into (2.6) and doing the Laplace transform yields

$$\begin{bmatrix} F_p \\ I_p \end{bmatrix} = \begin{bmatrix} K^E/s & \alpha_e \\ \alpha_e & -sC^S \end{bmatrix} \begin{bmatrix} \dot{X}_p \\ V_p \end{bmatrix} \tag{2.8}$$

where F_p, I_p, $\dot{X}_p$, and V_p are the Laplace transforms of f_p, i_p, $\dot{x}_p$, and v_p, respectively; s is the Laplace operator. In the matrix

$$K^E = \frac{tw}{l}c_{11}^E\,, \qquad C^S = \frac{wl}{t}\varepsilon_{33}^S\,, \qquad \alpha_e = we_{31} \tag{2.9}$$

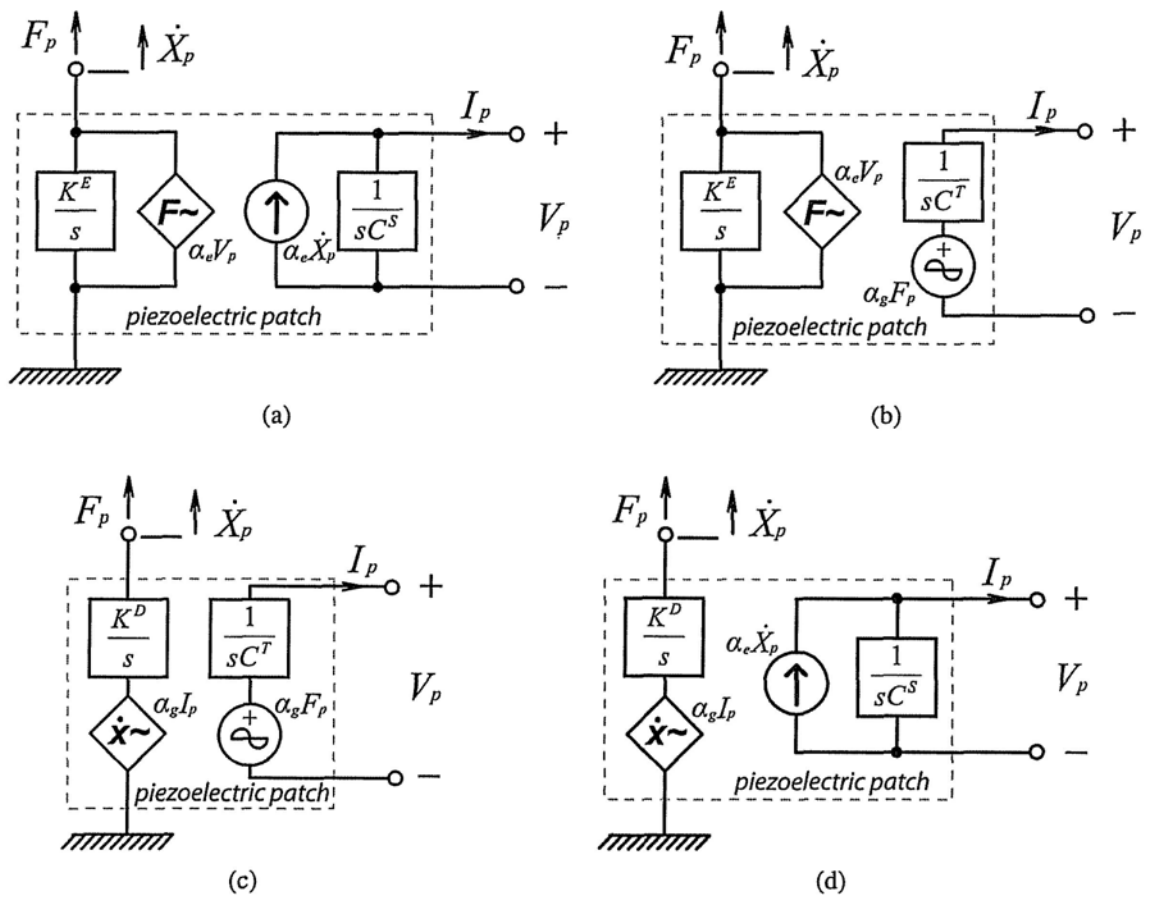

Figure 2.2: Schematic diagrams corresponding to four sets of constitutive equations. (a) P-P model. (b) P-S model. (c) S-S model. (d) S-P model.

are the short circuit stiffness, clamped capacitance, and force-voltage coupling factor of the piezoelectric patch, respectively.

For illustration, Figure 2.2(a) shows the schematic diagram corresponding to (2.8). Note that K^E/s represents the mechanical impedance of the short circuit stiffness in "1" direction, and $1/(sC^S)$ represents the electrical impedance of the clamped capacitance in "3" direction. This model regards the mechanical part as the patch's stiffness in parallel with a force source, and the electrical part as the capacitance in parallel with a current source. We call this P-P model in brief, where "P" stands for parallel relation. Similarly, for the other three constitutive equations, i.e. (2.2) $\sim$ (2.4), we can derive the P-S, S-S, S-P models corresponding to Figure 2.2(b) $\sim$ (d), where "S" stands for series relation. K^D, C^T, α_g

are the open circuit stiffness, free capacitance, and velocity-current coupling factor of the piezoelectric patch, respectively.

Since those four dynamic models illustrated in Figure 2.2 are compatible to the analyses of mechanical impedance networks and electrical ones, they can provide us with a guideline for selection of constitutive equations in the analyses of piezoelectric devices. For instance, from the electrical point of view, it will be more convenient to use P-P or S-P models to analyze devices whose shunt circuit network is built up by parallel connecting impedances; P-S or S-S models are preferred for shunt network built up in series.

2.2 Device Model

The device model differs from the element level one shown in Figure 2.2 in that it includes both the external mechanical and electrical components in the governing equation.

Based on (2.2), Hagood and von Flotow (1991) also drew a macroscopic representation for the electrical part of the piezoelectric materials, and included shunt impedance in the governing equations. This process altered the equations to "half device level", thus made it possible to consider the piezoelectric patch and its shunt circuit as a whole. Besides, consider the dynamic definition of device coupling coefficient given by

$$k_d^2 = \frac{\left(\omega^D\right)^2 - \left(\omega^E\right)^2}{\left(\omega^D\right)^2} = \frac{K^D - K^E}{K + K^D} \tag{2.10}$$

where ω^D is the open-circuit natural frequency, ω^E is the short-circuit natural frequency, and K is the stiffness of the substrate structure. This dynamic definition is again in "half device level", since the measurements of ω^D and ω^E regard the mechanical part of the device as a whole, but exclude the shunt circuit from the device.

From another point of view, given the relation between the open circuit and short circuit stiffness for the piezoelectric element

$$K^D = K^E + \frac{\alpha_e^2}{C^S} \tag{2.11}$$

the device coupling coefficient can also be expressed as

$$k_d^2 = \frac{\alpha_e^2}{(K+K^E)C^S + \alpha_e^2} \tag{2.12}$$

Compared to the electromechanical coupling coefficient at element level (Badel et al., 2005)

$$k_e^2 = \frac{\alpha_e^2}{K^E C^S + \alpha_e^2} \tag{2.13}$$

it is more obvious that only the substrate structural stiffness is included in the so called device coupling coefficient.

Referring to the these two analyses at either electrical or mechanical device level, and based on our representations for piezoelectric materials, we form an integrative device model by extending the P-P model of piezoelectric materials. The mounting piezoelectric patch on the beam structure can be modeled as mechanical impedances in parallel (Badel et al., 2005), i.e.,

$$F = F_p + Z_{mech\text{-}ex}\dot{X}_p \tag{2.14}$$

where $Z_{mech\text{-}ex}$ is the external mechanical impedance, F is the total force applied to the mechanical structure. The electrical shunt circuit appeared in parallel to the inherent piezoelectric capacitance (Hagood and von Flotow, 1991). Regarding the shunt circuit as the external electrical impedance $Z_{elec\text{-}ex}$, the voltage and current relation is obtained as

$$V_p = Z_{elec\text{-}ex} I_p \tag{2.15}$$

Substituting (2.14) and (2.15) into (2.8), the device model can be obtained as

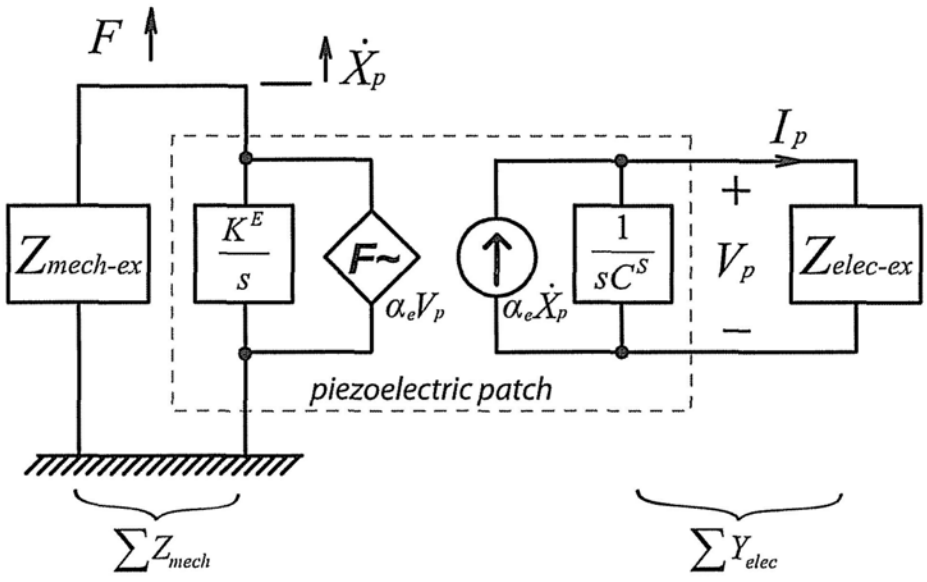

Figure 2.3: Piezoelectric device model.

$$\begin{bmatrix} F \\ 0 \end{bmatrix} = \begin{bmatrix} \sum Z_{mech} & \alpha_e \\ \alpha_e & -\sum Y_{elec} \end{bmatrix} \begin{bmatrix} \dot{X}_p \\ V_p \end{bmatrix} \tag{2.16}$$

where

$$\sum Z_{mech} = \frac{K^E}{s} + Z_{mech\text{-}ex} \tag{2.17}$$

$$\sum Y_{elec} = sC^S + Y_{elec\text{-}ex} \tag{2.18}$$

$Y_{elec\text{-}ex} = Z_{elec\text{-}ex}^{-1}$, is the external electrical admittance. Corresponding schematic diagram of the device model is illustrated in Figure 2.3.

Simplifying (2.16) yields the expression of the *total mechanical impedance* of the piezoelectric device

$$Z_{mech\text{-}total} = \frac{F}{\dot{X}_p} = \sum Z_{mech} + \alpha_e^2 Z_{elec} \tag{2.19}$$

where $Z_{elec} = (\sum Y_{elec})^{-1}$. $\alpha_e^2 Z_{elec}$ is the equivalent mechanical impedance of the electrical

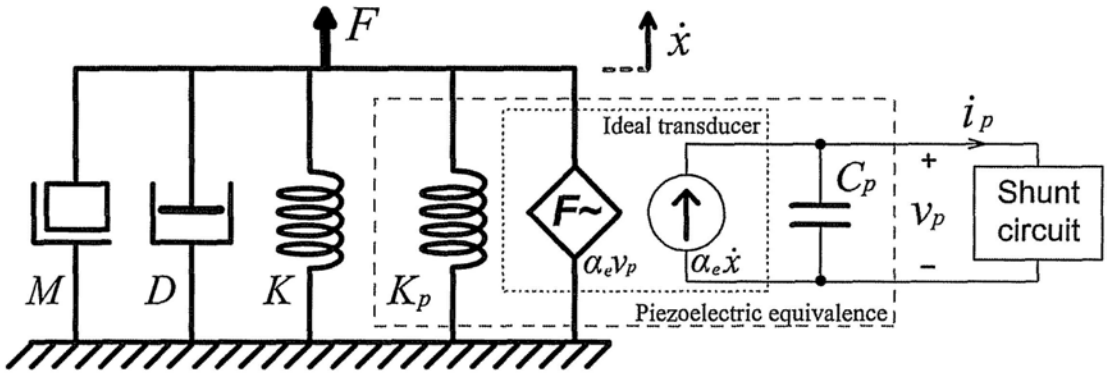

Figure 2.4: SDOF schematic representation of a piezoelectric device.

part.

Mass, spring, and damper are three basic components in an SDOF vibration system. Therefore, taking SDOF approximation, the schematic representation of a PEH device is shown in Figure 2.4 [1]. The external mechanical components include the effective mass M, the structure stiffness K, and the inherent damping D. Together with the piezoelectric short circuit stiffness K_p, the impedance of the mechanical part in the SDOF PEH device is

$$\sum Z_{mech} = Ms + D + \frac{K + K_p}{s} \tag{2.20}$$

2.3 Equivalent Circuit

With the equivalent mechanical impedance given in (2.19), the piezoelectric device can be regarded as a pure mechanical device. On the other hand, in order to study the electrical behavior of the device, we can also make the device equivalent to a pure electrical circuit. To keep voltages across and currents through all electrical elements unchanged, the equivalent circuit can be characterized, in form of the Ohm's law, as

[1] For simplicity, the notations K_p, C_p, x are substitutes for K^E, C^S, and x_p here, and also in the following chapters.

$$\frac{V_{eq}}{I_{eq}} = \frac{\sum Z_{mech}}{\alpha_e^2} + Z_{elec} \tag{2.21}$$

where V_{eq} and I_{eq} are the frequency domain expressions of the equivalent voltage and current associated with mechanical force and velocity. Their relationships in time domain were given by Warkentin and Hagood (1997) as

$$\begin{cases} v_{eq} = f/\alpha_e \\ i_{eq} = \alpha_e \dot{x} \end{cases} \tag{2.22}$$

where f is the time domain expression of the applied force. Considering the device, whose schematic was shown in Figure 2.4, (2.21) can be specified as

$$\frac{V_{eq}}{I_{eq}} = sL + R + \frac{1}{sC} + \frac{1}{sC_p + Y_{elec\text{-}ex}} \tag{2.23}$$

where

$$L = \frac{M}{\alpha_e^2} \tag{2.24}$$

$$R = \frac{D}{\alpha_e^2} \tag{2.25}$$

$$C = \frac{\alpha_e^2}{K + K_p} \tag{2.26}$$

are the equivalent inductance, resistance, and capacitance in the equivalent circuit. The capacitance C is combined with two capacitances in series. The two capacitances are related to the structural stiffness K and piezoelectric short circuit stiffness K_p with the following relations

$$C_{sturc} = \frac{\alpha_e^2}{K} \tag{2.27}$$

$$C_{Kp} = \frac{\alpha_e^2}{K_p} \tag{2.28}$$

With (2.26), the device coupling coefficient given in (2.10) and (2.12) can also be expressed as

$$k_d^2 = \frac{C}{C+C_p} \tag{2.29}$$

According to (2.23), the equivalent circuit diagram is shown in Figure 2.5(a). In the figure, v_{eq} is the equivalent voltage source representing the sinusoidal force excitation applied to the piezoelectric structure. This equivalent circuit can serve as a common base for damping analyses with both energy harvesting and energy dissipation. It depends on whether a shunt circuit designed for energy harvesting or energy dissipation is connected.

Moreover, the circuit was usually further simplified with an additional approximation that the coupling coefficient $k_d^2 \to 0$. From (2.29), such approximation results in $C_p \gg C$. Therefore, $1/(sC)$, as electrical impedance, is dominant. In this case, v_{eq} and L, R, C together form a current source i_{eq}. The simplified equivalent circuit is shown in Figure 2.5(b). This approximation under low coupling condition was acceptable in most of the previous literatures. Yet, it is not exact in fact. Because the so called device coupling coefficient is in "half device level", the influence of the electrical part cannot be included merely with this coefficient. Detailed explanation will be provided in Chapter 4.

In traditional passive damping, the simplified equivalent circuit shown in Figure 2.5(b) was seldom used, since the approximation $k_d^2 \to 0$ contradicts the purpose of extracting as much mechanical energy as possible. Hagood and von Flotow (1991) proposed an inspired analysis for shunt damping optimization, which can also be derived with the equivalent circuit in Figure 2.5(a). Later work in this area mainly focused on multiple-mode vibration damping methods (Moheimani, 2003).

In the research of energy harvesting, up to now, most of the analyses with the emphases on interface circuits were based on the simplified equivalent circuit as shown in Figure 2.5(b) (Ottman et al., 2002; Lesieutre et al., 2004; Guyomar et al., 2005; Badel et al., 2005; Mak-

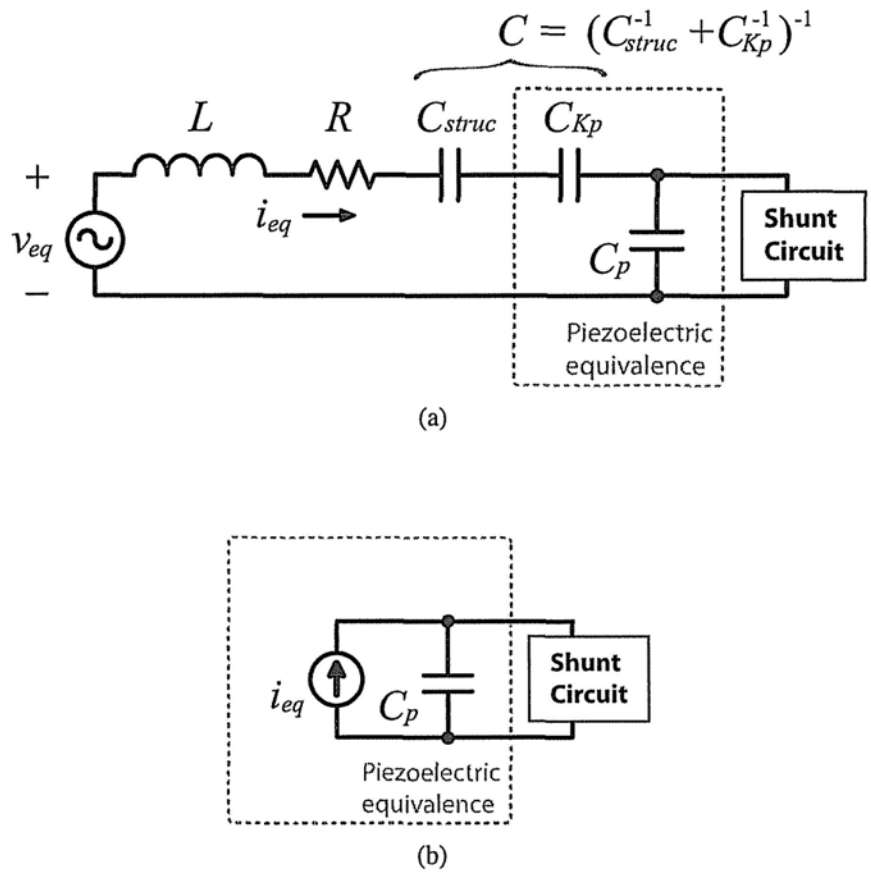

Figure 2.5: Equivalent circuit diagrams of a piezoelectric device. (a) Equivalent circuit. (b) Simplified equivalent circuit.

ihara et al., 2006; Anton and Sodano, 2007). As a result, the interaction between the shunt circuit and the mechanical structure was usually neglected. In fact, more universal analysis based on SEH circuit and the piezoelectric equivalent circuit as shown in Figure 2.5(a) was once proposed with the title "nonlinear shunt damping" (Warkentin and Hagood, 1997), before the recent research on energy harvesting.

2.4 Summary

Starting from the constitutive equations, which describe the piezoelectric characteristics at material level, the governing equations at element level were obtained with some dimensional and dynamic relations. By including the external components in both the mechani-

cal and electrical parts, the model was extended to device level, and further interpreted into equivalent circuit. Different from the simplified equivalent circuit (Figure 2.5(b)), which was often used in previous interface emphasized studies, the equivalent circuit (Figure 2.5(a)) introduced in this chapter includes the components in all the mechanical part (L, R, and C_{struc}), transducer (C_{Kp} and C_p), and the electrical part (shunt circuit); therefore, is more suitable for the analysis on the electromechanical interaction in piezoelectric devices.

By the way, in some literatures (Brufau-Penella and Puig-Vidal, 2009; Kong et al., 2010; Paganelli et al., 2010), the piezoelectric element was modeled as an ideal electrical transformer. It was somewhat misleading, because in ideal electrical transformer, both ports are current control voltage sources (CCVSs). However, since force and velocity in mechanical domain correspond to voltage and current in electrical domain, respectively, as expressed in (2.22), we can observe from Figure 2.2 that, in all of these four element level models, the primary (mechanical) ports are either voltage control voltage sources (VCVSs) ((a) & (b)) or current control current sources (CCCSs) ((c) & (d)); the secondary (electrical) ports are also either VCVSs ((b) & (c)) or CCCSs ((a) & (d)). Therefore, compared to the coupled electrical transformer model, the coupled capacitance model derived from Figure 2.2(a) better reflects the piezoelectric coupling relation between the mechanical and electrical domains.

□ End of chapter.

Chapter 3

Energy Harvesting and Dissipation on Structural Damping

Up to now, most of the researches on piezoelectric energy harvesting were mainly concerned with the absolute amount of energy that can be harvested from vibrating structures (Ottman et al., 2002; Badel et al., 2005; Anton and Sodano, 2007). The effect, which is resulted from energy harvesting and reacts to the vibrating structure, was seldom discussed in these studies. Lesieutre et al. (2004) discussed such an issue and claimed that the harvesting of electrical energy from the piezoelectric system brings out structural damping. On the other hand, it has been known for a long time that the effect of structural damping can be caused by energy dissipation. In most of the shunt damping treatments, energy dissipation was regarded as the only function that contributes to structural damping (Moheimani, 2003). In the two applications of standard energy harvesting (SEH) and resistive shunt damping (RSD), even though their main functions are energy harvesting and energy dissipation respectively, they can be compared in terms of damping capabilities (Lesieutre et al., 2004).

Referring to the comparison between the two applications, we note that it is possible that the two functions coexist in a certain condition and both have effects on structural damping. This phenomenon happens in the application of synchronized switch harvesting on inductor (SSHI). In this chapter, the relationship among the functions of energy harvesting, dissipation and their effects on structural damping will be investigated. This understanding is crucial towards an adaptive energy harvesting technique.

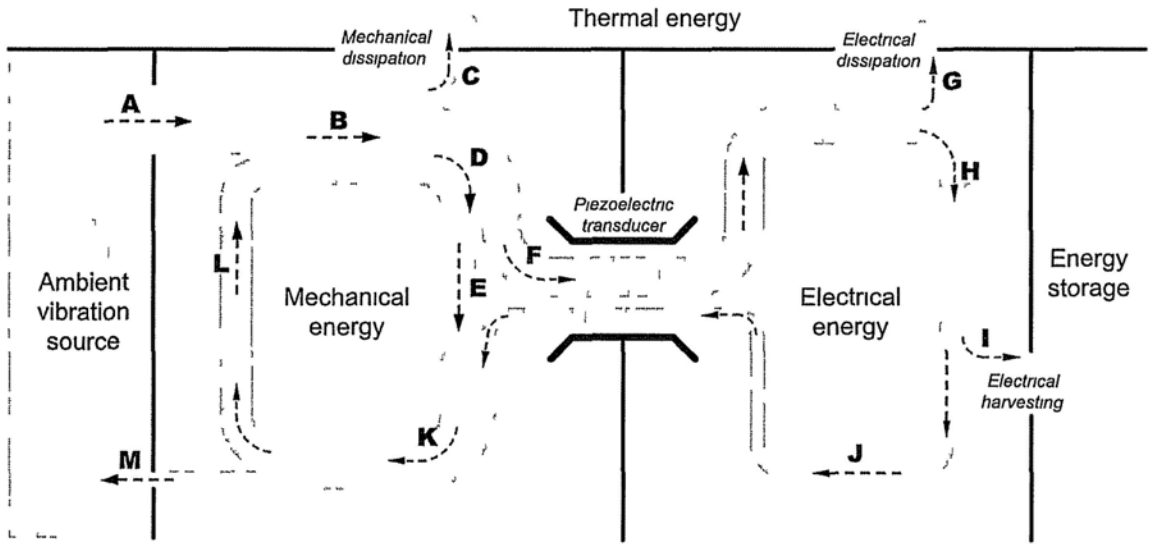

Figure 3.1: Energy flow chart in piezoelectric devices.

3.1 Energy Flow

In most of the literature, damping is the dissipation of energy of a mechanical system (Harris, 1996; de Silva, 2005), and dissipation usually means the lost energy is converted into heat (Wikipedia). However, de Silva (2005) also pointed out that damping is the process that *converts* and *dissipates* mechanical energy into other forms of energy. Considering the piezoelectric energy harvesting, which also results in structural damping, the previous definitions need to be clarified. In this section, energy flow in piezoelectric devices is studied; afterwards, terms are specified in order to investigate various effects in the following sections.

3.1.1 Overview on energy involved

The energy involved in piezoelectric devices will be clarified first. Given the piezoelectric devices, whose SDOF schematic representation was shown in Figure 2.4, regardless of the purposes of structural damping or energy harvesting, their mechanical parts in structures are similar. The main differences lie in their shunt circuits. Figure 3.1 provides an overview on three forms of energy involved in these devices. These three forms are: mechanical,

electrical, and thermal. The previous twos are linked by the bi-directional piezoelectric transducer. At the same time, either mechanical or electrical energy can be converted into thermal energy by dissipative elements such as mechanical dampers or electrical resistors. Once the energy is dissipated, i.e., transform into heat, it will not be recovered in the devices, therefore dissipative transformation is uni-directional.

The energy flow chart provides an intuitive way to indicate the directions of different branches of flow in every vibration cycle. During each cycle, the ambient excitation source inputs energy into the system in mechanical form (branch **A**). A majority of the energy keeps cycling in the mechanical domain as the vibratory energy (loop **B** - **D** - **E** - **K** - **L** - **B**). Accompanied with the vibration, some mechanical energy is directly dissipated, i.e., converted into thermal (branch **C**); while some is converted into electrical (branch **F**) with the electromechanical coupling characteristic of the piezoelectric transducer. In the electrical domain, without the shunt circuit, the electrical energy is temporarily stored in the piezoelectric capacitance and then all returns; however, with different shunt circuits connected, this electrical energy may have different destinations. Generally, there are three possible ways:

a) being converted into thermal energy (branch **G**), i.e., dissipated;

b) being stored as energy storage (branch **I**), i.e., harvested;

c) returning to the mechanical domain (branch **J**).

Finally, if the total mechanical impedance of the piezoelectric device does not match the source impedance, some energy will return to the source (branch **M**).

3.1.2 Term specification

Within all these branches, the three branches of **C**, **G**, and **I** can remove energy from the vibrating piezoelectric structure; yet, their mechanisms are different. Branch **C** is related to energy dissipation in mechanical way; it represents the function of *mechanical energy dissipation*. Branch **G** is related to energy dissipation in electrical way; it represents the function of *electrical energy dissipation*. Branch **I** scavenges the energy in electrical way; it

Table 3.1: Term Specification

Branch	Function		Effect
C	Mechanical energy dissipation	Energy dissipation	
G	Electrical energy dissipation	(dissipation factor, η_d)	Vibration damping
I	Electrical energy harvesting	Energy harvesting	(loss factor, η_Σ)
	Mechanical energy harvesting	(harvesting factor, η_h)	

represents the function of *electrical energy harvesting*. One or more of the three functions can take place in certain applications and cause the *effect* of structural damping. Table 3.1 gives the terms specification for four functions that can remove mechanical energy from vibrating structures. To have a complete classification, this table includes the forth item, *mechanical energy harvesting*. For example, in automatic watches, with elaborate designed mechanism, mechanical energy can be stored in the mainsprings to drive the watches. This technique has already been successfully applied for more than 80 years.

With the above specification, when considering the damping applications, e.g., RSD, we emphasize on the total effect of the involved functions to the structure. On the other hand, when considering the applications of energy harvesting, e.g., SEH or SSHI, we focus on the utilization of the electrical energy harvesting function. However, it does not mean that there is no other function in the system. On the contrary, in the applications of energy harvesting, parasitic mechanical and electrical energy dissipations usually exist. In general, they were not considered in most of the previous literatures. But since they partake and dissipate some of the energy that could be harvested, these functions would become important for the purpose of harvesting energy from vibration sources while exploitable energy is limited.

The three factors within the parentheses in Table 3.1 are indices to evaluate the corresponding functions or effect. For traditional damping, the term *loss factor* was usually used to evaluate the total damping capability. It was defined as the ratio between the energy dissipated per cycle and the energy associated with vibration (Warkentin and Hagood, 1997).

Here, in order to continue using this term for damping evaluation, we make a subtle change in this old definition. The new defined loss factor is the ratio between the energy removed per cycle and the energy associated with vibration. Moreover, considering energy harvesting, it is not enough to show the detailed energy relations with the use of loss factor only. Therefore, two additional factors are defined with respect to energy harvesting and energy dissipation as follows.

For energy harvesting, the new term *harvesting factor* is defined to evaluate the harvesting capability as

$$\eta_h = \frac{E_h}{2\pi E_{max}} \tag{3.1}$$

where E_h denotes the harvested energy in one cycle (branch **I**), E_{max} is the energy associated with vibration (branch **K**, the total cycling energy), multiplying by 2π to obtain the vibratory energy in one cycle. For energy dissipation, the term *dissipation factor* is used to evaluate the dissipation capability as

$$\eta_d = \frac{E_d}{2\pi E_{max}} \tag{3.2}$$

where E_d is the dissipated energy in one cycle (branch **C** and **G**). With (3.1) and (3.2), we can define the *loss factor* as

$$\eta_\Sigma = \frac{\Delta E}{2\pi E_{max}} = \eta_h + \eta_d \tag{3.3}$$

where ΔE is the summation of E_h and E_d, which represents the total removed energy from the vibrating structure in one cycle. The loss factor is related to the capability on vibration damping, which is the combined effect of both energy harvesting and dissipation.

3.2 Energy Harvesting and Dissipation

Besides a majority of literature studying absolute energy or power that can be harvested from an ideal current source, Lesieutre et al. (2004) have discussed the structural damping effect due to energy harvesting in the application of SEH. In terms of damping capability,

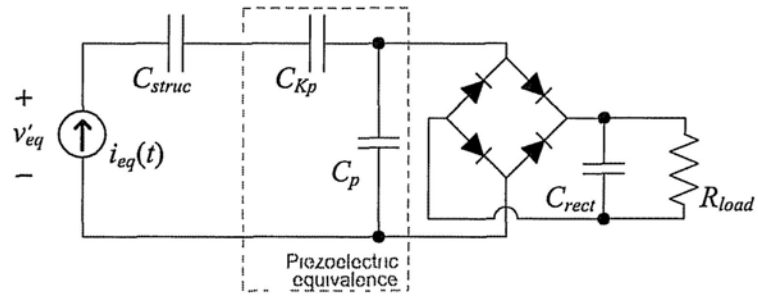

Figure 3.2: Equivalent circuit for standard energy harvesting (SEH).

which is evaluated by the loss factor, this effect can be compared to RSD. The comparison made by Lesieutre et al. (2004) was only valid under the condition that $k_d^2 \to 0$ (Shu and Lien, 2006*b*). In this section, brief review on the optimizations of SEH and RSD will be firstly given; afterwards, general comparisons covering the whole range of k_d^2 will be made to evaluate the electrical induced damping in SEH and RSD [1].

3.2.1 Standard energy harvesting

In the SEH application, only the energy harvesting function contributes to the effect of structural damping [2]. The shunt circuit is a nonlinear circuit, which is composed of a bridge rectifier, a filter capacitor, and the DC load in parallel. Under constant displacement excitation, its equivalent circuit is shown in Figure 3.2. The current source i_{eq} is made up of the voltage source v_{eq}, the equivalent inductance L, and the equivalent resistance R in Figure 2.5(a). The voltage across the current source is denoted as v'_{eq}. In analyzing this circuit, the filter capacitor C_{rect} is assumed to be large enough so that the voltage across this capacitor V_{rect} is nearly constant (Ottman et al., 2002). For the "nonlinear damping" circuit proposed by Warkentin and Hagood (1997), it differs from the circuit of Figure 3.2 in that the C_{rect} is replaced by a constant DC voltage supply. Yet, their analyses are compatible.

[1] Since the mechanical damping is subjected to the main structure, the purpose of this chapter is to consider the correlation between the functions of electrical harvesting, electrical dissipation, and their effect on structural damping (electrical induced damping). The mechanical damping is excluded from the analysis.

[2] Ideal bridge rectifier is assumed, i.e., its forward voltage drop equals to zero.

The ratio between the harvested energy and energy associated with vibration in one cycle, which is called *harvesting factor* here, is a function of k_d^2 and $\tilde{V}_{rect}$ (Warkentin and Hagood, 1997)

$$\eta_h = \frac{4}{\pi}\tilde{V}_{rect}\frac{1-\tilde{V}_{rect}}{\frac{1-k_d^2}{k_d^2}+\tilde{V}_{rect}} \tag{3.4}$$

where $\tilde{V}_{rect}$ is obtained by non-dimensionalizing the rectified voltage to the amplitude of open circuit voltage, i.e.,

$$\tilde{V}_{rect} = \frac{V_{rect}}{V_{OC}} \tag{3.5}$$

The open circuit voltage V_{OC} is related to the maximum displacement amplitude X with the following relation

$$V_{OC} = \frac{\alpha_e X}{C_p} \tag{3.6}$$

The coupling coefficient of the piezoelectric device depends on material and geometry properties, which cannot be changed after the device is made. The maximum harvesting factor can be obtained as follows

$$\eta_{h,max} = \frac{4}{\pi}\frac{\left(1-\sqrt{1-k_d^2}\right)^2}{k_d^2} \tag{3.7}$$

at a non-dimensional rectified voltage

$$\tilde{V}_{rect,opt} = \frac{1-k_d^2}{k_d^2}\left(\sqrt{\frac{1}{1-k_d^2}}-1\right) \tag{3.8}$$

The optimum rectified voltage can be achieved by properly choosing the load. This load can be an adaptive DC-DC converter (Ottman et al., 2002) or optimal resistor (Guyomar et al., 2005). The extracted power is transferred or consumed so as to keep the optimum rectified voltage constant. In addition, it can be proven that when $k_d^2 \to 0$, $\tilde{V}_{rect,opt} = 0.5$,

which is the optimal result given by Ottman et al. (2002). In their study on the damping effect of SEH, Lesieutre et al. (2004) took $\tilde{V}_{rect,opt}$ as constant, i.e., equals to 0.5, regardless of k_d^2, therefore, their optimum non-dimensional rectified voltage and maximum harvesting factor [3] are only valid when $k_d^2 \to 0$.

3.2.2 Resistive shunt damping

In the application of RSD (Hagood and von Flotow, 1991), only the energy dissipation function contributes to the effect of structural damping. The equivalent circuit is shown in Figure 3.3. It only connects a resistor as its shunt circuit to dissipate the extracted energy, thus results in damping. The dissipation factor is given by

$$\eta_d = \frac{\rho\, k_d^2}{1 - k_d^2 + \rho^2} \tag{3.9}$$

where ρ is the non-dimensional frequency

$$\rho = \omega R_{RSD} C_p \tag{3.10}$$

and ω is the excitation angular frequency, R_{RSD} is the resistance of the shunt resistor. The maximum dissipation factor can be obtained as follows

$$\eta_{d,max} = \frac{k_d^2}{2\sqrt{1 - k_d^2}} \tag{3.11}$$

at a non-dimensional frequency of

$$\rho_{opt} = \sqrt{1 - k_d^2} \tag{3.12}$$

[3] Loss factor was used in their study. In this thesis, harvesting factor is used instead while loss factor was defined in Section 3.1.

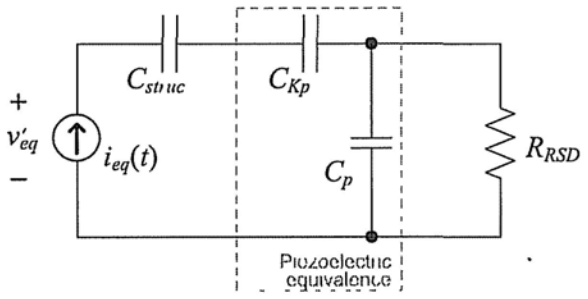

Figure 3.3: Equivalent circuit for resistive shunt damping (RSD).

3.2.3 Comparison between SEH and RSD

To compare the characteristics between SEH and RSD, we employ the non-dimensional charge-voltage diagrams to illustrate their energy conversion cycles.

Since the equivalent current in Figure 2.5(a) equals to $\alpha_e\dot{x}$, the equivalent charge input is the integral of this current, which is $\alpha_e x$. Assuming X as the maximum displacement, the maximum equivalent input charge should be $\alpha_e X$. Non-dimensionalizing $\alpha_e x$ with $\alpha_e X$, we have

$$\tilde{q}_p = \frac{\alpha_e x}{\alpha_e X} = \frac{x}{X} = \tilde{x} \tag{3.13}$$

It is not only the non-dimensional input charge $\tilde{q}_p$, but also the non-dimensional displacement $\tilde{x}$ induced by the mechanical source. Similarly, we can also non-dimensionalize the equivalent voltage across the current source in Figure 3.2 and Figure 3.3, $v'_{eq} = F'/\alpha_e$, with respect to the maximum voltage across C, i.e., C_{struc} and C_{Kp} in series,

$$\tilde{v} = \frac{v'_{eq}}{\alpha_e X/C} = \frac{F'}{(K+K_p)X} = \tilde{F} \tag{3.14}$$

The non-dimensional equivalent voltage $\tilde{v}$ is also the non-dimensional force $\tilde{F}$ applied to the corresponding mechanical components.

Given the situation that $k_d^2 = 0.3$, for instance, the energy conversion cycles for SEH with optimum $\tilde{V}_{rect}$ and RSD with optimum ρ are shown in Figure 3.4 and Figure 3.5, respectively. The black solid curve in either diagram shows the relation between non-dimensional

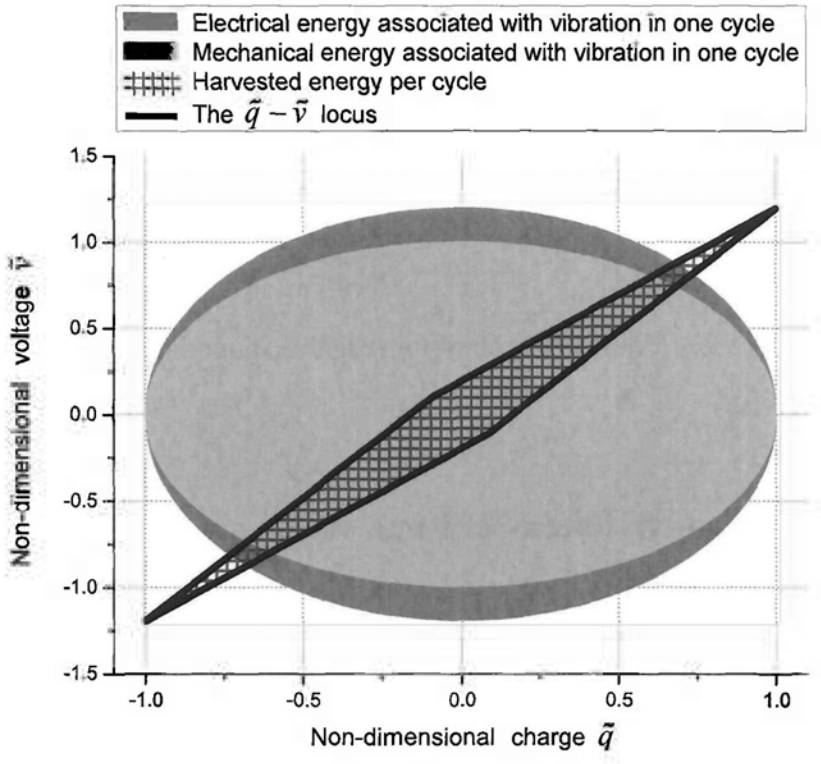

Figure 3.4: Energy cycle for standard energy harvesting (SEH).

charge and non-dimensional voltage in one cycle. The areas of blue and green ellipses represent 2π multiplying the maximum stored energy in the devices: blue for electrical and green for mechanical [4]. The areas enclosed by the $\tilde{q}-\tilde{v}$ loci represent the energy removed from the structures in one cycle. But in order to distinguish whether the extracted energy is harvested or dissipated, different patterns are used in the diagrams.

The main differences between Figure 3.4 and Figure 3.5 are the shapes of the $\tilde{q}-\tilde{v}$ loci and the patterns that fill the areas enclosed by the loci. But even the flows of the extracted energy in these two applications are different, they can be compared in terms of damping capability, which is evaluated by the loss factor. Without energy being dissipated, the harvesting factor in SEH is also the loss factor; similarly, without energy being harvested, the dissipation factor in RSD is also the loss factor.

[4] For gray scale printing, the electrical and mechanical energy is represented by darker and lighter gray patches, respectively.

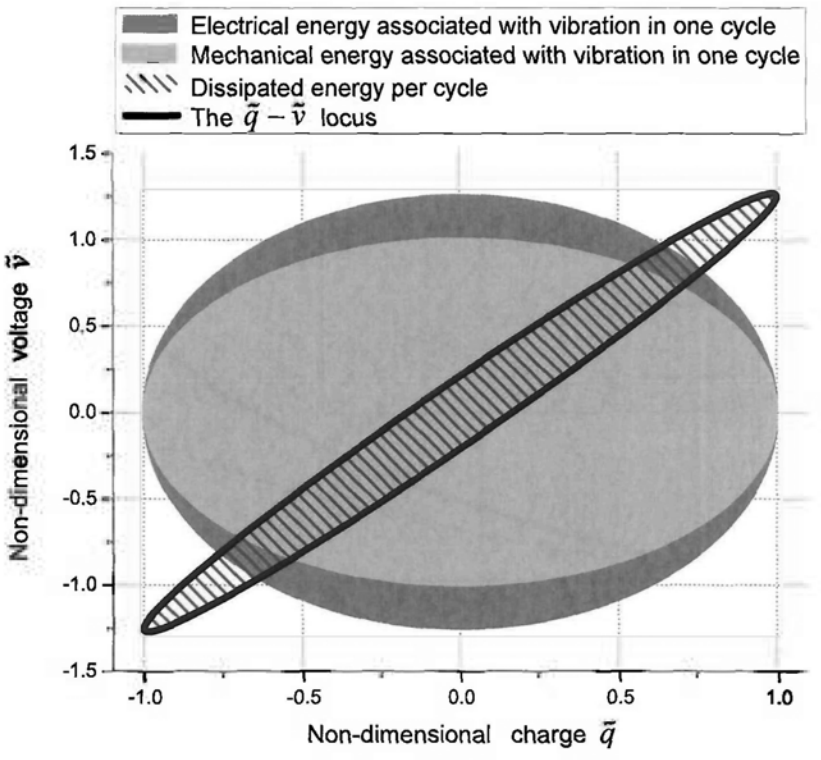

Figure 3.5: Energy cycle for resistive shunt damping (RSD).

According to the relations given in (3.7) and (3.11), the two maximum loss factors, i.e., $(\eta_{\Sigma,max})_{SEH}$ and $(\eta_{\Sigma,max})_{RSD}$, in the two applications, as functions of k_d^2, are compared in Figure 3.6. As k_d^2 increases, the attainable maximum loss factors for both applications increase; besides, the ratio between the two factors of SEH and RSD decreases. Moreover, it should be noted that, when coupling coefficient of the piezoelectric element approaches zero, we can obtain

$$\lim_{k_d^2 \to 0} \frac{(\eta_{\Sigma,max})_{SEH}}{(\eta_{\Sigma,max})_{RSD}} = \frac{2}{\pi} = 63.66\% \tag{3.15}$$

which can also be observed from the dot curve in Figure 3.6. Lesieutre et al. (2004) had come to the same result under this special condition. Indeed most of the previous analyses on SEH took $k_d^2 \to 0$ as their premise, explicitly or implicitly. This premise constrains the endeavor to increase the material coupling in order to harvest more energy. It simplifies the analysis; however, it confines the optimization in specific, rather than general, conditions.

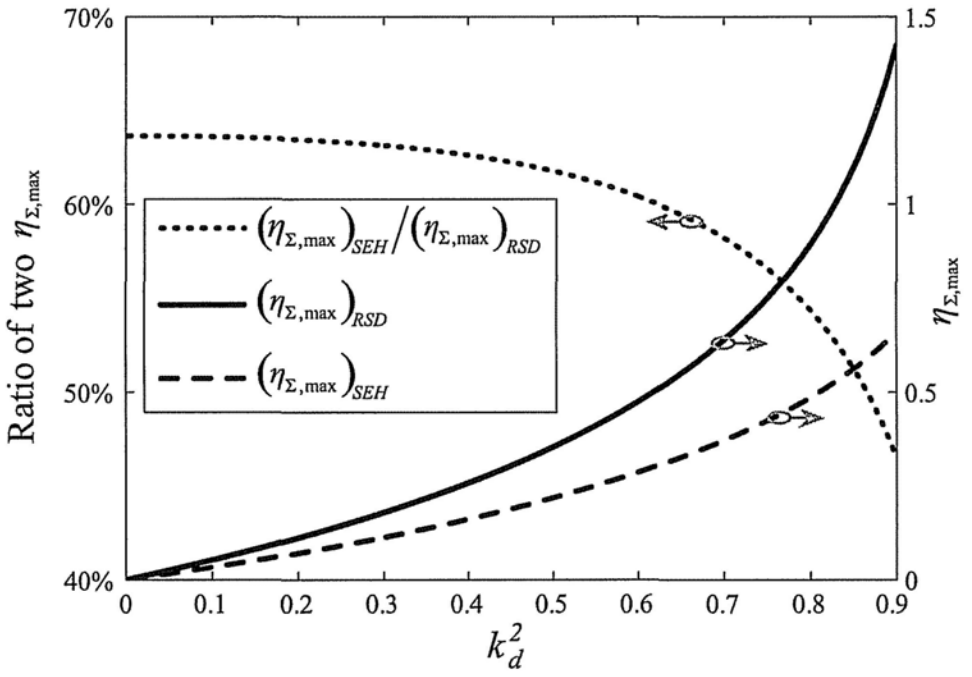

Figure 3.6: Maximum loss factors in two applications and their ratio.

3.2.4 Experimental verification

Experiments are performed, in order to verify the relationship between harvesting factor and non-dimensional rectified voltage $\tilde{V}_{rect}$ in the standard energy harvesting application, as given in (3.4); as well as the relationship between dissipation factor and non-dimensional resistance ρ in the resistive shunt damping application, as given in (3.9).

SEH

For standard energy harvesting, the experimental setup is shown in Figure 3.7. One end of a commercial piezoelectric bimorph (QuickPack QP20W, Midé Technology) is fixed on a shaker (Mini Shaker Type 4810, Brüel & Kjær) to form a base-driven cantilever. In order to enhance the vibration at low frequency, a proof mass is mounted at the other end of the bimorph. It is measured that this piezoelectric cantilever has a natural frequency of 21.5 Hz at open circuit and 20.6 Hz at short circuit. Thus, with (2.10) the device coupling coefficient k_d^2 is around 8.20%. The two layers of the bimorph are connected in series, and

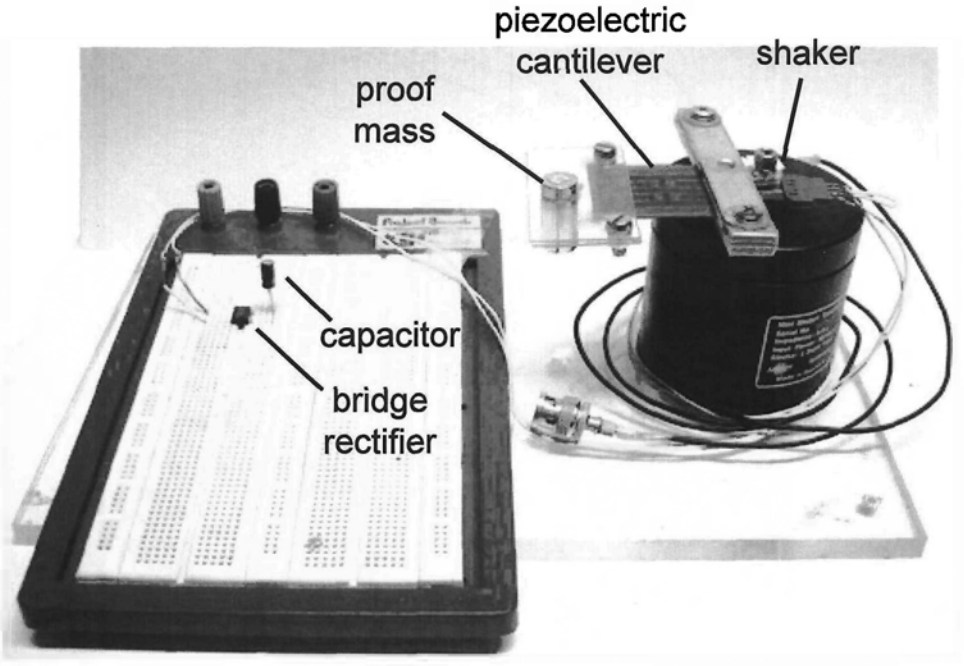

Figure 3.7: Experimental setup for standard energy harvesting.

a capacitance of 42 nF is measured. To harvest energy, the two electrodes are connected to the AC input port of a bridge rectifier, whose DC output port is connected to a capacitor for energy storage.

A 25 Hz excitation signal is provided to the shaker. Its amplitude is adjusted until the open circuit voltage, i.e., V_{OC}, of the piezoelectric patch reaches 25 V. To obtain the harvested energy per cycle, i.e., E_h in (3.1), with respect to different rectified voltage, the voltage rising across the storage capacitor is captured with a sampling frequency of 1kHz. Figure 3.8 shows the voltage histories for charging three different capacitors, respectively. Their capacitance values are 10 μF (measured 10.04 μF), 22 μF (measured 22.64 μF) and 33 μF (measured 30.94 μF). It can be seen from the figure that, the smaller in value of storage capacitor, the quicker to be charged up. The obtained data is then processed in PC with Matlab. Assuming the mean voltage across the storage capacitor within an interval to be constant during charging, the harvesting power under this V_{rect} value can be obtained, because the energy input of the capacitor within such interval can be estimated according to the voltage change. However, there is a problem that the estimating interval should be

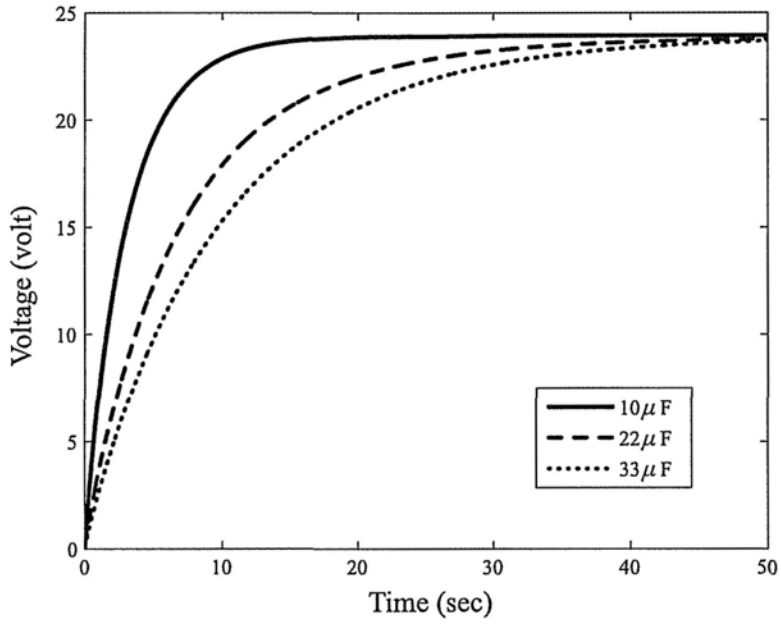

Figure 3.8: Time histories of voltage with different storage capacitors.

chosen carefully. If it is too long, the constant voltage assumption would be invalid; on the contrary, if it is too short, the voltage across the capacitor can hardly change. We overcome this problem with an "adaptive interval algorithm". Generally, shorter interval for lower V_{rect} and longer one for higher V_{rect}, since the voltage changes more shapely at low V_{rect}.

To calculate the harvesting factor, there is still another challenge. Since the cantilever does not vibrate with constant displacement in the charging process, to estimate the loss factor, we need to know E_{max} in (3.1). This vibration energy is related to the maximum displacement in one vibration cycle. Therefore, an inductive displacement sensor (JCW-24SR, CNHF Co.) is used here to measure the displacement of the cantilever, so that we can adjust the estimation of E_{max} with the changing displacement.

Since the harvesting factor is also the loss factor in the standard energy harvesting, Figure 3.9(a) shows the relation between the loss factor and non-dimensional rectified voltage in this application. According to (3.4), the solid curve shows the theoretical result with an ideal bridge rectifier. The three sorts of discrete marks are experimental results obtained from the corresponding voltages. Three of them are in good agreement, but all are lower

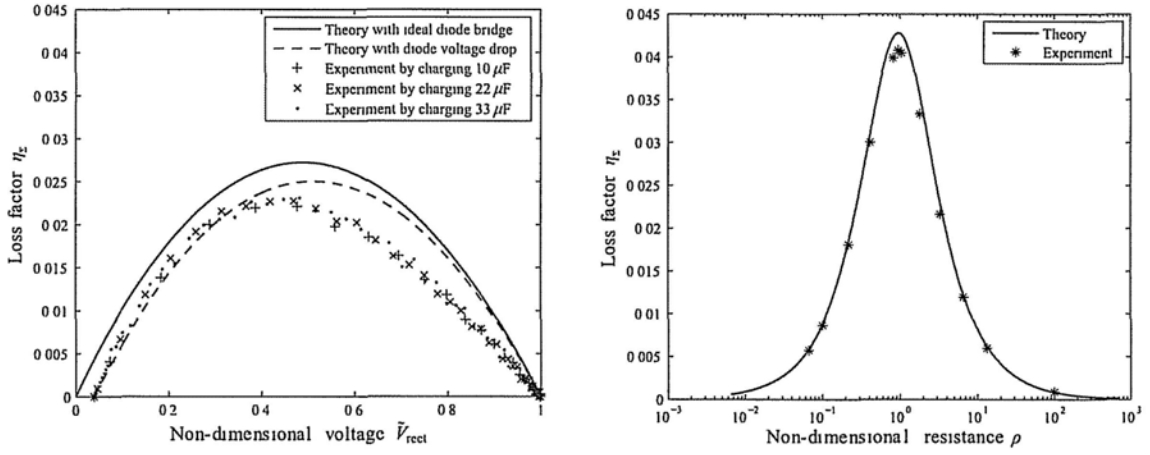

(a) (b)

Figure 3.9: Theoretical and experimental loss factors in two applications. (a) Standard energy harvesting. (b) Resistive shunt damping.

than the solid theoretical curve. This difference may be due to the non-ideal behavior of the diode bridge and nonideal sinusoidal current output from the piezoelectric patch [5]. To compensate this, a revisory factor considering the voltage drop across the rectifier is introduced, which is

$$\lambda = \frac{V_{rect} - V_F}{V_{rect}}, \tag{3.16}$$

where V_F is the forward voltage drop of the bridge rectifier. The V_F is 1.0 V for the bridge rectifier we used in this experiment. Multiplying (3.4) by λ yields the dash curve in Figure 3.9(a). It is closer to the experimental results than the solid one.

RSD

For the experiment on resistive shunt damping, the mechanical part of the setup is the same as that for the standard energy harvesting. The difference is to replace the bridge rectifier and the storage capacitor with a resistor.

[5] In our experiment, we found the lower the excitation frequency, the more deformation the open circuit voltage of this piezoelectric patch. In particular, for frequencies below 20 Hz, the output can hardly be regarded as sinusoidal.

With the same excitation frequency, several chosen resistors at different values are connected to the piezoelectric patch one after another. For different shunt resistors, the displacement of the cantilever is adjusted to the same level according to the output of the displacement sensor, in order to have constant displacement excitation. With the RMS voltages across different resistors, we can calculate how much power is consumed by every single shunt resistor, and then the dissipation factor can be obtained.

As no energy is harvested in the application of resistive shunt damping, the dissipation factor here is also the loss factor. Figure 3.9(b) shows the loss factor as a function the non-dimensional shunt resistance, both theoretically and experimentally. The two results show good agreement with each other.

As discussed above, even the energy flows in the two applications of standard energy harvesting and resistive shunt damping are different, they both extract energy from the vibrating mechanical structure, thus result in structural damping. Figure 3.9(a) and (b) provide a comparison on the damping capabilities of these two applications at the condition of $k_d^2 = 8.20\%$. The results verify that the ratio of $(\eta_{\Sigma,max})_{SEH}$ to $(\eta_{\Sigma,max})_{RSD}$ is about 60% at low coupling conditions.

3.3 Energy Harvesting and Dissipation of SSHI

In the previous two applications, either has only one dominant function that contributes to the effect of structural damping. In the application of SSHI, situation is more complicated. Both of the two functions, energy harvesting and energy dissipation, coexist in this application, and bring out damping effect. Previous researches on SSHI were conducted for the only purpose of harvesting energy; nevertheless, unlike the application of SEH, considering its contribution to structural damping, the function of energy harvesting may not be dominant in all situations. Detailed study on the relationship among energy harvesting, dissipation and their effects on SSHI can help us better understand the energy flow and conversion mechanism within the piezoelectric devices.

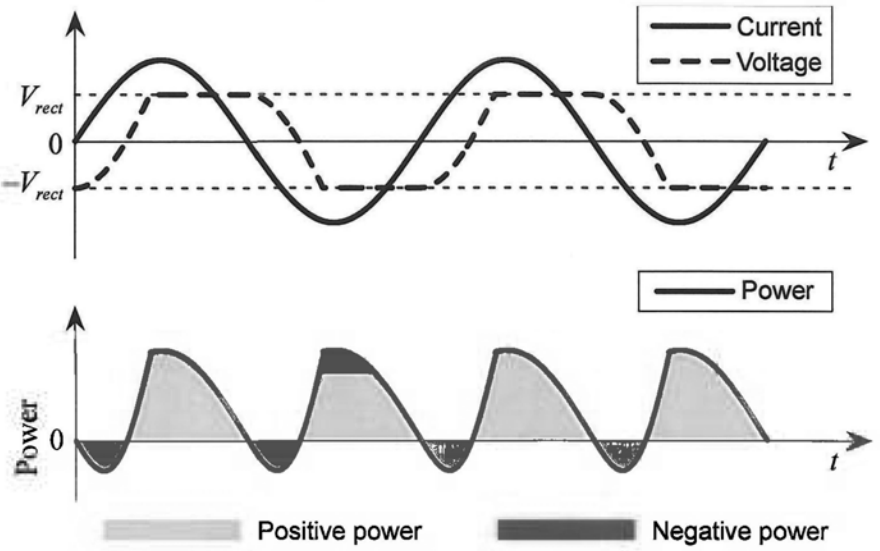

Figure 3.10: Typical voltage, current and power waveforms in standard energy harvesting (SEH).

3.3.1 The SSHI technique

The technique of SEH provides a passive solution to harvest ambient vibration energy. It is simple and reliable; however, its harvesting capability is difficult to be further enhanced. As the electrical part of the device is composed of C_p in parallel with the shunt circuit, Figure 3.10 shows the typical waveforms of the voltage across it, i.e., v_p, the current flowing into it, i.e., i_{eq}, and its power input (product of v_p and i_{eq}). In most of a cycle, the power is positive, which means that energy is converted from mechanical into electrical; but in some intervals, it has negative value, which indicates the energy returns from electrical part to mechanical part. We call this *energy return phenomenon.*

In order to enhance the energy conversion efficiency, Guyomar et al. (2005) proposed a solution called *synchronized switch harvesting on inductor* (SSHI) (Badel et al., 2005; Shu et al., 2007). The equivalent circuit and typical voltage, current, power waveforms of this technique are shown in Figure 3.11 and Figure 3.12, respectively. The circuit in Figure 3.11 was further specified as "parallel-SSHI" by Lefeuvre, Badel, Petit, Richard and Guyomar (2006). By involving the shunt path composed of an active switch *sw* and a small inductor L_i, with appropriately controlling the switch, this circuit can overcome the energy return

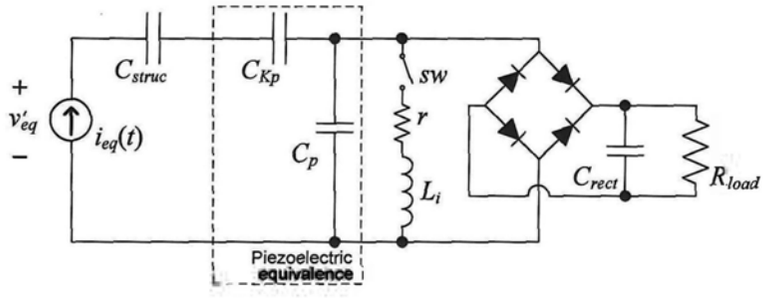

Figure 3.11: Equivalent circuit for energy harvesting with SSHI technique.

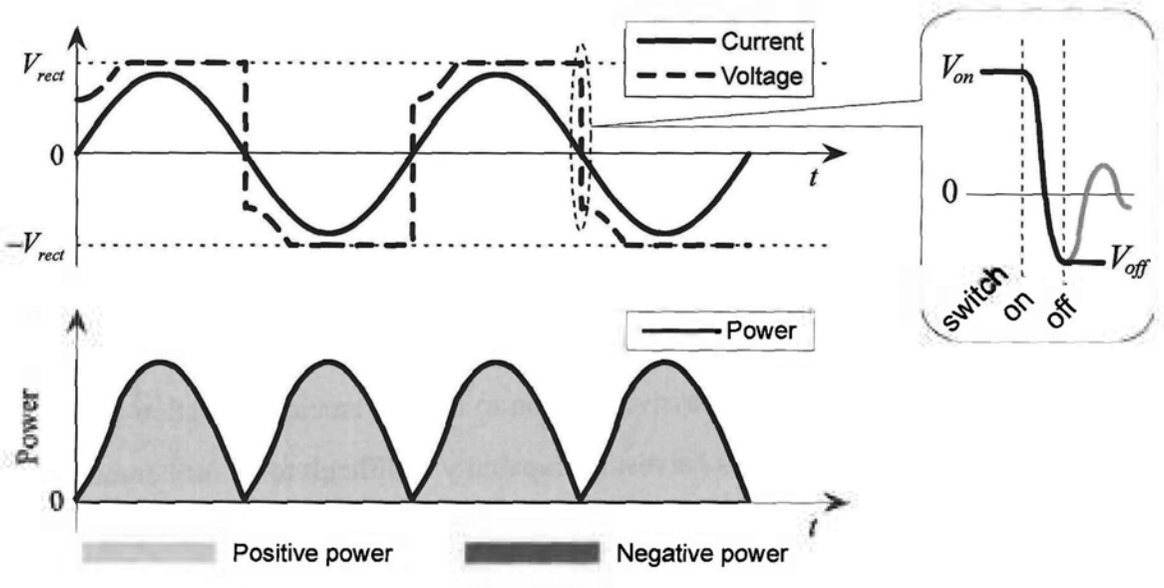

Figure 3.12: Typical voltage, current and power waveforms in energy harvesting with SSHI technique.

phenomenon so as to make sure the power always flows into the electrical part. All energy converted from mechanical to electrical is either harvested or dissipated. Therefore, the vibratory energy is only composed of mechanical energy. The energy flow chart for SSHI is shown in Figure 3.13. The electromechanical transduction in this figure is a one way process, which is different from the one in Figure 3.1.

The switch is off in most of a cycle; it takes action at the time when the current equals to zero. Also at this instant, the charge stored in C_p is at its extreme value. During the operation, the switch is first turned on to create a "shortcut" for the charge stored in C_p,

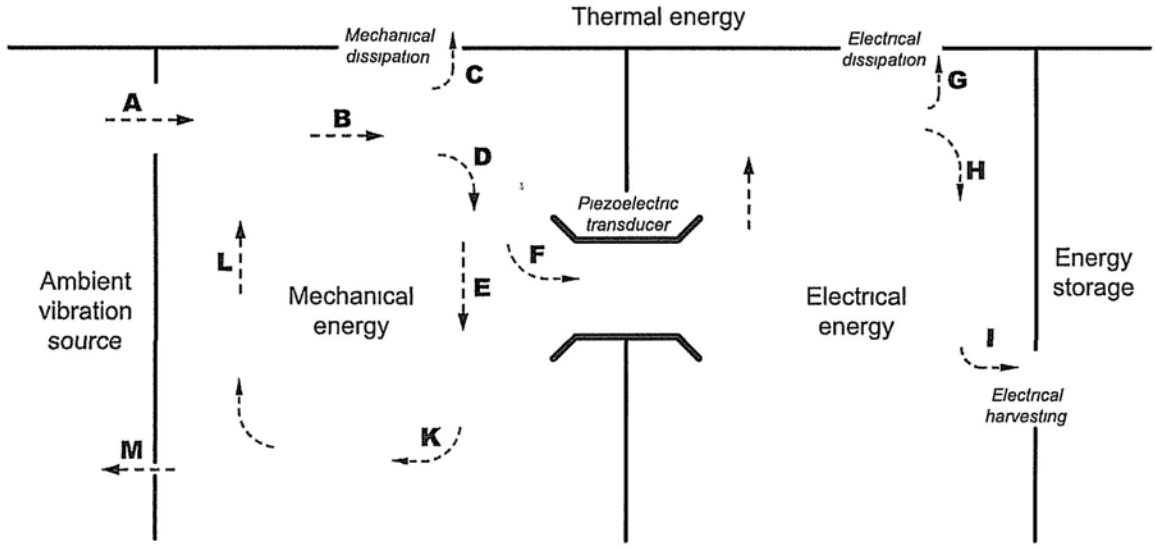

Figure 3.13: Energy flow chart of PEH devices with SSHI technique.

and then turned off to disconnect the shortcut again when the voltage across C_p alters to another extreme value. Since the electrical cycle, which is decided by the time constant $L_i C_p$, is much shorter than the mechanical cycle. The response time can be neglected, so the voltage waveform can be regarded as changing from V_{on} to V_{off} steeply at the instant when the current equals to zero. The zoom-in view of the action instant is also shown in Figure 3.12.

3.3.2 Voltage inversion factor

Most references on SSHI gave the relation between V_{off} and V_{on} in terms of electrical quality factor Q. In order to make a more general representation, we take *voltage inversion factor* as

$$\frac{V_{off}}{V_{on}} = \gamma, \quad -1 < \gamma \leqslant 0 \text{ or } \gamma = 1 \tag{3.17}$$

When $\gamma = 1$, it represents the SEH. When γ is negative, it can represent energy harvesting with SSHI technique under any electrical quality factor Q. During an inversion in SSHI, the switch is first closed to enable a LCR loop, and then naturally blocked again after half of a

LCR cycle, i.e.,

$$\tau = \pi \sqrt{L_i C_p} \tag{3.18}$$

so that the voltage across the capacitance changes at a short interval τ, which is much smaller than the mechanical cycle, with the factor of

$$\gamma = -e^{-\pi/(2Q)} \tag{3.19}$$

For a practical inductor, there is always parasitic resistance, which is denoted as r in Figure 3.11. If no additional energy is provided to the C_p and "shortcut" loop, γ can never reach -1.

3.3.3 Coexistent harvesting and dissipation

Most of the researches on harvesting with SSHI technique focused on the optimization in order to harvest more energy from the mechanical source (Guyomar et al., 2005; Badel et al., 2005; Lefeuvre, Badel, Petit, Richard and Guyomar, 2006; Shu and Lien, 2006*a*; Shu et al., 2007), while the electrical energy dissipation was considered in the simulation by Badel et al. (2005). Till now, no further analytical result is given, especially on the relationship between energy harvesting and energy dissipation in this application.

As mentioned above, the functions of energy harvesting and energy dissipation are coexistent in this application. In each cycle, some of the electrical energy is harvested and preserved in the storage device, e.g., C_{rect}; while some of it is dissipated in r during the switch action interval and also in the bridge rectifier. The first energy dissipation corresponds to the voltage change from V_{on} to V_{off} across C_p ; the second is due to the voltage drop across the rectifier, i.e., V_F.

The amount of energy harvested in one cycle is

$$E_h = 2C_p(V_{rect} - V_F)\left[2V_{OC} - V_{rect}(1+\gamma)\right] \tag{3.20}$$

The amount of energy dissipated in one cycle is

$$E_d = C_p V_{rect}^2 \left(1-\gamma^2\right) + 2C_p V_F \left[2V_{OC} - V_{rect}\left(1+\gamma\right)\right] \tag{3.21}$$

The first item in (3.21) represents the energy dissipation in r during the switch action interval; the second item results from the voltage drop across the bridge rectifier V_F.

Besides, when $\gamma \leqslant 0$, no energy returns from the electrical part to the source. The energy associated with vibration only includes the strain energy, which is

$$E_{max} = \frac{aC^S V_{oc}^2}{2} \tag{3.22}$$

where a stands for the ratio of

$$a = \frac{1-k_d^2}{k_d^2} \tag{3.23}$$

The relations among E_h, E_d and $2\pi E_{max}$ can be illustrated in the non-dimensional charge-voltage diagram. Since the mechanical part of the device, which is represented by C_{struc} and C_{Kp} in the equivalent circuit, is in series with the electrical part of the device, the charge flowing through both parts is the same. Given $k_d^2 = 0.3$, $\gamma = -0.2$ ($Q \approx 1.0$), and $\tilde{V}_{rect} = 0.8$, the charge-voltage diagrams of the mechanical and electrical parts are shown in Figure 3.14(a) and (b), respectively. Combining the charge-voltage diagrams of the mechanical part and electrical part, and referring to (3.20) $\sim$ (3.22), the charge-voltage diagram of the whole equivalent circuit is shown in Figure 3.14(c), with different patterns to indicate different branches of energy flow. The steep voltage changes at maximum charge enable the charge-voltage locus to enclose more area. Compared with the SEH and RSD, whose energy conversion cycles are shown in Figure 3.4 and Figure 3.5, energy harvesting with SSHI technique is capable to extract more energy in one cycle. Within a cycle, some of the extracted energy is converted into heat, i.e., dissipated, while the rest is harvested and kept in some suitable electrical energy storage devices (Sodano et al., 2005*a*,*b*; Guan and Liao,

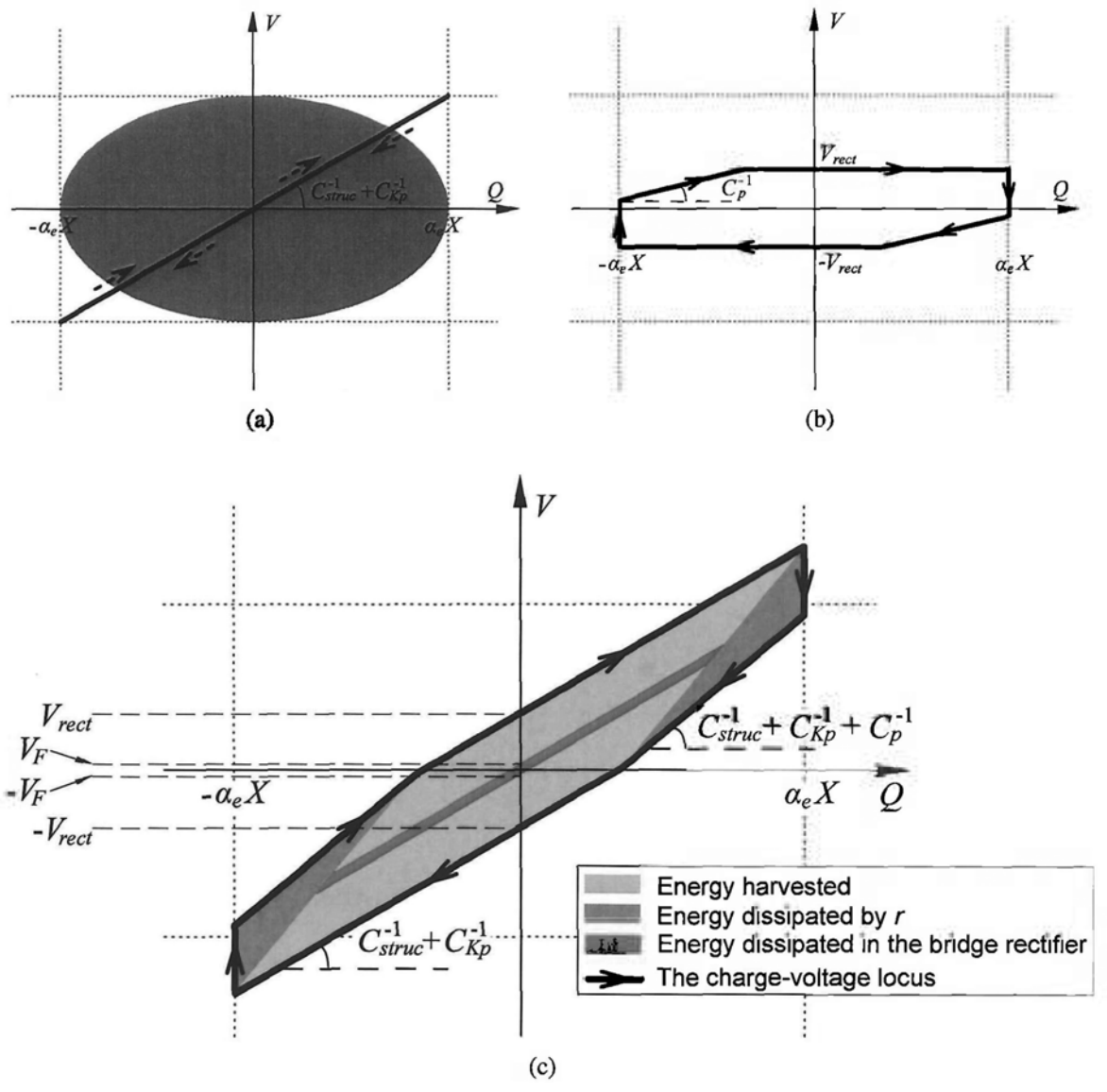

Figure 3.14: Charge-voltage diagrams of the equivalent circuit of SSHI. (a) Mechanical part. (b) Electrical part. (c) Combination.

2007, 2008).

Substituting (3.20) $\sim$ (3.22) for E_d, E_h and E_{max} into (3.1) and (3.2), the harvesting factor and dissipation factor of this device can be obtained as

$$\eta_h = \frac{2(\bar{V}_{rect} - \bar{V}_F)\left[2 - \bar{V}_{rect}(1+\gamma)\right]}{a\pi} \tag{3.24}$$

$$\eta_d = \frac{\tilde{V}_{rect}^2\left(1-\gamma^2\right)+2\tilde{V}_F\left[2-\tilde{V}_{rect}\left(1+\gamma\right)\right]}{a\pi} \tag{3.25}$$

where $\tilde{V}_{rect}$ is given by (3.5); $\tilde{V}_F$ is the non-dimensional rectified voltage drop give by

$$\tilde{V}_F = \frac{V_F}{V_{OC}} \tag{3.26}$$

According to (3.3), the loss factor η_Σ is the sum of η_h and η_d

$$\eta_\Sigma = \frac{4\tilde{V}_{rect}-\tilde{V}_{rect}^2\left(1+\gamma\right)^2}{a\pi} \tag{3.27}$$

In addition, since the harvesting factor η_h given in (3.24) and the loss factor η_Σ given in (3.27) should not be negative, therefore, there is a practical range of $\tilde{V}_{rect}$, which is

$$\tilde{V}_F \leqslant \tilde{V}_{rect} \leqslant \frac{2}{1+\gamma} \tag{3.28}$$

In this interval, when k_d^2 and γ are fixed, η_d and η_Σ monotonously increase with $\tilde{V}_{rect}$; yet, η_h is non-monotonic function. The maximum value of η_h can be obtained

$$\eta_{h,max} = \frac{1}{a\pi}\left[\frac{2}{1+\gamma}-2\tilde{V}_F+\frac{(1+\gamma)\tilde{V}_F^2}{2}\right] \tag{3.29}$$

at an optimum non-dimensional rectified voltage

$$\tilde{V}_{rect,opt} = \frac{1}{1+\gamma}+\frac{\tilde{V}_F}{2} \tag{3.30}$$

When the open circuit voltage V_{OC} is much larger than the forward voltage drop of the bridge rectifier, i.e., V_F, the second item in $\tilde{V}_{rect,opt}$ can be neglected. It should be also noted that, the optimum rectified voltages for maximum harvesting factor are one half of its applicable

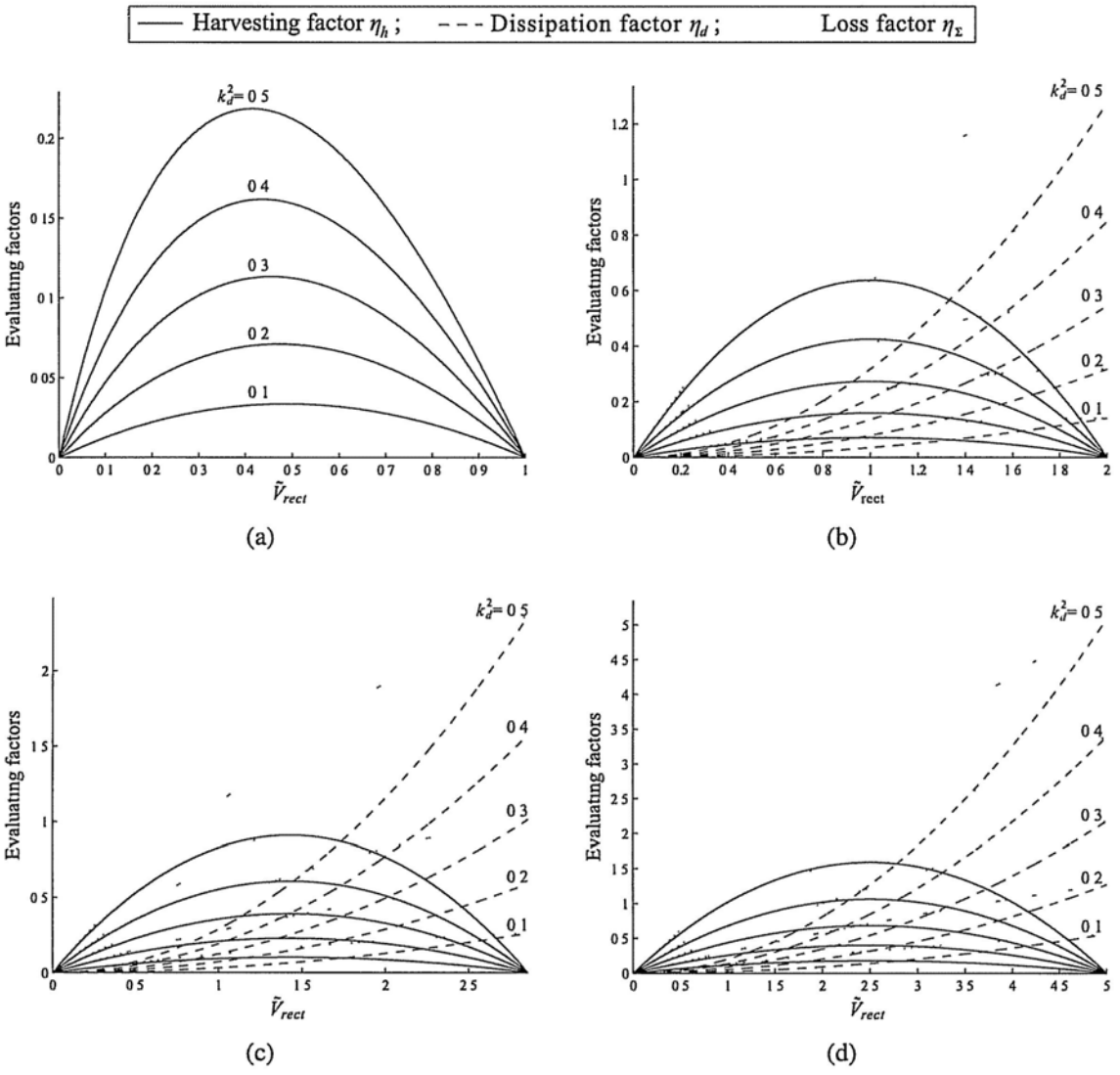

Figure 3.15: Evaluating factors, as functions of $\tilde{V}_{rect}$ and k_e^2, under different values of γ. (a) $\gamma = 1$ (SEH); (b) $\gamma = 0$ ($Q = 0$); (c) $\gamma = -0.3$ ($Q = 1.3$); (d) $\gamma = -0.6$ ($Q = 3.1$).

range as given in (3.28).

According to (3.24) $\sim$ (3.28), the harvesting factor, dissipation factor and loss factor, as functions of $\tilde{V}_{rect}$ and k_d^2, are evaluated with four different values of γ. The results of these three evaluating factors are shown in Figure 3.15. Figure 3.15(a) stands for the situation of SEH [6]. Ideally, no energy is dissipated in this situation, thus the dissipation factor equals to

[6] (3.4) $\sim$ (3.8) are used for this sub-figure.

zero; the curves of harvesting factor overlap with those of loss factor. As γ decreases, under the same k_d^2 and $\tilde{V}_{rect}$, all the three factors increase. In addition, it can also be seen from Figure 3.15 that when $\tilde{V}_{rect}$ reaches its upper limit, there is no energy harvesting effect, i.e., $\eta_h = 0$, thus all structural damping effect is due to energy dissipation. In this special case, this device becomes a *synchronized switch damping on inductor* (SSDI) device (Guyomar and Badel, 2006). This damping treatment can achieve a large loss factor, which is comparable to those of some high-polymers, e.g., for hard rubber and polystyrene, their loss factors are 1.0 and 2.0, respectively (Cremer et al., 2005).

With the purpose to optimize SSHI, considering the proportional relations between harvesting factor and dissipation factor shown in Figure 3.15, two guidelines are suggested. First, for SSHI with the same k_d^2 and γ, there are two $\tilde{V}_{rect}$ corresponding to a same harvesting factor η_h; yet, the smaller one should be the preference. Its corresponding dissipation factor is smaller, therefore, less energy is dissipated within one cycle with the same harvesting performance. The saved energy can be harvested in the future cycles. Second, for SSHI under $\tilde{V}_{rect,opt}$, even though $\eta_{h,max}$ increases against γ, it is not necessary the smaller γ, the better. Since η_d at $\tilde{V}_{rect,opt}$ also increases against γ, and its increasing rate is even larger than that of $\eta_{h,max}$. In another word, the ratio between the dissipated energy and harvested energy increases with γ. Therefore, rather than merely enhancing the harvesting capability, a more optimized SSHI should also take these into account in order to make a good balance between the coexistent energy harvesting and energy dissipation.

3.3.4 Experiments

Experiments are performed, in order to verify the theoretical analysis on energy flow in PEH with SSHI interface circuit. With the same experimental setup, but based on different processes, three experiments can be respectively performed to estimate the loss factor, harvesting factor and dissipation factor in the SSHI treatment. Figure 3.16 shows the mechanical structure and the shunt circuit in the experimental setup.

The main mechanical structure is an aluminium cantilever whose fixed end is fixed on

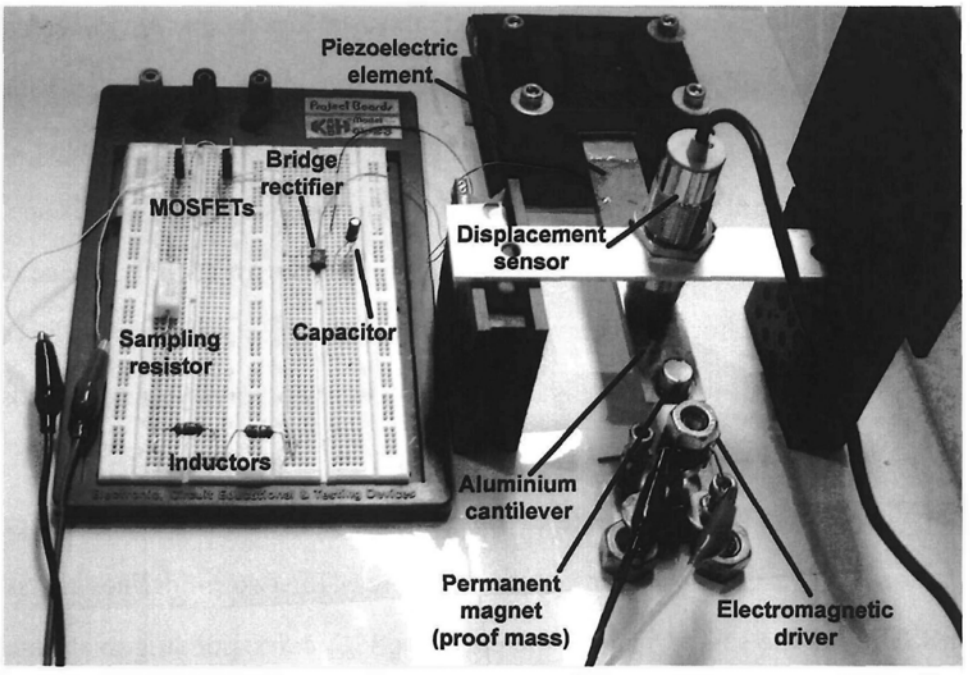

Figure 3.16: Experimental setup for PEH with SSHI technique.

the vibration-free table and the free end is driven by an electromagnetic driver. A piezoceramic patch of 49 mm $\times$ 24 mm $\times$ 0.508 mm (T120-A4E-602, Piezo System, Inc.) is bonded near the fixed end where the largest strain happens along the cantilever. A permanent magnet is attached at the free end of the cantilever, so as to achieve the coupling with the electromagnetic driver; and it also acts as a proof mass to lower the vibration frequency and increase the displacement of the free end. The displacement of the cantilever is sensed by an inductive displacement sensor (JCW-24SR, CNHF Co.). Applying a 25 Hz harmonic excitation, which corresponds to a 1.34 V peak-peak value output from the displacement sensor, to this structure, a 16.6 V peak-peak value sinusoidal voltage can be observed across the piezoelectric element.

In order to perform SSHI treatment, the displacement sensor output is connected to an A/D channel of the PC based controller board (dSPACE DS1104). The digital processer performs peak detection and generates switch driving signal accordingly to control the switch in SSHI circuit. The shunt circuit is shown on the left hand side of Figure 3.16. Table 3.2 gives the models or values of different components in the circuit.

Table 3.2: Models or values of different components in the shunt SSHI circuit

Component	Value or model
C_p	34.76 nF
sw	MOSFET (IRF530N)
L_i	121.8 mH
Bridge rectifier	DB104 (V_F = 1.0 V)
C_{rect}	9.708 μ F
r_{sample}	10.2 Ω

The coupling coefficient of the main structure k_d^2 is fixed after installation; meanwhile the Q factor of the switching shunt is fixed when all components are connected, i.e., γ is fixed. According to (3.24) $\sim$ (3.27), the three evaluating factors corresponding to structural damping, energy harvesting and energy dissipation are all functions of $\tilde{V}_{rect}$. The functional relations can be investigated experimentally as follows.

Loss factor on structural damping

As far as the loss factor is related to the system bandwidth that can be obtained from the frequency response function (FRF) [7] , the loss factors under different electrical conditions, i.e., short circuit, open circuit and seven values of $\tilde{V}_{rect}$ (from 5/12 to 35/12 with a step of 5/12), can be estimated with this method. For each condition, the peak-peak values of the displacement sensor outputs at 18 frequencies (24.0 $\sim$ 25.7 Hz with a step of 0.1 Hz) are recorded. To obtain the displacement peak-peak values under different $\tilde{V}_{rect}$, V_{rect} should be adjusted according to the changing V_{OC}, which cannot be directly measured when the SSHI treatment is operating. However, since V_{OC} is proportional to X, the maximum displacement of the structure, it can still be indirectly obtained under SSHI treatment. To adjust V_{rect},

[7] Strictly, this method for loss factor estimation is valid for linear system. However, since SSHI is a nonlinear treatment, this is only an approximation for the loss factor in SSHI treatment.

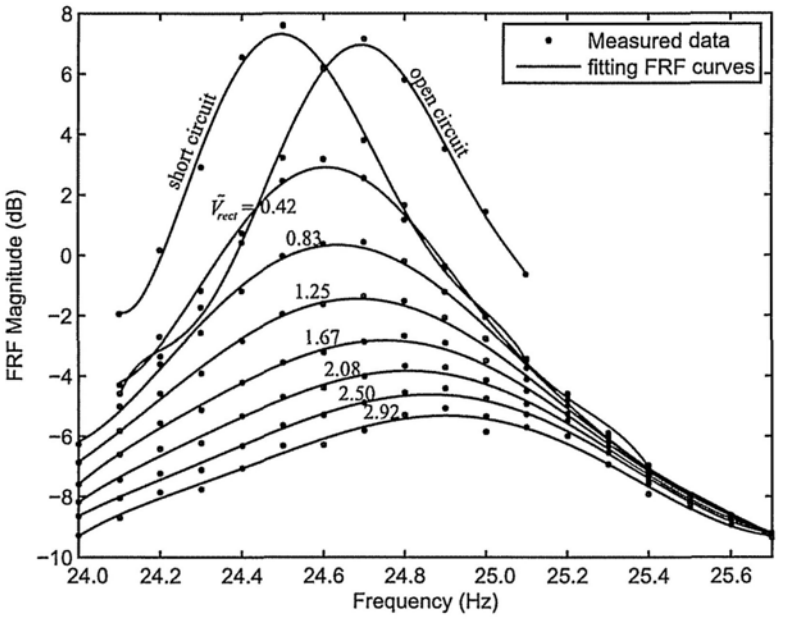

Figure 3.17: Frequency response functions under different electrical conditions.

the constant voltage output of a power supply (IPS 2303D, ISO-TECH) is connected to the capacitor C_{rect}. Nine FRF curves are obtained by fitting the corresponding data under each condition [8]. Figure 3.17 shows the measured data and fitted curves. For each curve, the resonant frequency f_0 and the -3 dB bandwidth Δf can be calculated. Therefore, the loss factor under the corresponding condition is $\Delta f / f_0$. Since the loss factors include both inherent damping and the damping contributed by SSHI, subtracting the loss factors under different $\tilde{V}_{rect}$ to that under short circuit condition yields the net contribution of the SSHI treatment (Lesieutre et al., 2004).

Harvesting factor on energy harvesting

The harvesting factor is estimated based on (3.1). With the record of a complete charging process, E_h can be obtained from the voltage history across C_{rect}, meanwhile, E_{max} can be obtained from the displacement history. This method was once used to estimate the

[8] In order to better fit the peaks, data at only 11 frequencies are used for open circuit and short circuit conditions.

harvesting factor for SEH in sub-section 3.2.4. The voltage and displacement histories are separated into a number of appropriate intervals. Within an interval, V_{rect} is regarded as the sum of V_F and the mean voltage across C_{rect}. The energy harvested during this interval can be calculated with respect to the voltage increase across C_{rect}. E_{max} here only includes mechanical vibratory energy, so it is related to the maximum displacement. Since 1.34 V peak-peak value output from the displacement sensor corresponds to 16.6 V peak-peak value sinusoidal voltage across the open circuit piezoelectric element, the mechanical vibratory energy associated with 1.34 V peak-peak value displacement output can be estimated with the device coupling coefficient, which can be calculated with (2.10). From Figure 3.17, the open circuit natural frequency $f_{OC} = 24.69$ Hz, the short circuit natural freqency $f_{SC} = 24.50$ Hz, therefore $k_d^2 = 0.0153$. This means, in the open circuit, when the voltage across C_p is at maximum, i.e., 8.3 V, the ratio between mechanical energy and electrical energy is a, which is defined above in (3.23). Knowing the E_{max} associated with 1.34 V peak-peak value displacement output, the E_{max} associated with other values can be obtained.

Dissipation factor on energy dissipation

The dissipation factor is estimated based on (3.2). From the voltage across C_p, the voltage inversion factor γ is obtained to be -0.384. So the Q factor of the switching shunt is about 1.64, the total equivalent series resistance r is 1.14 kΩ. Since a 10 Ω sampling resistor r_{sample} is connected in series to the shunt, recording the root mean square (RMS) voltage across r_{sample} under different V_{rect} with an oscilloscope (TDS 220, Tektronix), the energy consumed by r in one cycle can be estimated. As for the energy dissipated by the bridge rectifier in one cycle, i.e., the second item in (3.21), it is proportional to E_h under certain V_{rect}; therefore it can be calculated simultaneously with the estimation of E_h. Combining these two dissipations, E_d is readily to be obtained.

Results

Three experiments are performed in order to show the functional relations with either of η_h, η_d and η_Σ to $\tilde{V}_{rect}$. Besides, since k_d^2 and γ are experimentally obtained as 0.0153 and

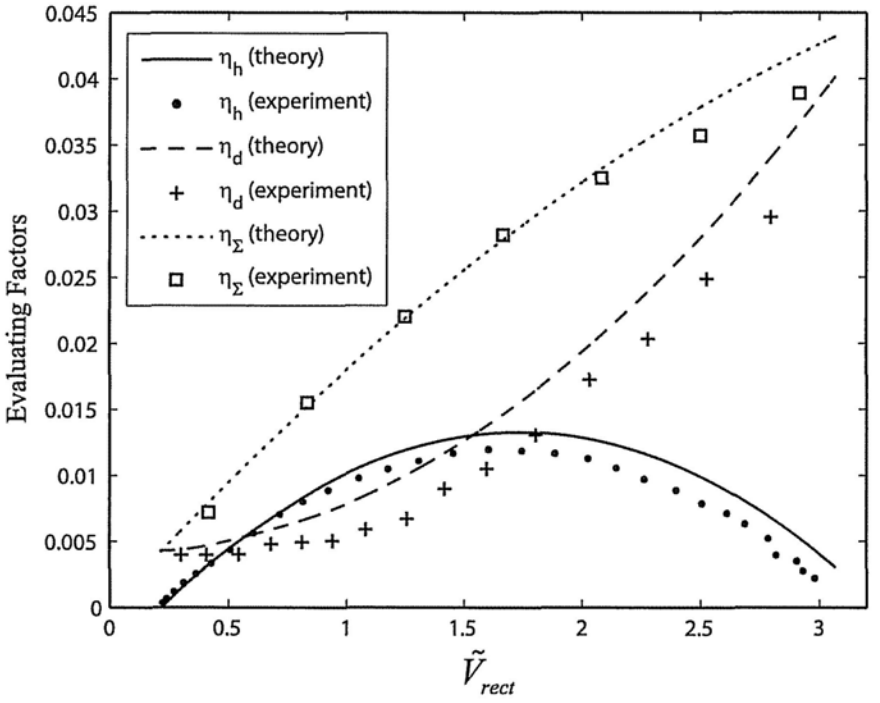

Figure 3.18: Theoretical and experimental results on three evaluating factors in PEH with SSHI interface.

-0.384, respectively, the three evaluating factors are also readily to be theoretically obtained with (3.24) $\sim$ (3.27). Both results are simultaneously shown in Figure 3.18. It demonstrates that both experimental results and theoretical analyses agree with each other very well.

3.3.5 Harvesting and damping performances

Besides clarifying the relation of energy harvesting, dissipation and damping in SSHI, we can also theoretically prove the advantages of the SSHI technique. In terms of energy harvesting capability, we can non-dimensionalize the maximum harvesting factors of SSHI to those of SEH under the same coupling coefficients, as

$$\tilde{\eta}_{h,max} = \frac{(\eta_{h,max})_{SSHI}}{(\eta_{h,max})_{SEH}} \tag{3.31}$$

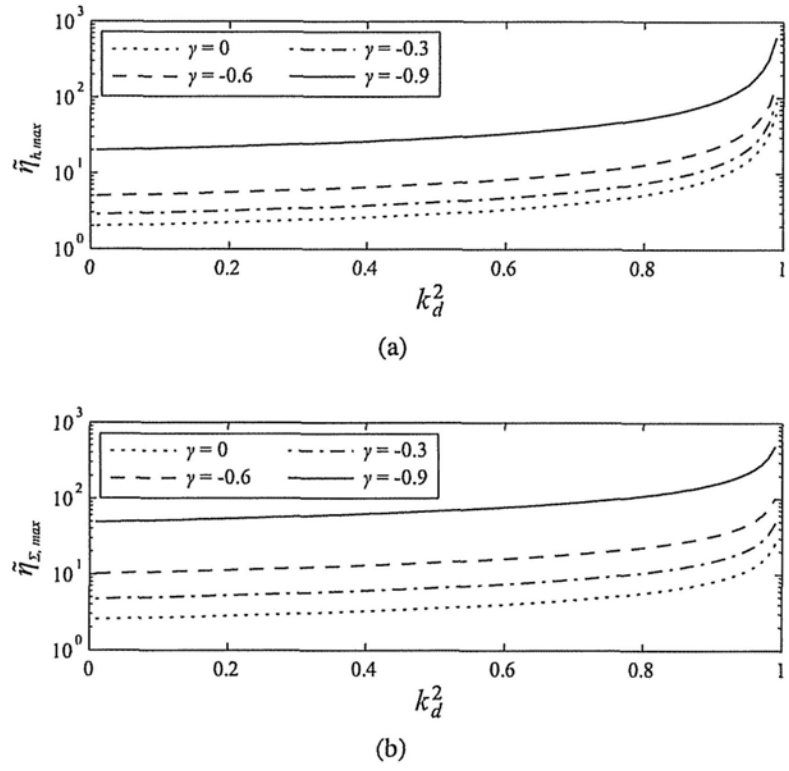

Figure 3.19: Non-dimensional maximum harvesting factors and maximum loss factors in energy harvesting with SSHI technique. (a) harvesting factor. (b) loss factor.

Figure 3.19(a) shows the non-dimensional maximum harvesting factor $\tilde{\eta}_{h,max}$ as function of k_d^2 under different values of γ. It shows that, for the purpose of harvesting energy, the harvesting capability of SSHI technique is better than that of SEH, regardless of k_d^2 and γ, since all $\tilde{\eta}_{h,max}$ in Figure 3.19(a) is larger than 1, i.e., 10^0. Moreover, more significant improvement can be achieved by introducing the SSHI treatment to the harvesting devices with higher coupling coefficient, i.e., larger k_d^2. On the other hand, with the same device using SSHI, the smaller γ, the larger improvement can be obtained.

Similarly, in terms of damping capability, we can non-dimensionalize the maximum loss factor of SSHI, which is specified as SSDI, to that of RSD under the same coupling coefficients, as

$$\tilde{\eta}_{\Sigma,max} = \frac{(\eta_{\Sigma,max})_{SSDI}}{(\eta_{\Sigma,max})_{RSD}} \tag{3.32}$$

Figure 3.19(b) shows the non-dimensional maximum loss factor $\tilde{\eta}_{\Sigma,max}$ as function of k_d^2 with respect to different values of γ. The damping capability of SSDI is better than that of RSD. The curves of $\tilde{\eta}_{\Sigma,max}$ show a similar trend as $\tilde{\eta}_{h,max}$ in Figure 3.19(a).

3.4 Summary

In this chapter, analyses were performed on the relationship among the functions of energy harvesting, energy dissipation and their effects on structural damping in piezoelectric devices. The concept of energy flow was clarified and illustrated with energy flow chart. Previously, absolute harvesting power was usually considered to evaluate different PEH devices. This is an application-oriented evaluation. But looking into the PEH devices, for an overall evaluation, it is suggested that three evaluating factors defined in (3.1) $\sim$ (3.3) are likewise important, since they are helpful to show the energy flow within different PEH devices.

Two applications of SEH and RSD utilizing piezoelectric materials were investigated, and the similarities and differences between energy harvesting and energy dissipation were discussed. These two functions could be selected to achieve different objectives. Furthermore, coexistent energy harvesting and dissipation in the implementation of energy harvesting with SSHI technique were investigated. These coexisting functions can both contribute to the effect of structural damping. The performances of the SSHI technique were also investigated. It has been shown that the SSHI would outperform the SEH in terms of harvesting capability and outperform the RSD in terms of damping capability.

On the other hand, even the SSHI treatment can significantly enhance the harvesting efficiency, it also increases energy dissipation. In particular, for larger $\tilde{V}_{rect}$, the dissipation factor can be larger than the harvesting factor, i.e., more energy is dissipated rather than harvested in one cycle. This should be avoided for the purpose of recycling the ambient vibration energy. Generally speaking, in every PEH device, energy dissipation inevitably exists. Even for SEH devices, the bridge rectifier consumes energy because of its forward voltage drop. The coexistent relation between energy harvesting and dissipation is subtle.

The understanding on their relation and their total effect to the vibrating structure is crucial towards the development on PEH devices.

□ End of chapter.

Chapter 4

Impedance based Analysis

In Chapter 3, it has been shown that the harvesting power improvement by modifying the interface circuit is significant. Yet, since the analyses were based on constant displacement excitation, like most of the electrical part emphasized studies did (Ottman et al., 2002; Qiu et al., 2009; Guan and Liao, 2007; Wu et al., 2009), the dynamics of the mechanical part was not included. On the other hand, it has been shown that the behaviors of PEH devices under displacement and force excitations are very different (Shu et al., 2007), the mechanical dynamics cannot be neglected when force excitation is applied. Besides, concerning the power optimization issue, two questions are still open for force excited PEH devices:

a) Given a force excitation applied to a specific structure, what is the maximum harvestable power?
b) Is there any interface circuit can make this maximum power?

Several literatures discussed the limitation of the harvesting power by analyzing the ideal work cycle of the electrical parts. Liu, Tian, Wang, Lin, Zhang and Hofmann (2009) proposed the so called active PEH, with which they claimed that the harvested power can be increased arbitrarily high without the limitation on power electronics efficiency. Liu, Vasic, Costa, Wu and Lee (2009) reached a similar point, but they called their method as velocity-controlled PEH. Earlier than those, Liu et al. (2007) provided a similar analysis on the ideal work cycle; but differently, they regarded the maximum parameters of a piezoelectric element, e.g., maximum strain, maximum field, maximum surface charge density and maximum stress, as the limitation of the electromechanical conversion. There are two common problems in these analyses.

a) These analyses have not considered the reaction of their treatments to the dynamics of the mechanical part (again, the mechanical dynamics was neglected). In real situation,

as the extracted energy increases, the damping effect increases too, the vibration magnitude therefore is suppressed. Eventually some of the increase on extracted energy will be canceled out.

b) It is not true that the larger the area enclosed by the work cycle, the higher the harvesting power. The enclosed area corresponds to the extracted energy in one cycle, which should be subdivided into harvested portion and dissipated portion.

The importance of detailed energy flow has been addressed in Chapter 3. Without considering the mechanical dynamics and the energy flow in the system, the discussions on the limitation of harvesting power would be misleading.

A preferred investigation on the maximum harvesting power should take both the overall dynamics and the energy flow into account. The impedance matching is well known for load power optimization. It has been employed to investigate the maximum harvesting power issue (Kim et al., 2007; Brufau-Penella and Puig-Vidal, 2009; Kong et al., 2010); nevertheless, three factors are ambiguous in their studies:

a) The definition of the equivalent impedance of a nonlinear PEH interface circuit.
b) The attainable ranges of the equivalent impedance of the electrical part under different interface circuits.
c) The objective of utilizing impedance matching in PEH.

In addition, there were also conflicts in utilizing the matching theory for power optimization in electromagnetic energy harvesting (Stephen, 2006*a*). Concerning all the above-mentioned three issues, this chapter proposes an investigation for clarification.

4.1 Impedance Modeling

Nowadays, both the modeling techniques for pure mechanical structures and pure electrical circuits are of many options. Take the PEH device shown in Figure 1.2 for example. Its mechanical part is a cantilever beam, which has multiple vibration modes. The structural

dynamics can be analyzed with either closed-form or numerical solution to the partial differential equations (PDEs). Its electrical part is a conventional rectifier circuit, which is nonlinear in nature. The circuit waveforms can be obtained with piecewise circuit equations or circuit simulation software. Yet, when the two domains are bridged by the piezoelectric transducer, the situation becomes complicated. The dynamics of the whole electromechanical device would be hardly modeled accurately with these existing methods. The characteristics of multiple vibration modes on mechanical part and nonlinearity on electrical part obstruct the integration of their models. Up to now, nearly all studies emphasizing on the mechanical part adopted simplified electrical models (Erturk and Inman, 2008*a*; Zhu et al., 2009); while studies emphasizing on the electrical part adopted simplified mechanical models (Ottman et al., 2002; Guyomar et al., 2005). The majority of researches focused on either mechanical or electrical parts, but not both.

On the other hand, energy flow and impedance matching have been considered from the system level. To utilize the impedance matching, the first problem is: what are the impedances of different parts or components in the system? The equivalent circuit of the linear mechanical part is well established. With the mechanical to electrical analogy, each mode can be equivalently represented by an RLC path in the electrical domain. The corresponding resistance, inductance, and capacitance values can be obtained by experimental identification (Guan and Liao, 2009), analytical method (Elvin and Elvin, 2009*b*), or numerical analysis (Yang and Tang, 2009). Nevertheless, for the electrical part, in most literatures, the nonlinear interface circuit was taken as an equivalent resistance, i.e., impedance without imaginary part (Kim et al., 2007; Kong et al., 2010). On the other hand, Brufau-Penella and Puig-Vidal (2009) regarded it as complex impedance. They proposed the complex conjugate impedance matching, rather than resistive impedance matching. However, they did the matching with a resistor and an inductor, whose values are able to be arbitrarily chosen, instead of considering the equivalent impedance of a real harvesting interface circuit. To determine the equivalent impedance of the electrical part is one of the keys to the analysis in this chapter.

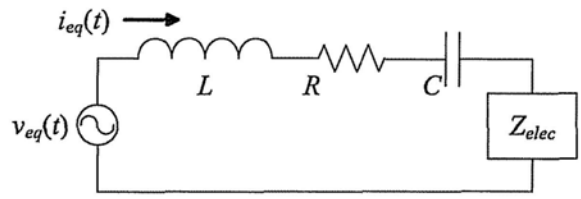

Figure 4.1: Equivalent circuit of a piezoelectric device (regarding the electrical part as a whole).

4.1.1 Impedance of mechanical part

In Chapter 2, the mechanical part in the SDOF representation of a piezoelectric device has already been modeled as equivalent impedance in the equivalent circuit, as shown in Figure 2.4. Alternatively, in some studies, the derivation is started from the following dynamic equations

$$\begin{cases} M\ddot{x}(t) + D\dot{x}(t) + (K + K_p)x(t) + \alpha_e v_p(t) = F(t) \\ i_p(t) = \alpha_e \dot{x}(t) - C_p \dot{v}_p(t) \end{cases} \tag{4.1}$$

Taking the Fourier transform of (4.1) and substituting V_{eq} and I_{eq} specified in (2.22), L, R, and C specified in (2.24) $\sim$ (2.26) into the equations, we can have

$$V_{eq}(j\omega) = \left[j\omega L + R + \frac{1}{j\omega C} + Z_{elec} \right] I_{eq}(j\omega) \tag{4.2}$$

where

$$Z_{elec} = \frac{V_p(j\omega)}{I_{eq}(j\omega)} = \frac{1}{sC_p + Y_{elec\text{-}ex}} \tag{4.3}$$

is the impedance of the electrical part. Figure 4.1 illustrates the relation given by (4.2) as equivalent circuit. The equivalent circuit is the same as that shown in Figure 2.5(a); but here the electrical part is regarded as a whole, rather than decomposed into the piezoelectric capacitance and the shunt circuit in parallel.

4.1.2 Impedance of electrical part

In sub-section 4.1.1, the electrical part of the PEH device was denoted as Z_{elec}. Yet, as we know, in circuit analysis, the concept of impedance is usually used for linear AC circuits to show the magnitude and phase relations between voltage and current. So strictly speaking, for all the AC to DC harvesting interfaces, even the simplest SEH, their behaviors cannot be completely shown by the concept of impedance. Simplification is made based on the assumption that the influence of higher-order harmonics produced by the harvesting circuit to the system is much smaller than that of the fundamental component. With this assumption, two simplified conditions are obtained.

a) The equivalent current i_{eq} can be regarded as perfect sine wave.
b) Only the fundamental component of v_p, which is denoted as $v_{p,F}$, has an effect on the dynamic of the system.

Taking SEH for instance, given the equivalent current as

$$i_{eq}(t) = I_0 \sin(\omega t) \tag{4.4}$$

where $I_0 = \alpha_e \omega X$ is the magnitude of the $i_{eq}(t)$. The voltage across the piezoelectric element can be described by the following piecewise equation:

$$v_p(t) = \begin{cases} \dfrac{I_0}{\omega C_p}[1-\cos(\omega t)] - V_{rect}, & 0 \leqslant \omega t < \theta \\ V_{rect}, & \theta \leqslant \omega t < \pi \\ V_{rect} - \dfrac{I_0}{\omega C_p}[1+\cos(\omega t)], & \pi \leqslant \omega t < \pi+\theta \\ -V_{rect}, & \pi+\theta \leqslant \omega t < 2\pi \end{cases} \tag{4.5}$$

where θ corresponds to the rectifier blocked interval in a half cycle (as illustrated in Figure 4.2(a)), V_{rect} is the rectified voltage. θ and V_{rect} are related by

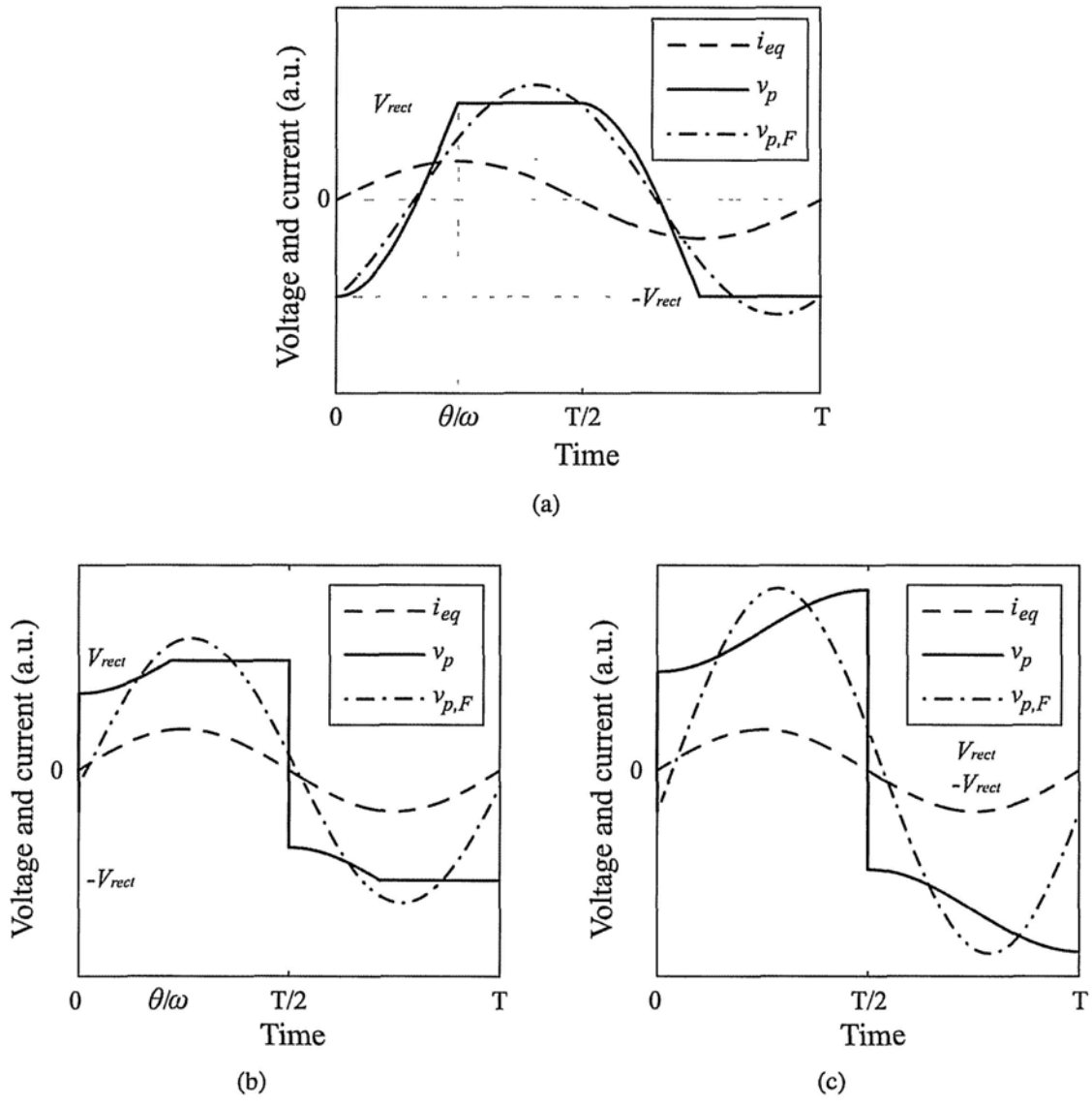

Figure 4.2: Characteristic voltage and current waveforms. (a) SEH. (b) P-SSHI. (c) S-SSHI.

$$\cos\theta = 1 - 2\tilde{V}_{rect} \tag{4.6}$$

$\tilde{V}_{rect}$ is the non-dimensional rectified voltage defined by (3.5). The rectified voltage V_{rect} is the sum of V_{store} (the voltage across C_{rect}) and V_F (the forward voltage drop of the bridge rectifier). According to (4.5), the expression on the fundamental component of v_p is obtained as

$$v_{p,F} = \frac{I_0}{2\pi\omega C_p}\left\{[\sin(2\theta) - 2\theta]\cos(\omega t) + 2\sin^2\theta\sin(\omega t)\right\} \tag{4.7}$$

Figure 4.2(a) shows the waveforms of i_{eq}, v_p, and $v_{p,F}$ under a certain V_{rect} in one vibration cycle. The equivalent impedance of the electrical part is obtained with the Fourier transform of (4.4) and (4.7)

$$Z_{elec}(j\omega) = \frac{V_{p,F}(j\omega)}{I_{eq}(j\omega)} = \frac{1}{\pi\omega C_p}\left[\sin^2\theta + j(\sin\theta\cos\theta - \theta)\right] \tag{4.8}$$

When the excitation frequency ω is fixed, Z_{elec} is independent of the voltage source, but merely depends on θ. The equivalent impedances with other harvesting interface circuits can also be obtained with this method.

The characteristic waveforms of i_{eq}, v_p, and $v_{p,F}$ in P-SSHI and S-SSHI are shown in Figure 4.2(b) and (c), respectively. From the waveform point of view, distortions are observed by taking $v_{p,F}$ as the representation of v_p, in particular, the distortions are even larger in the highly nonlinear P-SSHI and S-SSHI cases. But from the power point of view, given that i_{eq} is composed of a single harmonic and the fundamental component of $v_{p,F}$ is orthogonal to all high order harmonics, the power consumed by Z_{elec} is calculated by

$$P_{elec} = \frac{1}{T}\int_0^T v_p(t)i_{eq}(t)\mathrm{d}t = \frac{1}{T}\int_0^T v_{p,F}(t)i_{eq}(t)\mathrm{d}t \tag{4.9}$$

Therefore, representing v_p with $v_{p,F}$ is reasonable for the power estimation within the dynamic PEH systems. Similar approach called state-space averaging technique was introduced in the analyses of time-variant power conversion circuits (Sanders et al., 1991; Wong and Brown, 1995).

4.2 Range of Electrical Impedance

The ranges of the electrical equivalent impedance with four different interface circuits, i.e. SEH, RSD, P-SSHI (parallel SSHI), and S-SSHI (series SSHI), will be compared and discussed in this section. The interface circuits of SEH, RSD, P-SSHI, and S-SSHI were shown in Figure 3.2, Figure 3.3, Figure 3.11, and Figure 4.3 respectively.

In linear RSD, the electrical part is composed of C_p and R_{RSD} connected in parallel. Its impedance is

$$Z_{elec}(j\omega) = \frac{1}{\omega C_p}\left(\frac{\rho}{1+\rho^2} - j\frac{\rho^2}{1+\rho^2}\right) \tag{4.10}$$

where ρ is the non-dimensional shunt resistance in RSD defined in (3.10).

With the same method, the equivalent impedance of the electrical part in SEH, the P-SSHI and S-SSHI interfaces can also be studied. In P-SSHI, the equivalent impedance of the electrical part is obtained as

$$Z_{elec}(j\omega) = \frac{1}{\pi\omega C_p}\left[(1-\cos\theta)\left(\frac{4}{1+\gamma} - 1 + \cos\theta\right) + j\left(\frac{1}{2}\sin 2\theta - \theta\right)\right] \tag{4.11}$$

Different from SEH, in P-SSHI, θ and V_{rect} are related by

$$\cos\theta = 1 - (1+\gamma)\tilde{V}_{rect} \tag{4.12}$$

In S-SSHI, the equivalent impedance is obtained as

$$Z_{elec}(j\omega) = \frac{1}{\omega C_p}\left[\frac{4}{\pi}\frac{1-\gamma}{1+\gamma}(1-\tilde{V}_{rect}) - j\right] \tag{4.13}$$

In (4.11) $\sim$ (4.13), γ is the voltage inversion factor in every switching action, which was defined in (3.19).

According to (4.8), (4.10), (4.11), and (4.13), Figure 4.4 shows the electrical part equiv-

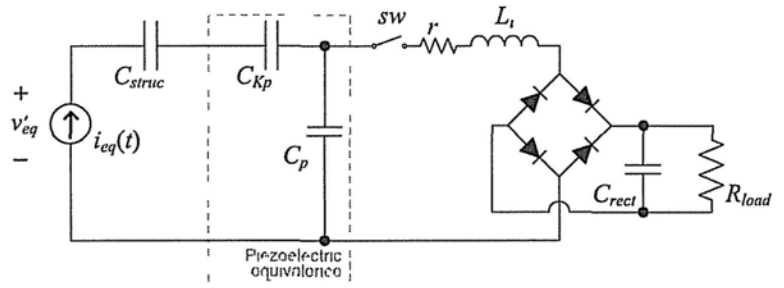

Figure 4.3: Equivalent circuit for series synchronized switching harvesting on inductor (S-SSHI).

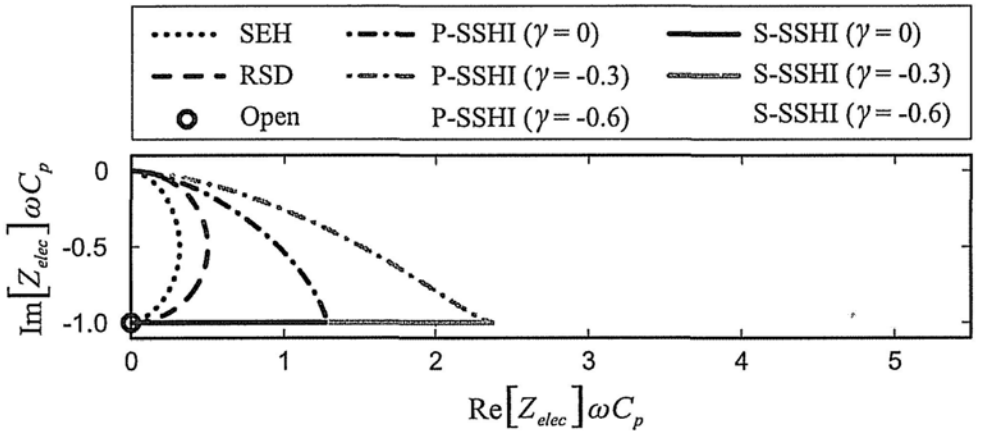

Figure 4.4: Available impedance ranges of four interface circuits.

alent impedance of the four interface circuits on the normalized complex impedance plane. Only points on the corresponding curve are attainable for a certain interface circuit. Therefore, the range is constrained, rather than able to be arbitrarily set.

Comparisons between SEH and RSD have been made in sub-section 3.2.3. It has been shown that the performances of SEH and RSD are different; the ratio between their maximum extractable powers is $2/\pi$. From Figure 4.4, the impedance ranges of SEH and RSD are not overlapped except for the points corresponding to short and open circuits; therefore, their responses to the same excitation are again shown to be different. The real component of the equivalent impedance is related to the load power. In a general matching case, it is not necessary that the larger the real component, the more power delivered. But in a low

coupling system, the equivalent source resistance, e.g., R in Figure 4.1, is much larger than the real component of Z_{elec}. In this condition, the larger the real component, the more the power delivered to the electrical part. Therefore, the maximum extractable power of RSD is larger than SEH. Both P-SSHI and S-SSHI can greatly increase the real component of the equivalent impedance (the smaller the inversion factor γ, the larger the increase on the real component); therefore, the extracted power can be increased by P-SSHI and S-SSHI.

4.3 Harvesting Power Optimization

The equivalent impedances of both the mechanical and electrical parts were obtained; further investigation on how to utilize the impedance matching to improve the harvesting power will be carried out.

4.3.1 Optimization objective

The objective of impedance matching for a general system is to maximize the power that delivered to the load. But in the energy harvesting system, the objective is vague. Various researchers have made conflicting claims (Stephen, 2006*a*). The reason is attributed to the ambiguous understanding on the concept of load in energy harvesting. In a conventional system, load consumes all the power that is extracted from the system. Whereas, in a harvesting system, the concern is how much energy is scavenged rather than consumed. The harvested energy is only one portion of the extracted energy. Clarification on energy flow is crucial towards straightening out the objective of impedance matching in energy harvesting.

With the energy flow chart given in Figure 3.1 and the analyses on the energy flow among three different piezoelectric devices presented in Chapter 3, it was clarified that the functions of energy harvesting and energy dissipation are coexistent in a harvesting interface circuit. Both of them bring out structural damping. Recall that there are generally three possible destinations for electrical energy:

a) Being converted into thermal energy (branch **G** in Figure 3.1), i.e. electrically dissi-

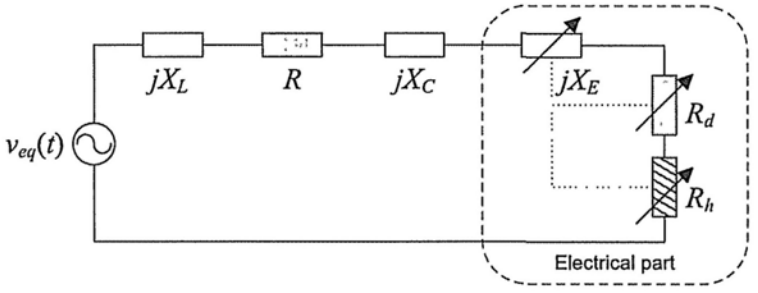

Figure 4.5: Equivalent impedance network of a force excited PEH device.

pated;

b) Being stored as energy storage (branch **I**), i.e. electrically harvested;

c) Returning to the mechanical part as a portion of the vibratory energy (branch **J**).

While taking the electrical part as equivalent impedance, its real component always absorbs energy without any return; on the other hand, its imaginary component alternately absorbs energy from the system and then all returns. Comparing the above-mentioned three items and the two components of the equivalent impedance of the electrical part, item c) is corresponding to the imaginary component; while the total effect of items a) and b) contributes to the real component. But among these three items, only the second one, i.e., the harvesting power, is the target for the purpose of energy harvesting. In order to identify this target, the real component of the equivalent impedance Z_{elec} should be further subdivided into two. One is the dissipative component R_d, while the other is the harvesting component R_h, as shown in Figure 4.5. In the equivalent impedance network of Figure 4.5, X_L, X_C, and X_E are the reactance of L, C, and the electrical part, respectively. From the viewpoint of the excitation source, R_d and R_h have the same effect of absorbing energy from the source; whereas, their functions are different in nature. In Figure 4.5, different pattern is used for R_h for distinction. As illustrated in Figure 4.4, the impedance of a certain interface circuit is adjustable, but unable to be arbitrarily set. The values of R_d, R_h and X_E are not only variables (denoted with arrows), but also related with each other (illustrated with dot links among the three components).

The dissipative component R_d in the SEH interface is attributed to the forward voltage drop of the rectifier V_F. In the SEH

$$R_d = \frac{4}{\pi\omega C_p}\tilde{V}_F(1-\tilde{V}_{rect}) \tag{4.14}$$

$$R_h = \frac{4}{\pi\omega C_p}(\tilde{V}_{rect}-\tilde{V}_F)(1-\tilde{V}_{rect}) \tag{4.15}$$

$$X_E = \frac{1}{\pi\omega C_p}(\sin\theta\cos\theta-\theta) \tag{4.16}$$

where $\tilde{V}_F$ is the non-dimensional forward voltage drop, which is defined in (3.26). For the P-SSHI and S-SSHI, the dissipative component R_d is composed of the rectifier dissipation and the dissipation produced during the switching actions. In the P-SSHI

$$R_d = \frac{1}{\pi\omega C_p}\left\{2\tilde{V}_F\left[2-\tilde{V}_{rect}(1+\gamma)\right]+\tilde{V}_{rect}^2(1-\gamma^2)\right\} \tag{4.17}$$

$$R_h = \frac{2}{\pi\omega C_p}(\tilde{V}_{rect}-\tilde{V}_F)\left[2-\tilde{V}_{rect}(1+\gamma)\right] \tag{4.18}$$

$$X_E = \frac{1}{\pi\omega C_p}\left(\frac{1}{2}\sin 2\theta-\theta\right) \tag{4.19}$$

In the S-SSHI

$$R_d = \frac{4}{\pi\omega C_p}\frac{1-\gamma}{1+\gamma}(1-\tilde{V}_{rect}+\tilde{V}_F)(1-\tilde{V}_{rect}) \tag{4.20}$$

$$R_h = \frac{4}{\pi\omega C_p}\frac{1-\gamma}{1+\gamma}(\tilde{V}_{rect}-\tilde{V}_F)(1-\tilde{V}_{rect}) \tag{4.21}$$

$$X_E = -\frac{1}{\omega C_p} \tag{4.22}$$

4.3.2 Constrained impedance matching

Based on the energy flow in a PEH system, the harvesting power is obtained as

$$P_h = \frac{V_{eq}^2 R_h}{2\left|Z_{sys}\right|^2} = \frac{V_{eq}^2}{2}\frac{R_h}{(X_L+X_C+X_E)^2+(R+R_d+R_h)^2} \tag{4.23}$$

where V_{eq} is the magnitude of the equivalent voltage source, which is constant for the force excited case; Z_{sys} denotes the total input impedance of the system, from the view of v_{eq}.

For a general case of impedance matching, the maximum P_h can be achieved under the condition that

$$R_h = \sqrt{(X_L+X_C+X_E)^2+(R+R_d)^2} = \left|Z_{sys}-R_h\right| \tag{4.24}$$

However, for a practical harvesting device, the condition provided by (4.24) is hardly satisfied. Due to the low coupling coefficient, the magnitudes of X_L, X_C, and R are usually much larger than that of Z_{elec}. Even some advanced interface circuits, e.g., P-SSHI and S-SSHI, can enlarge the magnitude of Z_{elec}; its magnitude is still limited, and the range of Z_{elec} is constrained on the corresponding curve. On the other hand, this result was obtained under the condition that the load impedance is independent to the source impedance. However, in this case, R_h is related with R_d and X_E; the result in general impedance matching cannot be simply applied to the PEH cases.

Therefore, in harvesting power optimization, a constrained matching, instead of free matching, should be used. Since P_h is a function of ω and $\tilde{V}_{rect}$, When the excitation frequency ω is determined, maximum P_h is obtained at the zero derivative point, i.e.,

$$\begin{aligned}\frac{\partial(2P_h/V_{eq}^2)}{\partial\tilde{V}_{rect}} &= \left[(X_L+X_C+X_E)^2+(R+R_d)^2-R_h^2\right]\frac{\partial R_h}{\partial\tilde{V}_{rect}} \\ &\quad -2R_h(R+R_d+R_h)\frac{\partial R_d}{\partial\tilde{V}_{rect}} \\ &\quad -2R_h(X_L+X_C+X_E)\frac{\partial X_E}{\partial\tilde{V}_{rect}} \\ &= 0\end{aligned} \tag{4.25}$$

Theoretically, optimum $\tilde{V}_{rect}$ is obtainable by substituting the expressions on R_h, R_d, and X_E into (4.25), then solving the equation. Closed form expressions on optimum $\tilde{V}_{rect}$ are preferred; however, the transcendental equation is unable to be solved with analytical method. It is solvable with numerical method; it seems more convenient to obtain the optimum by substituting the expressions of R_h, R_d, and X_E into (4.23) and numerically searching for the maximum P_h.

The ratio between R_h and $\left|Z_{sys}-R_h\right|$ is defined as the matching index

$$\lambda = \frac{R_h}{\sqrt{(X_L+X_C+X_E)^2+(R+R_d)^2}} \tag{4.26}$$

At the free matching point, which was given by (4.24), λ equals to one. Taking the analogy to the conventional impedance matching case, λ represents the relation between the "load impedance" and the "source impedance". But different from the conventional case, it is not necessary the closer between λ and one, the more energy can be delivered to the "load". Because in conventional case, the source impedance is fixed; yet, in (4.26), both R_h and $\left|Z_{sys}-R_h\right|$ are changeable. Therefore, λ can be only used to show the relation between the "load" and "source" here. In low coupling PEH device, R_h is usually much smaller than $\left|Z_{sys}-R_h\right|$; therefore, $\lambda \ll 1$.

In this PEH study, P_h is the most direct index for harvesting power optimization. It can be expressed as functions of some tunable parameters in a harvesting interface circuit. In all the three interfaces of SEH, P-SSHI, and S-SSHI, the tunable ranges are limited (only one tunable parameter). The non-dimensional rectified voltage $\tilde{V}_{rect}$ is the most representative

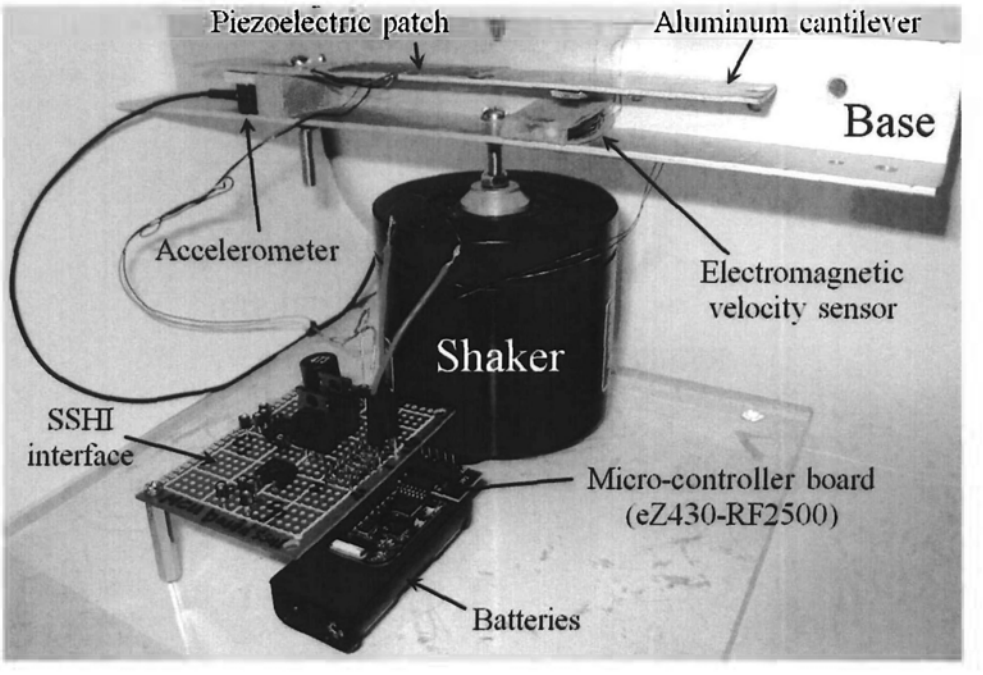

Figure 4.6: Experimental setup of a base excited PEH device.

tunable parameter within these three interface circuits.

4.4 Experiments

Because the base excitation PEH devices can be modeled as the force excitation ones with the equivalent force of

$$F(t) = -M\ddot{y}(t) \tag{4.27}$$

where $\ddot{y}(t)$ represents the base acceleration [1], experiments are carried out with a base excited piezoelectric energy harvester for three cases. In each case, one of the interface circuits among SEH, P-SSHI, and S-SSHI is connected to the piezoelectric cantilever. The harvesting power is theoretically obtained as functions of $\bar{V}_{rect}$. The actual harvesting power is experimentally measured for comparison.

[1] Detailed explanation will be provided in Chapter 5.

Table 4.1: Parameters of the experimental setup.

Component	Value or model
α_e	4.75×10^{-4} NV
f_0	42.76 Hz
sw	MOSFET (IRL510)
Rectifier	DB104 (V_F=1.0 V)
γ	-0.7
L_i	47 mH
C_{rect}	1, 10, 22 μF
C_p	34.69 nF
L	31 kH
C	448 pF
R	1 MΩ

4.4.1 Experimental setup

Figure 4.6 shows the experimental setup. The main mechanical structure is an aluminum cantilever, whose excitation is from a shaker (4810, B & K). A piezoceramic patch of 49 mm $\times$ 24 mm $\times$ 0.508 mm (T120-A4E-602, Piezo System, Inc.) is bonded near the fixed end. An accelerometer (4501, B & K) is installed at the fixed end to track the base acceleration. For the purpose of synchronization in both P-SSHI and S-SSHI, an electromagnetic sensor is employed to sense the relative velocity between the cantilever beam and the base. The permanent magnet acts as proof mass at the same time. It can lower the vibration frequency and increase the displacement of the free end. The output voltage from the coil, which is proportional to the end velocity, is then input to a micro-controller unit (eZ430-RF2500, Texas Instrument). In the circuitry part, the micro-controller is coded to firstly analyze the velocity signal, and then generate switching command to drive the MOSFET switch to perform synchronized switching actions. Although the micro-controller is powered by

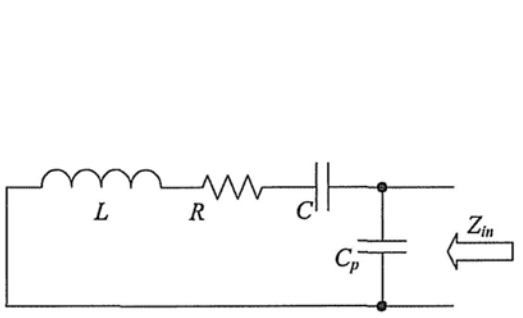

(a)

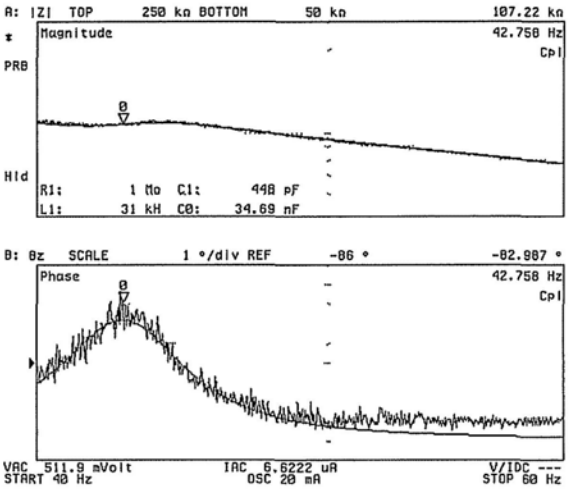

(b)

Figure 4.7: The internal impedance of the piezoelectric structure. (a) Van Dyke's model. (b) Measured and fitted results.

batteries, there are two advantages for this setup, compared to those which were commonly used in the previous studies (Guyomar et al., 2005; Lefeuvre, Badel, Richard, Petit and Guyomar, 2006). By adopting the electromagnetic velocity sensor, rather than inductive displacement sensor, self-powered sensing is achieved. Meanwhile, since the velocity signal is obtained directly, zero-crossing detection rather than peak detection is required, which might help to save some computational effort. By equipping a micro-controller unit, which works independently and provides accesses to many peripheral devices, e.g., sensors, RF unit, and power management unit, we are getting closer towards the goal of constructing an intelligent autonomous device.

Table 4.1 gives the parameters of the experimental setup, including mechanical structure and interface circuit. The equivalent impedance of the mechanical part is obtained with experimental identification. Without excitation applied and shunt circuit connected, the internal impedance of the piezoelectric structure can be derived from Figure 2.5(a). It was also known as the Van Dyke's model (Guan and Liao, 2009), as shown in Figure 4.7(a). The measured result of the internal impedance is obtained with an impedance analyzer (4294A, Agilent), and it is shown in Figure 4.7(b). Based on the Van Dyke's model, the component

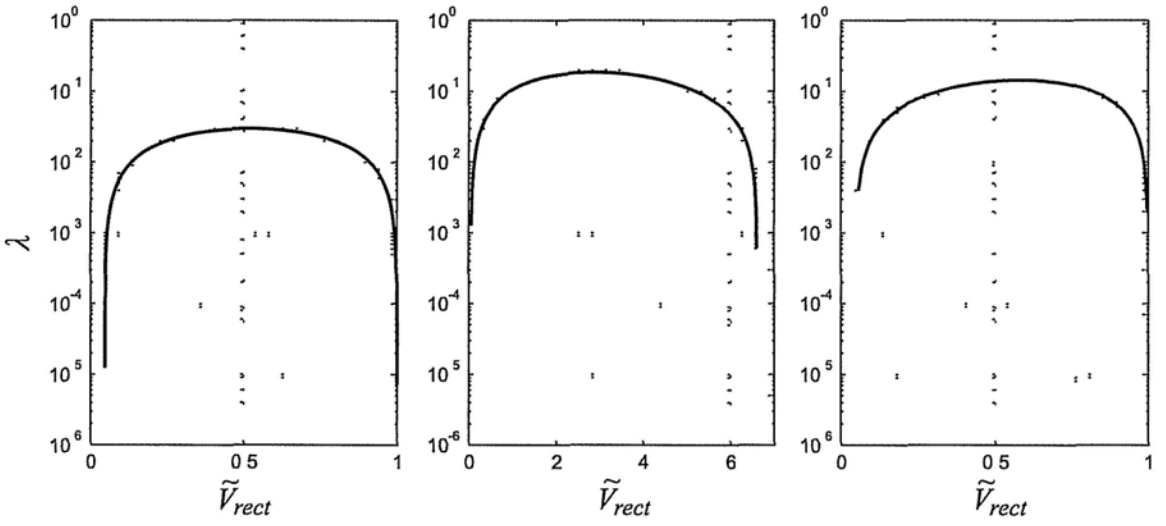

(a) (b) (c)

Figure 4.8: The matching indices with different interface circuits. (a) SEH. (b) P-SSHI. (c) S-SSHI.

values are obtained by fitting the experimental waveforms. The values are also listed in Table 4.1.

4.4.2 Results

Given a 42 Hz and 10 m/s^2 (in RMS) harmonic base excitation, the harvesting power under different $\tilde{V}_{rect}$ is studied both theoretically and experimentally. The matching indices under the three circuits of SEH, P-SSHI, and S-SSHI are firstly checked. The theoretical results on λ are shown in Figure 4.8. It is shown that, the index λ is always smaller than one, i.e., the value of R_h is not comparable to the magnitude of the sum of the rest impedance. Among the three circuits, the P-SSHI case is the closest to one, but its maximum λ is only around 0.2. Moreover, even λ is able to attain one, maximum harvesting power still cannot be ensured. P_h is the most direct index to maximize the harvesting power.

Experiments are carried out to obtain the P_h under different $\tilde{V}_{rect}$. In experiments, different DC load resistors R_{load} are connected one after another to stabilize the V_{store} at different levels. The corresponding experimental P_h is obtained with

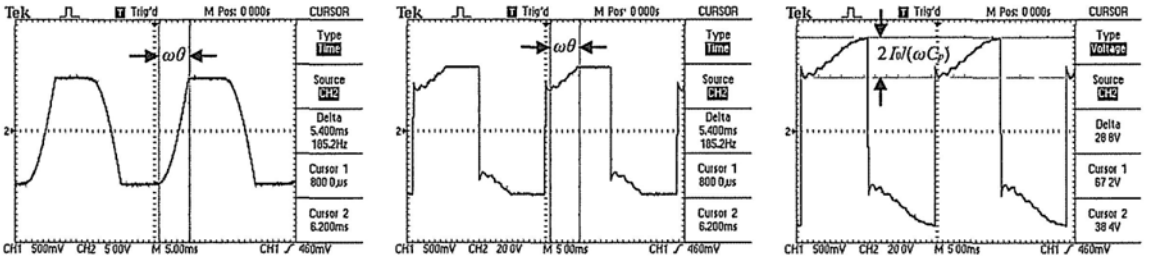

(a) (b) (c)

Figure 4.9: Measured waveforms. (a) SEH. (b) P-SSHI. (c) S-SSHI.

$$P_{h,exp} = \frac{V_{store}^2}{R_{load}} \tag{4.28}$$

For the measurement of $\tilde{V}_{rect}$, V_{rect} is the sum of V_{store} and V_F (1.0 V for the bridge rectifier we used), but I_0 changes under different V_{rect}. It is better to take the time interval $\omega\theta$ as the direct measured parameter in SEH and P-SSHI, as illustrated by Figure 4.9(a) and (b) [2], and then obtained $\tilde{V}_{rect}$ with (4.6) and (4.12), respectively. And for S-SSHI, there is no conduction angle θ, but $2I_0/(\omega C_p)$ can be directly measured from the waveform, as illustrated by Figure 4.9(c) [3].

The theoretical and experimental results on the harvesting power are shown in Figure 4.10 for comparison. The theoretical results match the experimental data very well. The P-SSHI provides the maximum harvestable power among the three cases. For this specific based excited PEH device, the improvement of implementing P-SSHI and S-SSHI, compared to SEH, is about 500% and 400%, respectively. The improvement in implementing these two interfaces, yet, might be different between two different devices, since it also depends on the mechanical characteristics. Moreover, the difference between the impedance matching in PEH and the conventional free matching with constant source impedance should

[2] In P-SSHI, as far as there is usually a reversion after every voltage inversion, $\omega\theta$ should be the time interval started at the lowest point after the reversion and ended when the bridge rectifier is conducted.

[3] In S-SSHI, also because of the reversion after every voltage inversion, $2I_0/(\omega C_p)$ should be the voltage difference between the lowest point after the reversion and the highest point before another switching action.

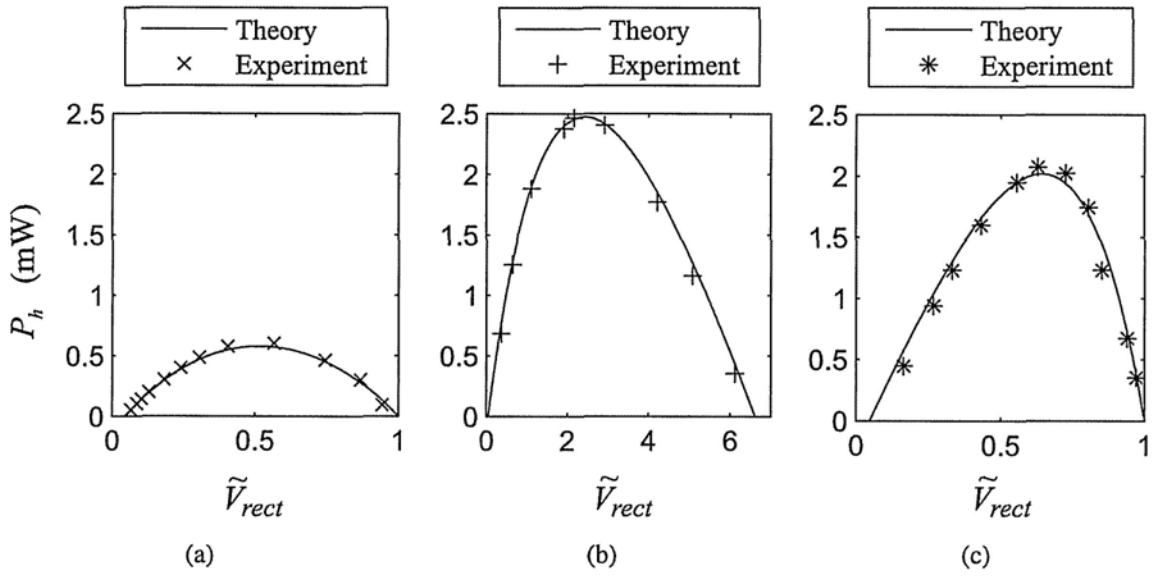

Figure 4.10: Theoretical and experimental results on the harvesting power with different interface circuits. (a) SEH. (b) P-SSHI. (c) S-SSHI.

be addressed.

Previous studies on P-SSHI and S-SSHI were mostly conducted under constant displacement excitation (Badel et al., 2006; Lallart and Guyomar, 2008). Under constant displacement excitation, the P_h curve is symmetric with the middle value in the $\tilde{V}_{rect}$ range for all the SEH, P-SSHI, and S-SSHI (Badel et al., 2006). Yet, from Figure 4.10, the shapes are asymmetric, in particular, for P-SSHI and S-SSHI. The SEH curve seems still symmetric. The reason is that, its Z_{elec} is far from the equivalent impedance of the mechanical part in this device; therefore, harvesting with this interface circuit makes little influence on the system dynamics. The displacement of this device changes little with the SEH interface circuit.

4.5 Discussions

Power optimization under force excitation

Power optimization has been investigated in some of the previous literatures. However, as reviewed in Section 1.3, in the theoretical analysis of PEH devices, when one of the

mechanical or electrical parts was emphasized, the other was usually oversimplified. For the analyses with advanced mechanical models, e.g., analytical solution to PDEs, real harvesting circuits were seldom taken into consideration; on the other hand, analyses on advanced harvesting interface circuits have difficulties on the synthesis of the mechanical dynamics and the nonlinear circuit behavior. Even some syntheses were claimed in literatures, all their mechanical models were based on SDOF approximation.

Guyomar et al. (2005) suggested a power optimization approach for SSHI interface circuits under force excitation, but in fact, it was still optimization under displacement excitation. The force magnitude is only used to determine the displacement level at the presumed "optimum point", where the excitation force and vibration speed are in phase. Shu et al. (2007) pointed out the insufficiency of the in-phase analysis and also provided an improved analysis on SSHI. In their study, it was found that no matter the real electromechanical system is weakly or strongly coupled, the electrical response using an ideal SSHI interface is similar to that using the SEH interface in a strongly coupled electromechanical system operated at the short circuit resonance. The impedance based analysis presented in this chapter further perfected Shu et al. (2007)'s finding. Utilizing the impedance concept makes this study more compatible with the existing power system analysis. In addition, based on the comprehensive understanding on the energy flow, some previous neglected details on the roles of energy harvesting and dissipation were also considered in this analysis.

It has been both theoretically and experimentally shown that the SSHI interface circuits can harvest several hundred percents more power than the SEH one under the same force excitation and with the same piezoelectric structure. However, the question at the beginning of this chapter was still unanswered, i.e., what is the maximum harvestable power? Even the power optimization for PEH devices is very different from general impedance matching procedure, this task can be roughly broken down into two steps

a) To maximize the power extraction, i.e., the sum of harvesting and electrical dissipation
b) To increase the portion of the harvested power within the extracted power

To simplify the problem, let us consider the harvesting power and electrical extracted

power under resonance. At resonance, the sum of the imaginary components in the equivalent impedance network is zero, i.e., $X_L + X_C + X_E = 0$. Substituting this relation as well as (2.22) and (2.25) into (4.23) gives the harvesting power under resonance

$$P_{h,r} = \frac{F_0^2}{2} \frac{\alpha_e^2 R_h}{[D + \alpha_e^2 (R_d + R_h)]^2} \tag{4.29}$$

where F_0 is the magnitude of the applied harmonic force. Since the harvesting power is a portion of the extracted power

$$P_{h,r} = \frac{R_h}{R_d + R_h} P_{\Sigma,r} \tag{4.30}$$

The electrical power extraction is expressed as

$$P_{\Sigma,r} = \frac{F_0^2}{2} \frac{\alpha_e^2 (R_d + R_h)}{[D + \alpha_e^2 (R_d + R_h)]^2} \tag{4.31}$$

Unlike the optimization of harvesting power, in which both the load and source impedance are variables, the optimization of extracted power is the same as general impedance matching. Maximum energy is extracted from the system when $R_d + R_h = D/\alpha_e^2 = R$. Since $R_d > 0$, we can have the following relations on the harvesting and extracted powers

$$P_{h,r} < P_{\Sigma,r} \leqslant \frac{F_0^2}{8D} \tag{4.32}$$

In the previous literatures, the harvesting power was considered as function of k_d^2/ζ_M (Shu et al., 2007) or similarly $k_d^2 Q_M$ (Guyomar et al., 2009), where

$$Q_M = \frac{\sqrt{M(K + K^D)}}{D} \tag{4.33}$$

$$\zeta_M = \frac{D}{2\sqrt{M(K+K^D)}} \tag{4.34}$$

are the quality factor and damping ratio of the mechanical system at open-circuit condition. With (2.11) and (2.12), the device coupling coefficient can also be expressed as

$$k_d^2 = \frac{\alpha_e^2}{(K+K^D)C_p} \tag{4.35}$$

In addition, the open-circuit natural frequency is given by

$$\omega^D = \sqrt{\frac{K+K^D}{M}} \tag{4.36}$$

Combining (4.33), (4.35) and (4.36), we can have

$$k_d^2 Q_M = \frac{\alpha_e^2}{\omega^D C_p D} \tag{4.37}$$

Assuming that the resonant frequency after connecting the harvesting interface circuit is very close to that at open circuit condition, (4.29) and (4.31) are also expressed as

$$P_{h,r} = \frac{F_0^2}{2} \frac{k_d^2 Q_M \bar{R}_h}{D\left[1+k_d^2 Q_M(\bar{R}_d+\bar{R}_h)\right]^2} \tag{4.38}$$

$$P_{\Sigma,r} = \frac{F_0^2}{2} \frac{k_d^2 Q_M (\bar{R}_d+\bar{R}_h)}{D\left[1+k_d^2 Q_M(\bar{R}_d+\bar{R}_h)\right]^2} \tag{4.39}$$

where

$$\bar{R}_h = \omega C_p R_h \tag{4.40}$$

$$\bar{R}_d = \omega C_p R_d \tag{4.41}$$

are the non-dimensional harvesting and dissipative components of the selected circuit. So with the impedance based analysis, the effects of different interface circuits are reflected by $\bar{R}_h$ and $\bar{R}_d$, which only depend on the characteristic of the selected circuit as well as its rectified voltage.

Shu et al. (2007) found that the electrical response using an ideal SSHI interface, no matter under weakly or strongly coupled condition, is similar to that using the SEH interface in a strongly coupled electromechanical system. This description can also be explained with (4.38) and (4.39). As we can observe from (4.39), both the increases on $k_d^2 Q_M$ and $\bar{R}_d + \bar{R}_h$ result in the increase of their product, and thus have the same effect towards the power extraction $P_{\Sigma,r}$. Therefore, given that the adoption of SSHI interface can make $\bar{R}_d$ and $\bar{R}_h$ much larger than those in SEH, it is rational that the PEH system with SSHI interface performs like strongly coupled PEH system with SEH interface. For the harvesting power, it can be observed from (4.38) that $\bar{R}_d$ and $\bar{R}_h$ have different effects on $P_{h,r}$. Therefore, the distinction on the their effects as well as the understanding on their applicable ranges for different interface circuits are important towards the optimization of harvesting power.

Design consideration in practical systems

Equations (4.29) $\sim$ (4.32) provide ideas on the relation between the extracted and harvesting power in a general case without considering the constraints on α_e^2, R_d and R_h. In the power optimization of practical systems, the constraints on these parameters need to be taken into account.

Figure 4.11 shows the equivalent impedance of both mechanical and electrical parts in the experiments introduced in Section 4.4. Their real components correspond to R and $R_d + R_h$, respectively. It can be observed that both the P-SSHI and S-SSHI can greatly extend the the real component of Z_{elec}, compared to RSD and SEH. However, in this case, the $R_d + R_h$ still cannot catch up with R. The ratio between $R_d + R_h$ and R can be increased by three means:

a) implement more sophisticated circuit, so as to increase $R_h + R_d$, e.g., replace SEH

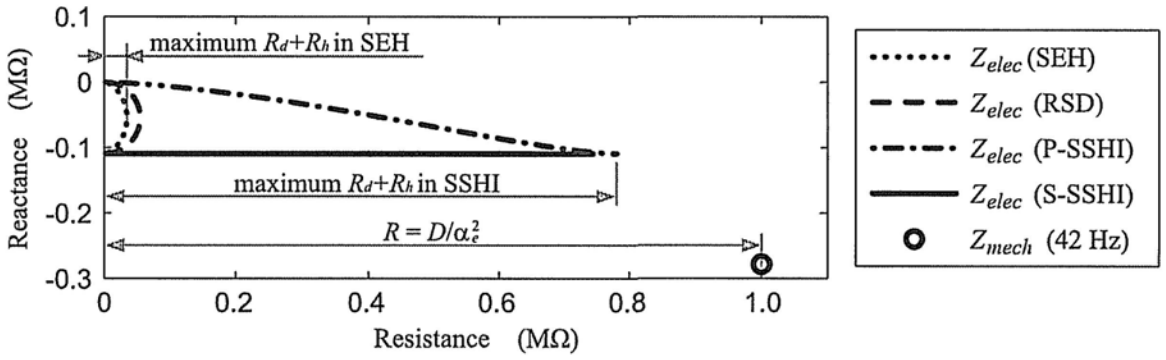

Figure 4.11: Mechanical and electrical impedances in the experiments.

with P-SSHI or S-SSHI; or decrease the voltage inversion factor γ in SSHI circuits;

b) decrease the inherent mechanical damping D;

c) increase the force-voltage factor α_e.

These three means imply that all the mechanical structure, transducer, and electrical circuit can contribute to the increase of power extraction.

The second step is to increase the ratio between harvesting and dissipation power. The relation between harvesting and dissipation in P-SSHI has been investigated in Section 3.3. Sometimes the harvesting power is larger, while sometimes the dissipation one is larger. Their sum, i.e., the extracted power, is not constant. The above-mentioned two steps are dependent, rather than can be separately carried out. Besides, maximum harvesting power is not necessarily attained at resonance.

In general, the harvesting power might be further improved by increasing $R_h + R_d$, decreasing D, increasing α_e, and adjusting the ratio between R_h and R_d. There is no explicit formula for these constrained impedance matching problems. Optimization can be carried out with numerical method by taking P_h in (4.23) as the direct objective index.

On power and efficiency optimization

Power and efficiency were usually taken as the objects for the optimization of PEH devices. But their differences were seldom discussed. One widely referred explicit expression

on optimum conversion efficiency was proposed by Richards et al. (2004). They assumed that the maximum efficiency is obtained at the maximum power point, which is appropriate for the weakly coupled system, but would be misleading for the strongly coupled system (Shu and Lien, 2006*b*).

This can also be explained from the impedance point of view. Under the resonance, the harvesting power is given by (4.29) and (4.38); the harvesting efficiency is expressed as

$$\eta_{eff,r} = \frac{\alpha_e^2 R_h}{D + \alpha_e^2 (R_d + R_h)} = \frac{k_d^2 Q_M \bar{R}_h}{1 + k_d^2 Q_M (\bar{R}_h + \bar{R}_d)} \tag{4.42}$$

In the weakly coupled system, $k_d^2 Q_M \ll 1$; therefore

$$P_{h,r} \approx \frac{F_0^2}{2} \frac{k_d^2 Q_M \bar{R}_h}{D} \tag{4.43}$$

$$\eta_{eff,r} \approx k_d^2 Q_M \bar{R}_h \tag{4.44}$$

The increase on the harvesting efficiency is associated with the increase on the harvesting power. Both of them are related to $\bar{R}_h$ rather than $\bar{R}_d$. In the strongly coupled case, $k_d^2 Q_M \gg 1$; therefore we can have

$$P_{h,r} \approx \frac{F_0^2}{2} \frac{\omega C_p}{\alpha_e^2} \frac{\bar{R}_h}{(\bar{R}_h + \bar{R}_d)^2} \tag{4.45}$$

$$\eta_{eff,r} \approx \frac{\bar{R}_h}{\bar{R}_h + \bar{R}_d} \tag{4.46}$$

The relation between (4.45) and (4.46) is similar to that between power and efficiency in an ordinary resistive impedance network, in which $\bar{R}_h$ is the "load resistance", while $\bar{R}_d$ is the "source resistance". As illustrated in Figure 4.12, it can be seen that the efficiency and load power are functions of the ratio between load and source resistance. The efficiency monotonically increases with the ratio; the power increases with the ratio until $R_{load} =$

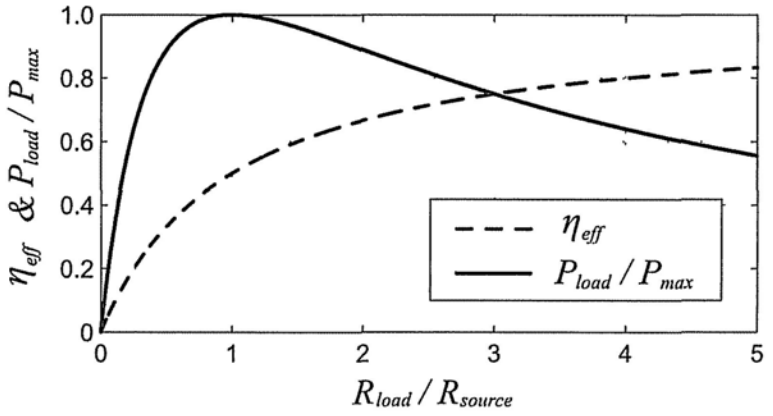

Figure 4.12: Efficiency and load power in an ordinary resistive impedance network.

R_{source}, and then decreases. Therefore, the assumption that the increase on efficiency is associated with the increase on transfer power is not valid for the strongly coupled system.

Both of the harvesting power and efficiency of PEH devices under harmonic excitation were discussed above. In these systems, the input power is continuous; the amount of potential harvestable energy is infinite. Therefore, the harvesting power seems more suitable to be the object for optimization. Increasing the harvesting power enables the device to accumulate more energy in the same time interval, or undertake heavier duties. The harvesting efficiency is more sensitive for PEH devices under pulsed or impact excitation. Under these excitations, the energy input is limited. Most of the time, it is desired to scavenge the energy as much as possible, even spending longer time to do so. If the energy is not scavenged with high efficiency, it will turn into never reclaimable heat.

4.6 Summary

The impedance matching theory is useful in load power optimization. Yet, for the research on piezoelectric energy harvesting (PEH), several issues should be addressed before utilizing impedance matching for harvesting power optimization. The methodologies to obtain the equivalent impedances of the mechanical and electrical parts were proposed. Only when both sides are uniformly modeled in terms of impedances, the utilization of the impedance

method to study the dynamics of an entire PEH system can be realized. Moreover, we studied the constraints on the equivalent impedances of the electrical part connected with three different interface circuits, including standard energy harvesting (SEH), parallel synchronized switching harvesting on inductor (P-SSHI), and series synchronized switching harvesting on inductor (S-SSHI). Since there is only one tunable parameter in either of these interface circuits, the range of the electrical equivalent impedance is constrained on a specific curve, rather than able to be arbitrarily set, as claimed in some literatures.

The objective of impedance matching was clarified considering the energy flow within a PEH system. This understanding is also valuable for the harvesting power optimization in other energy harvesting technologies. For harvesting power optimization, it has been shown that its procedures are different from the general impedance matching approaches. In these PEH cases, both the load and source impedances are dependent variables. Moreover, their values are constrained, rather than can be arbitrarily set. Taking these into consideration, the power optimization was carried out with numerical method in our analysis. Experiments showed that the impedance based analysis can model the dynamics of a base excited PEH system around the first vibration mode and well predict the maximum harvesting power.

□ End of chapter.

Chapter 5

Displacement and Base Excitations

To harvest energy from mechanical vibration with piezoelectric materials, different installations might be adopted according to the vibration conditions of the substrate structures. Surface mount and base excitation are two of the commonly utilized installations. For structure whose surface undertakes significant alternating deformation, the most direct way to harvest energy is to attach piezoelectric patches to the structural surface, as shown in Figure 5.1. On the other hand, for the structure whose surface has small deformation, but

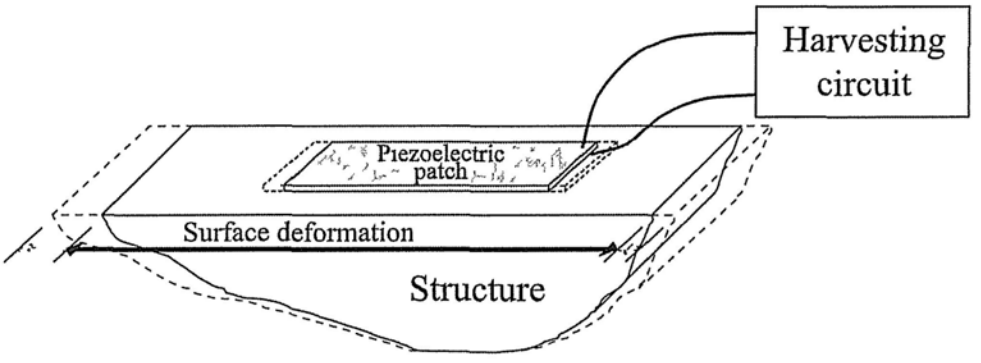

Figure 5.1: A surface mount PEH device.

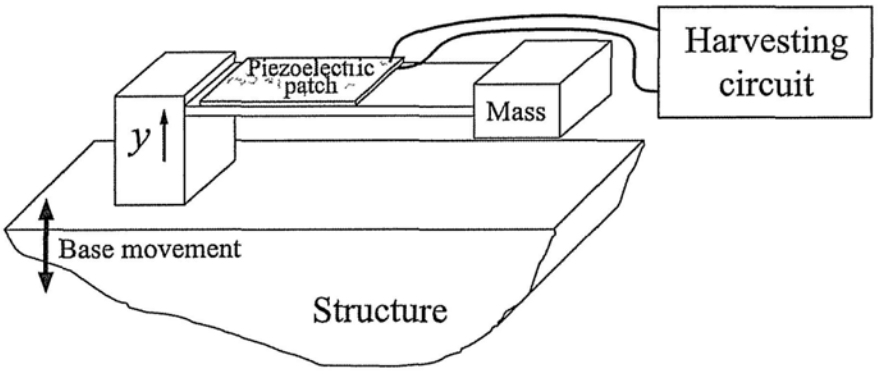

Figure 5.2: A base excited PEH device.

undergoes significant movement, it is more suitable to install a base excited PEH device to harvest energy. The configuration of a base excited PEH device is shown in Figure 5.2. Since the configurations of these two devices are different, their performances on energy harvesting might also be different. It would be interesting that given the same harvesting circuit connected to these two devices, how the different configurations influence the power generation.

Assuming that the installation of the PEH devices would not change the dynamics of the main structure, these configurations can be modeled as a general PEH device under displacement and force excitations, respectively. The two excitations correspond to two mechanical drive modes, i.e., strain-driven mode and stress-driven mode (Rodig et al., 2010). Comparison on the dynamics as well as power generation for PEH devices with a real harvesting interface circuit under these two excitations was not made in the previous literatures, since they oversimplified either the mechanical or electrical part. Based on the equivalent impedance network of a general PEH device, the overall dynamics was investigated in Chapter 4. In this chapter, the impedance technique is again utilized to analyze PEH devices, with emphasis on the differences under the two excitation conditions. Three of the above-studied interface circuits, i.e., SEH, P-SSHI, and S-SSHI are connected in turn as the interface circuit, so as to provide more insights on the harvesting performances of different harvesting devices under different excitations.

5.1 Displacement Excitation

The deformation magnitude of the piezoelectric element remains constant under displacement excitation. According to (2.22), the magnitude of the equivalent current i_{eq} is also constant when the excitation frequency is fixed. The harvesting power under displacement excitation therefore is given by

$$P_h = \frac{1}{2} I_{eq}^2(j\omega) R_h(j\omega, \tilde{V}_{rect}) \tag{5.1}$$

where R_h is the harvesting component shown in Figure 4.5. The expression on harvesting power is much simpler than that given by (4.23). Since I_{eq} is not related to $\tilde{V}_{rect}$, with a given excitation frequency, maximum P_h can be obtained when R_h reaches its maximum value.

The value of R_h differs when different interface circuit is connected. In the following parts, the harvesting power in displacement excited PEH devices with three different interface circuits, i.e., SEH, parallel-SSHI (P-SSHI), and series-SSHI (S-SSHI) are compared. The corresponding harvesting components R_h associated with these three interfaces are given in (4.15), (4.18), and (4.21), respectively. R_h in these three cases attain their maxima at

$$\left(\tilde{V}_{rect,opt}\right)_{SEH} = \frac{1-\tilde{V}_F}{2} \tag{5.2}$$

$$\left(\tilde{V}_{rect,opt}\right)_{P\text{-}SSHI} = \frac{1}{1+\gamma} - \frac{\tilde{V}_F}{2} \tag{5.3}$$

$$\left(\tilde{V}_{rect,opt}\right)_{S\text{-}SSHI} = \frac{1-\tilde{V}_F}{2} \tag{5.4}$$

When $V_{OC} \gg V_F$, we can neglect the $\tilde{V}_F$ terms in (5.2) $\sim$ (5.4) and obtain similar results to those proposed by Badel et al. (2006). It should be noted that the previous studies were emphasized on the optimization of the harvesting circuits under displacement excitation. Early literatures treated the piezoelectric structures as a current source in parallel with the piezoelectric capacitance C_p (Ottman et al., 2002). The implicit assumption of this equivalence is that the displacement magnitude is constant. Recent literatures started their analyses from differential equations, which are similar to (4.1) (Lefeuvre, Badel, Richard, Petit and Guyomar, 2006). Yet, in these studies, the force magnitude in fact was only used to determine the displacement magnitude at resonant frequency. Other than this, the analyses were all based on displacement excitation.

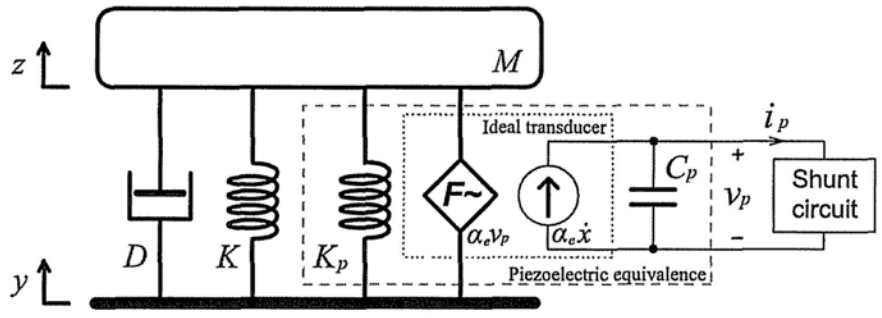

Figure 5.3: SDOF schematic representation of a base excited PEH device.

5.2 Base Excitation

Figure 5.3 shows the SDOF schematic representation of a PEH device under base excitation, where $y(t)$ is the base displacement, $z(t)$ is the displacement of the proof mass. In the base excitation case, the peak magnitude of the base acceleration, i.e., $\ddot{y}(t)$, remains constant. Denoting the relative displacement of the cantilever free end as $x(t) = z(t) - y(t)$, the dynamics of the base excited cantilever can be simplified into SDOF representation and described by the following equations

$$\begin{cases} M\ddot{x}(t) + D\dot{x}(t) + (K + K_p)x(t) + \alpha_e v_p(t) = -M\ddot{y}(t) \\ i_p(t) = \alpha_e \dot{x}(t) - C_p \dot{v}_p(t) \end{cases} \tag{5.5}$$

Comparing (4.1) and (5.5), and taking $-M\ddot{y}(t)$ as the equivalent force, the base excitation problem therefore is converted into force excitation.

Unlike that in displacement excitation, the dynamics of other components, in both mechanical and electrical parts, influence the vibration displacement, and subsequently affect the harvesting power. As introduced in Chapter 4, the harvesting power P_h can be calculated with the equivalent impedance network.

5.3 Comparison

The parameters of an experimental PEH device, which is introduced in Section 5.4, are given in Table 5.1. Based on these parameters; the harvesting powers with three interface circuits under two excitations are investigated. Figure 5.4 shows the contours of harvesting power P_h as well as the corresponding optimum $\tilde{V}_{rect}$ in six cases.

For displacement excitation, the magnitude of open circuit voltage V_{OC} under different excitation frequency maintains at 8.4 V. With the relation given in (3.6), the displacement magnitude of the equivalent mass is 0.92 mm. It can be observed from Figure 5.4 (a), (c), and (e) that the optimum $\tilde{V}_{rect}$ in all SEH, P-SSHI, and S-SSHI cases is constant under displacement excitation, in spite of the frequency difference. The optimum $\tilde{V}_{rect}$ under displacement excitation is located in the middle of the harvestable range (light gray in Figure 5.4) of $\tilde{V}_{rect}$, which is also expressed in (5.2) $\sim$ (5.4).

For base excitation, the applied acceleration to the base excited piezoelectric cantilever is 10 m/s^2 in RMS value. As observed from Figure 5.4 (b), (d), and (f), the optimum $\tilde{V}_{rect}$ varies with excitation frequency in the three cases. Guyomar et al. (2005) regarded the optimum $\tilde{V}_{rect}$ under force excitation (shown by dash curves in Figure 5.4) the same as that under displacement excitation, i.e., the middle points of the harvestable range (shown by dot curves); yet, it is shown in these figures that they are in fact different, in particular, the difference gets larger around the resonant frequency.

5.4 Experiments

The experimental setup is the same as that shown in Figure 4.6. A piezoceramic patch is bonded near the fixed end of an aluminum cantilever, where the longitudinal deformation of the piezoelectric element is generated according to the transverse vibration of the cantilever. But since the place of the permanent magnet, which also acts as a mass, have been changed, some parameters in the mechanical part needed to be measured again. The parametric changes are listed in Table 5.1.

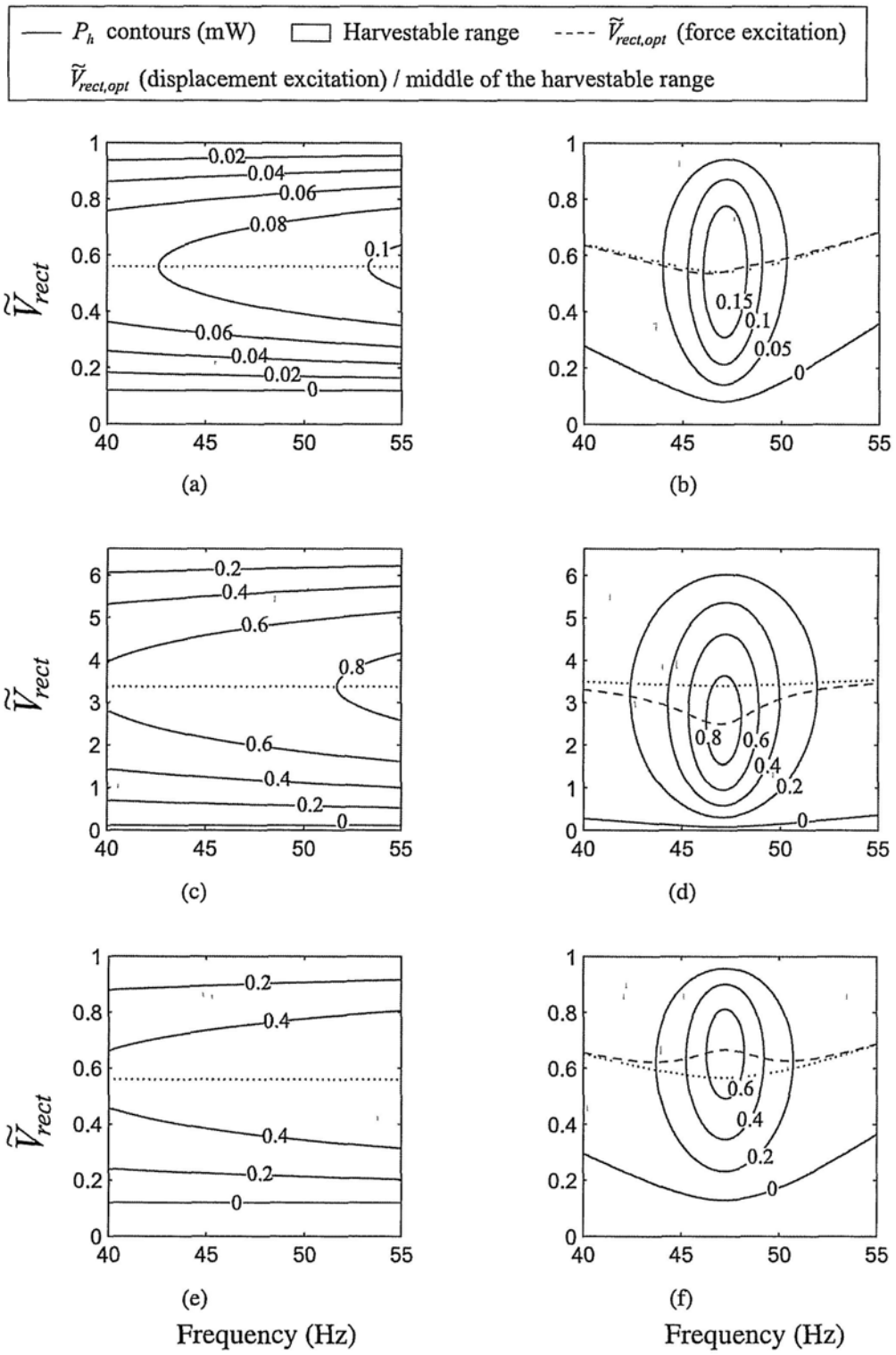

Figure 5.4: Contours of harvesting power P_h. (a) SEH, displacement excitation. (b) SEH, force excitation. (c) P-SSHI, displacement excitation. (d) P-SSHI, force excitation. (e) S-SSHI, displacement excitation. (f) S-SSHI, force excitation.

Table 5.1: Parametric changes in the experimental setup*.

Component	Value or model
α_e	3.12×10^{-4} NV
f_0	47.09 Hz
L	40.7 kH
C	280.67 pF
R	1 MΩ

* Other parameters are the same as those given in Table 4.1.

The relative displacement of the cantilever as well as the base acceleration might drift under different harvesting conditions. As long as the relative velocity is related with the relative displacement, to perform constant displacement excitation, the electromagnetic sensor is used to sense the relative velocity of the cantilever and then adjust the excitation signal for maintaining same displacement magnitude under different situations. For constant force excitation, it is adjusted by referring to the output of the accelerometer.

For any interface circuit connected, the harvesting power under different $\tilde{V}_{rect}$ can be experimentally obtained by connecting different DC load resistor R_{load} to the storage capacitor C_{rect} and calculating with the relation given in (4.28).

Figure 5.5 summarizes the theoretical and experimental results under three excitation frequencies near the resonant frequency in six cases (connecting with three interface circuits, under two excitations, respectively). The theoretical results agree with the experimental data quite well. We now compare the results of those two groups under different excitations. Under force excitation, the harvesting power declines significantly when the excitation frequency is away from the resonant frequency. While under displacement excitation, the changes in harvesting power are not significant for small frequency drift. In terms of the shape of a single curve under a specified excitation frequency, in displacement excitation, it is symmetric; while in force excitation, it is asymmetric.

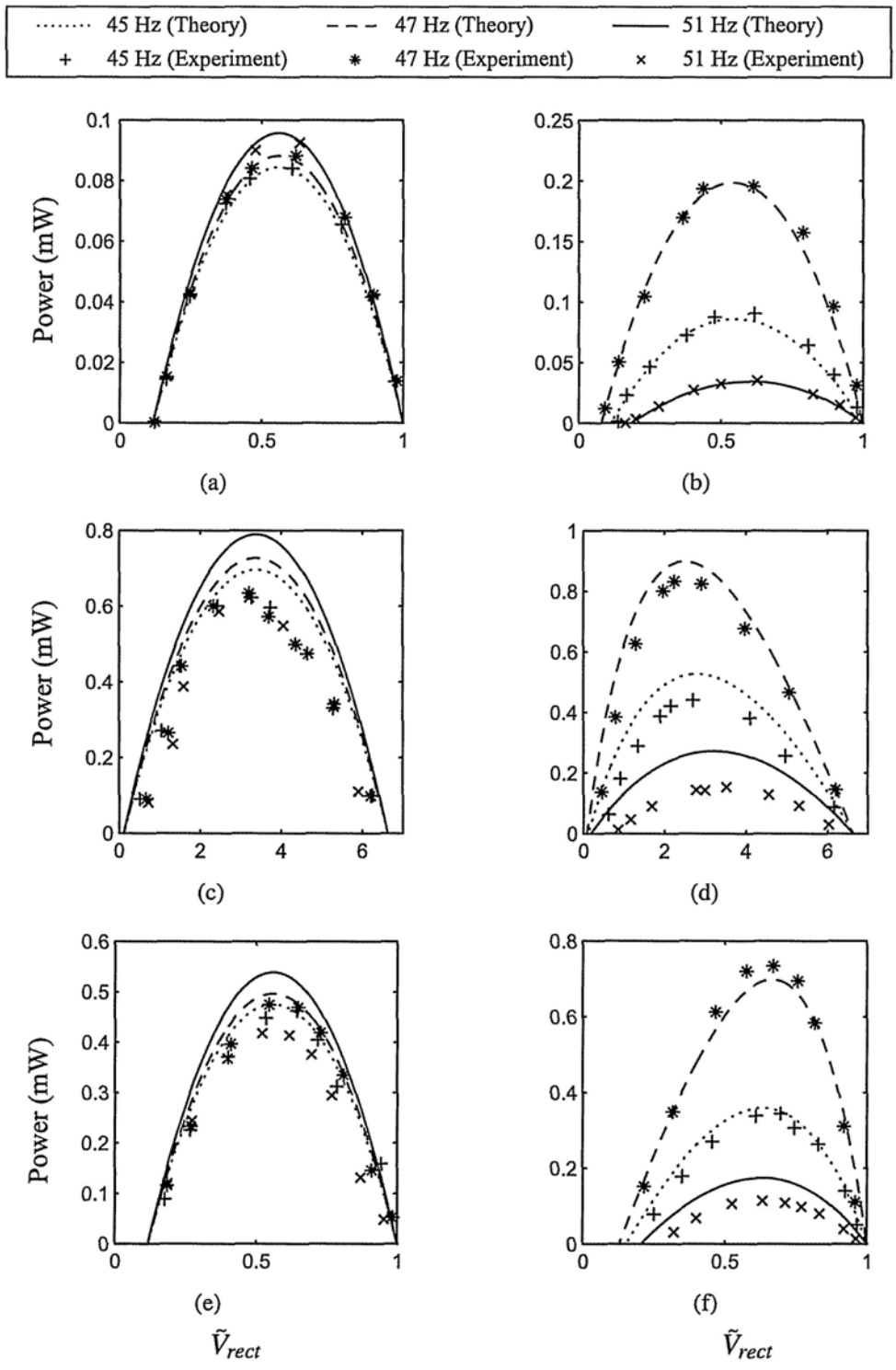

Figure 5.5: Theoretical and experimental harvesting power with three different interface circuits under two excitations, respectively. (a) SEH, displacement excitation. (b) SEH, force excitation. (c) P-SSHI, displacement excitation. (d) P-SSHI, force excitation. (e) S-SSHI, displacement excitation. (f) S-SSHI, force excitation.

5.5 Summary

Two installations of PEH devices, i.e., surface mount and base excitation, were discussed. Each of them should be adopted according to different vibration conditions of the substrate structure. The two configurations can be modeled as a general PEH device under two excitation manners, i.e., displacement and force excitations. The difference between those two excitations was discussed. Their performances in energy harvesting, in terms of harvesting power, were analyzed with the impedance based method. In particular, this method can accurately show how the harvesting performance (with real harvesting interface circuit) is influenced by the system dynamics under different excitation frequencies, which was never done in the previous studies.

□ End of chapter.

Chapter 6

Influence of Dielectric Loss in SSHI

In piezoelectric energy harvesting, the harvesting efficiency can be greatly improved by adopting the SSHI interface circuit. Most theoretical models were proposed with the emphasis on its ability to enhance harvesting efficiency. In the SSHI treatments, the inversion factor γ plays an important role. Theoretically, the harvesting power can reach infinity when $\gamma \to -1$ (under displacement excitation) (Lefeuvre, Badel, Richard, Petit and Guyomar, 2006).

The effective inversion was regarded to be only related to the quality factor of the inductive shortcut with the relation provided in (3.19). However, in real circuit, the inversion behavior is more complicated. It was found from experiments that, the voltage across the piezoelectric element reverses a little bit right after every voltage inversion across the piezoelectric element, so that the inversion effect produced by the switching RLC shortcut is weakened. This reversion, although small compared to the inversion, decreases the voltage magnitude a lot, therefore diminishes the harvesting efficiency. Most previous literatures on SSHI only emphasized its outstanding capability on enhancing the harvesting efficiency; the effective inversion factor used in calculation was obtained from measurement. This phenomenon on reversion and the difference between the ideal and effective inversion factors were ignored.

Although the analytical results, which use the measured effective inversion factor in calculation, agreed with experiments; the origin of the reversion after every switching action, as well as the quantitative relation between the ideal and effective inversion factors are also of interest. After experimentally investigating the SSHI circuit and waveforms, it was found that the reason of the reversion is attributed to the internal leakage within the piezoelectric element, which might be induced by dielectric loss. Besides the piezoelectric capacitance,

the dielectric loss is another important electrical characteristic of piezoelectric materials in practical energy harvesting systems. But it was seldom considered in the PEH researches. Early studies on piezoelectric ceramics have already shown that the dielectric loss increases remarkably under high-power operation (Hirose et al., 1993). Therefore, as SSHI boosts the voltage across the piezoelectric element, which increases the transduction power, the dielectric loss is not of little influence to a PEH system.

This chapter provides a detailed description on the phenomenon of voltage reversion after every inversion, as well as proposes a revised model to quantitatively analyze the influence of dielectric loss in PEH with SSHI interface.

6.1 Phenomenon

SSHI does provide an effective mechanism to increase the harvesting energy under same excitation level; the analytical results provided in the previous literatures match experiments as well. However, a phenomenon observed from the experimental waveform, which differs from that in ideal one, was ignored. In this section, with the focus on the S-SSHI interface, this phenomenon will be described and analyzed in detail.

Applying a 30 Hz constant (in magnitude) displacement excitation to a piezoelectric cantilever, whose first vibration resonant frequency is nearby, a 20 volt open circuit voltage is recorded across the piezoelectric element, i.e., $V_{OC} = 20$ volt. Figure 6.1(a) shows the voltage waveforms when S-SSHI treatment is activated under 7.6 volt rectified voltages, i.e., $V_{rect} = 7.6$ volt. Figure 6.1(b) shows the zoom-in view to one of the switching instants around time origin. When the switching command is applied, the voltage level before and after the switching action can be obtained as V_{on} and V_{off}, as indicated in Figure 6.1(b). Substituting the measured V_{on}, V_{off} , and V_{rect} into the equation of

$$V_{off} - V_{rect} = \gamma(V_{on} - V_{rect}) \tag{6.1}$$

yields the ideal inversion factor of the LCR shortcut $\gamma = -0.8$. Ideally, without any loss, the

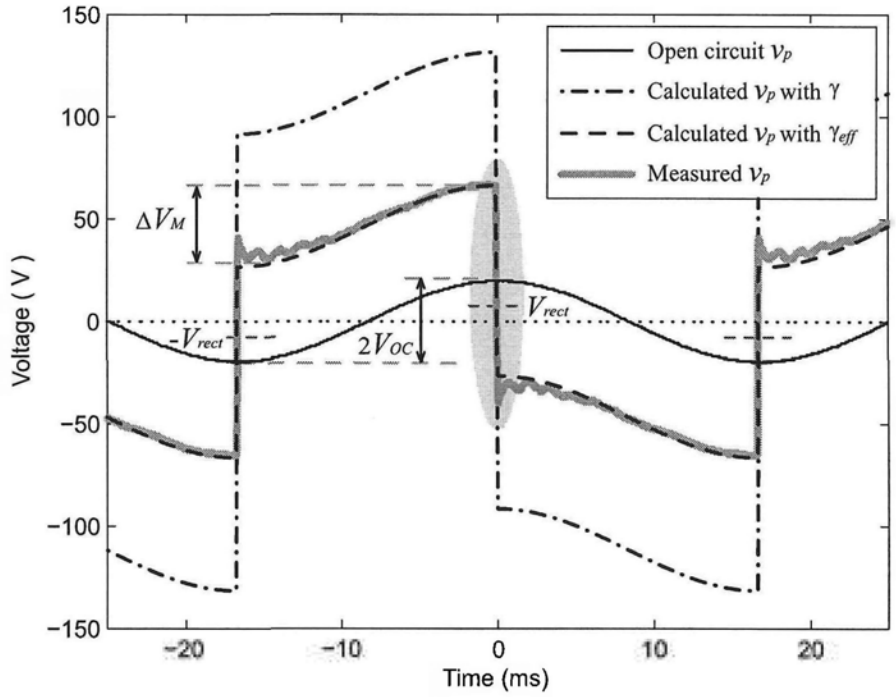

(a)

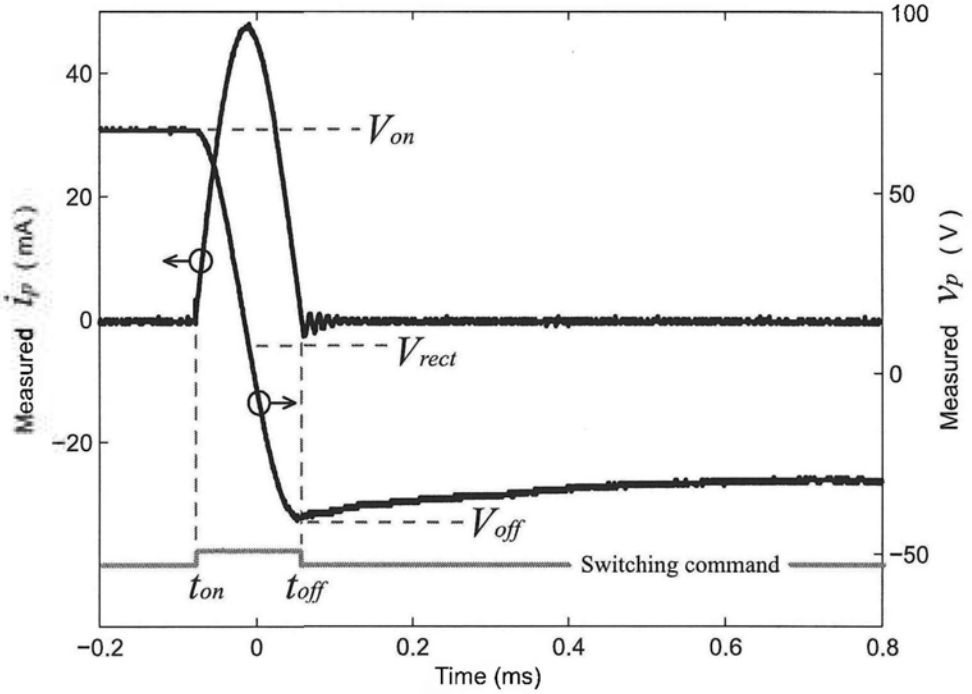

(b)

Figure 6.1: Characteristic waveforms in S-SSHI ($V_{OC} = 20$ volt, $V_{rect} = 7.6$ volt). (a) Voltages. (b) Zoom-in view to the voltage and current around time origin.

effect of SSHI treatment is to, intuitively, split the open circuit voltages at maxima places and move the adjacent parts against each other to some extent. Lefeuvre, Badel, Richard, Petit and Guyomar (2006) gave the formulas with which the S-SSHI characteristic voltage waveform can be theoretically obtained. Based on these formulas, the dash dot curve in Figure 6.1(a) shows the theoretical waveform of v_p with $\gamma = -0.8$. Nevertheless, there is a large error between the calculated result and the experimental one (gray bold curve). Two features, which differ from those in theoretical waveform, can be observed from the experimental waveform:

a) As highlighted by the ellipse area in Figure 6.1(a), the voltage v_p reverses somewhat right after every inversion. Small damped oscillation can be observed as well.
b) The measured voltage difference between two switching instants in S-SSHI, i.e., ΔV_M, as indicated in Figure 6.1(a), is smaller than, rather than equals to, that in open circuit condition, i.e., $2V_{OC}$.

For the first feature, similarities can be observed from the experimental waveforms provided by Guyomar et al. (2006); Lallart and Guyomar (2008); Richard et al. (2000). This reversion counteracts the inversion, therefore makes the effective inversion factor above the ideal inversion factor γ, implying that the inversion effect is weakened. A small reduction in the magnitude of the inversion factor usually causes large drop in the magnitude of v_p. The second feature imposes an equivalent effect as to decrease V_{OC}, which also results in the magnitude reduction of v_p. These two features were not pointed out in the previous literatures, not to mention the origin of them. However, their theoretical results still agreed with the experiments, because, instead of using the ideal inversion factor γ in calculation, they used the effective inversion factor (denoted as γ_{eff} in the following part of this chapter), which can be estimated by taking V_{off} as the voltage level after the reversion. But still, the reason about the voltage reversion, as well as the relation between γ and γ_{eff} are of interest.

These questions can be studied with an investigation to the voltage and current in one of the switching instants. As far as v_p is proportional to the charge stored in the piezoelectric capacitance C_p, the reversion of v_p after every inversion must be resulted from some current

leakage. For the observation of the instant current flowing through the treatment circuit during the switching instant, a 10 Ω current sampling resistor is connected to the treatment circuit in series. As shown in Figure 6.1(b), the switch begins to conduct at t_{on}, and then is blocked again at t_{off}. The current approaches zero quickly after the switching path is blocked again at t_{off}, in spite of some low level oscillation. However, v_p keeps reversing even no current leaks through the shunt circuit [1]. Therefore, the current leakage should take place internally within the piezoelectric element.

In essence, the voltage reversion in SSHI is caused by the dielectric loss within the piezoelectric element, which was not mentioned in the previous studies on PEH with SSHI.

On the other hand, in the studies for piezoelectric ceramics, it was reported that the influence of dielectric loss increases intensively under high-power operation (Hirose et al., 1993). As far as SSHI treatment boosts the voltage level across the piezoelectric element, as well as the conversion power, it is rational that the dielectric loss influences the harvesting system more, when conversion power is getting larger. The conventional model, as given in 2.5(b), which considered the piezoelectric element as a lossless component, is no longer capable to show details on the mechanism of voltage reversion in SSHI.

6.2 Analysis

6.2.1 Revised equivalent circuit

The high-power characteristics of piezoelectric transducers can be studied with a more comprehensive model (Umeda et al., 1998), based on which the internal losses can also be taken into account. In order to evaluate on the influence of dielectric loss in PEH system with SSHI interface, Figure 6.2 shows the revised equivalent circuit of a piezoelectric device. An equivalent parallel resistance (EPR) R_p is internally connected to the current source and the piezoelectric capacitance. The shunt circuit can be connected as either P-SSHI or S-SSHI.

[1] As far as oscilloscope probe with high input impedance is used in experiments, it is considered that little current leaks through the measurement process as well.

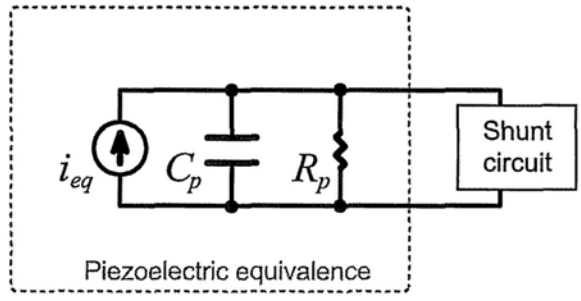

Figure 6.2: Revised equivalent circuit of a piezoelectric device.

During the harvesting process, the charge stored in C_p might leak internally through this EPR path, resulting in the voltage reversion and further magnitude reduction of v_p in SSHI.

6.2.2 Effective inversion factor

In S-SSHI treatment, besides (6.1), another relation links the voltages at the start (V_{off}) and end (V_{on}) of a switch-off interval. Mark one of the switching on maximum actions as time origin. The voltage v_p in the following half cycle is

$$v_p(t) = V_{off} + \frac{1}{C_p}\int_0^t \left[i_{eq}(t) - \frac{v_p(t)}{R_p}\right] \mathrm{d}t \tag{6.2}$$

As far as

$$v_p(T/2) = -V_{on} \tag{6.3}$$

where T is the period of mechanical excitation, and

$$\frac{1}{C_p}\int_0^{T/2} i_{eq}(t)\mathrm{d}t = -2V_{OC} \tag{6.4}$$

substituting (6.3) and (6.4) into (6.2) at $t = T/2$ instant, we can have

$$-V_{on} = V_{off} - 2V_{OC} - \frac{1}{R_p C_p}\int_0^{T/2} v_p(t)\mathrm{d}t \tag{6.5}$$

(6.5) can be further simplified by estimating $v_p(t)$ with its first-order approximation in this 0 to $T/2$ interval

$$\tilde{v}_p(t) = V_{off} - \frac{2(V_{on}+V_{off})}{T}t, \qquad t \in [0, T/2] \tag{6.6}$$

Substituting this approximated v_p into (6.5) yields

$$-V_{on} = V_{off} - 2V_{OC} - \frac{T}{4R_p C_p}(V_{off} - V_{on}) \tag{6.7}$$

where V_{OC}, the open circuit voltage can be directly measured without the SSHI circuit connected. With the two linear equations of (6.1) and (6.7), the values of V_{on} and V_{off} can be solved out.

In addition, at low excitation level, the difference between ΔV_M and $2V_{OC}$ is not significant, i.e., the effect produced by the second observed feature can be neglected, compared to that by first one. Considering the cancellation of reversion towards inversion, the pseudo V_{off}, i.e., voltage value after the reversion, is

$$V_{off,ps} = 2V_{OC} - V_{on} \tag{6.8}$$

This $V_{off,ps}$ is usually measured from experimental waveforms and taken as effective V_{off} in the previous studies. Furthermore, from (6.1) and (6.7), the effective inversion factor γ_{eff} is defined as

$$\gamma_{eff} = \frac{V_{off,ps} - V_{rect}}{V_{on} - V_{rect}} = \gamma + \frac{T}{4R_p C_p}(1-\gamma) \tag{6.9}$$

Since γ is less than one, therefore γ_{eff} is larger than γ. In general, the inversion effect is weakened. In Figure 6.1(a), it shows that, with γ_{eff}, the calculated waveform (dash curve)

approaches the experimental one quite well [2]. From (3.19), γ approaches -1 when the quality factor of the LCR path, i.e., Q, approaches infinity. Substituting this limitation on γ to (6.9), we can obtain the limitation of the effective inversion factor as

$$\lim_{\gamma \to -1} \gamma_{eff} = \frac{T}{2R_p C_p} - 1 \tag{6.10}$$

Obviously, the effective inversion factor γ_{eff} and also its limitation are not only determined by the quality factor of the switching LCR path, but also depend on the dielectric loss of the selected piezoelectric element, as well as the vibration period.

6.2.3 Energy flow

As pointed out in Chapter 3, energy harvesting is not the only function generated within the PEH system; during the harvesting process, another portion of energy may be dissipated in the conditioning circuits of the treatment. In addition, both energy harvesting and dissipation extract energy from the vibrating structure, and consequently bring out structural damping. Therefore, in order to have comprehensive evaluation to a certain PEH system, not only the harvesting capability, but also the side effect on energy dissipation should be taken into consideration.

With the analysis above, in an S-SSHI system, the amount of energy harvested in one cycle is

$$E_h = 2V_{store}C_p(V_{on} - V_{off}) \tag{6.11}$$

The amount of energy dissipated in one cycle is

$$E_d = C_p(V_{on} - V_{rect})^2(1-\gamma^2) + 2V_F C_p(V_{on} - V_{off}) + 2\int_0^{T/2} \frac{\tilde{v}_p(t)^2}{R_p} \mathrm{d}t \tag{6.12}$$

[2] Detailed parameters of the experimental system are provided in Section 6.3.

The three items in (6.12) are sequentially corresponding to: the dissipation induced by the equivalent series resistance (ESR) of the switching path, i.e., r in Figure 4.3; the dissipation induced by the bridge rectifier; and the dielectric loss induced by the EPR R_p [3].

6.3 Experiments

Experiments are performed, in order to measure the ERP R_p in the revised equivalent circuit, and further validate our analysis with an emphasis on energy flow.

The experimental setup is similar to that shown in Figure 4.6, except that no accelerometer is used here, because the experiments are carried out under displacement excitation. The piezoelectric structure's short circuit natural frequency f_{SC} and open circuit natural frequency f_{OC} are 27.06 Hz and 27.31 Hz, respectively. A 30 Hz displacement excitation is applied by the shaker.

6.3.1 Measuring the EPR R_p

The measurement on dielectric loss under high power operation is an issue. The loss is nonlinear, and it increases significantly under high power operation (Hirose et al., 1993; Umeda et al., 1998). In this analysis, a linear resistance R_p is used to approximately model the influence of dielectric loss. To determine the value of R_p, the voltages of V_{on} and V_{off} under different rectified voltage V_{rect} are measured first. As far as R_p is related to the theoretical V_{on} and V_{off} with (6.1) and (6.7), the value of R_p can be obtained simultaneously with the process of fitting the measured V_{on} and V_{off} data sets with the least square method.

The measured data as well as the fitted lines are shown in Figure 6.3. From the measured data, the ideal inversion factor $\gamma = -0.80$. From the curve fitting process, the corresponding $R_p = 2.07$ MΩ. Therefore, with (6.9), the effective inversion factor can be calculated $\gamma_{eff} = -0.59$.

[3] For simplicity, the first-order approximation of $v_p(t)$ is also used to estimate the dissipated energy here.

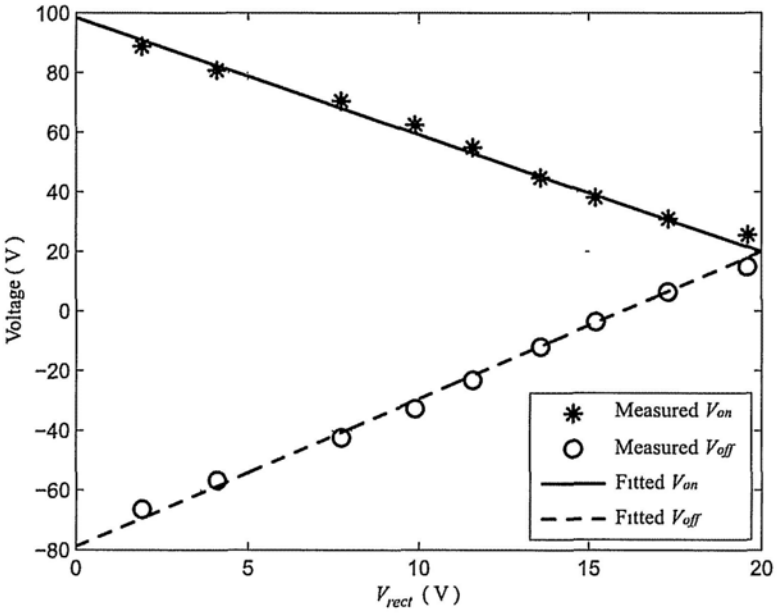

Figure 6.3: Fitting the experimental data of V_{on} and V_{off} to obtain the value of R_p.

6.3.2 Results

Experiments on both functions of energy harvesting and dissipation are performed in order to check their correlation to the revised theory, which includes the influence of dielectric loss. Load resistors with different values are connected as DC load. Recording the voltage V_{store} across the load, the harvesting power can be obtained with the Joule's laws. As for the energy dissipation, three parts should be measured individually. Power dissipated by the bridge rectifier is related to the harvesting. A sampling resistor is connected to the switching path to extract the RMS current flowing through the path, so as to estimate the power dissipation of its ESR r. The dissipation by R_p can be obtained with the RMS value of v_p.

For theoretical result, as (6.11) and (6.12) give the harvested and dissipated energy in every vibration cycle, multiplying E_h and E_d with the excitation frequency $f_0 = 30$ Hz yields the power on energy harvesting and dissipation, i.e., P_h and P_d, as shown in Figure 6.4. Meanwhile, besides the absolute power, the relative indices, i.e., efficiencies on energy harvesting and dissipation towards the energy associated with vibration are also of interest.

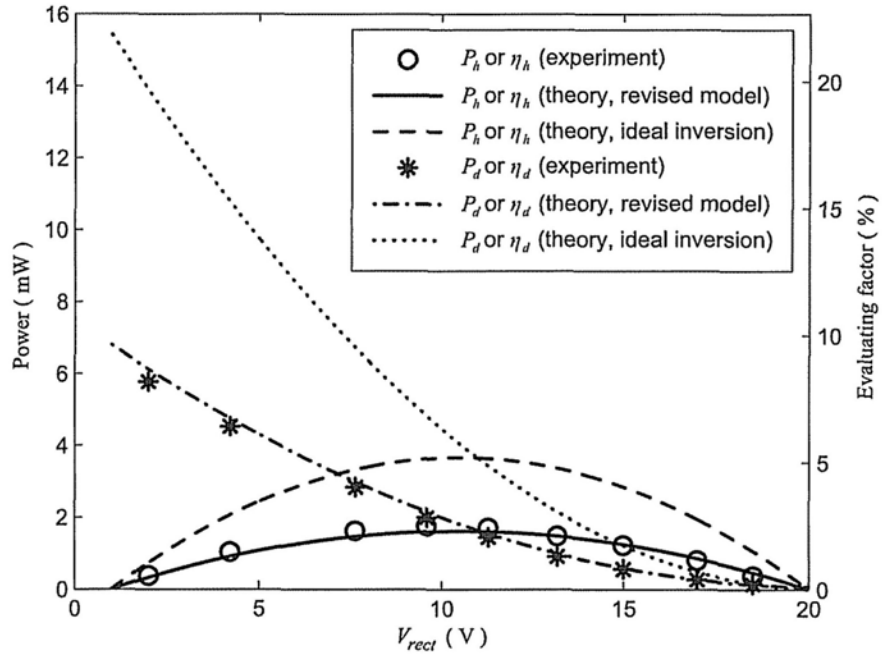

Figure 6.4: Power and evaluating factors in PEH with S-SSHI interface.

These two indices were defined as harvesting factor η_h and dissipation factor η_d in subsection 3.1.2. In this study, since constant displacement excitation is applied [4], the energy associated with vibration, usually denoted as E_{max}, does not change. It can be derived with the coupling coefficient k_d^2, which can be obtained with the natural frequencies under open and short circuit conditions, i.e., f_{OC} and f_{SC} according to (2.10). With the definition on η_h and η_d, they are proportional to P_h and P_d. The corresponding scale of the two evaluating factors is given by the right vertical axis in Figure 6.4.

Figure 6.4 shows that both experimental results and theoretical analyses agree with each other well. In addition, for comparison, the theoretical result with ideal inversion, i.e., assuming no reversion follows inversion, is also shown. Both predicted harvested power and dissipated power with this model are nearly 100% higher than those in real situation. Therefore, the reversion produced by dielectric loss, although small compared to the inversion,

[4] The relative displacement between the cantilever and the base may change when the SSHI treatment is activated. In experiment, the shaker input is adjusted to maintain the same vibration level according to the sensed velocity.

significantly degrades the efficiencies on energy harvesting and dissipation.

6.4 Summary

Based on the previous theoretical analyses on PEH with SSHI interface, it was considered that, by adopting a really low loss switching RLC path, the harvesting power can be pushed towards infinity under displacement excitation. Yet, in this chapter, we showed that the power harvested is also much related to the dielectric loss within the piezoelectric element. This loss causes the voltage reversion across the piezoelectric element after every inversion, weakens the inversion effect, and consequently reduces the voltage magnitude as well as the harvesting efficiency a lot. The phenomenon on voltage inversion was explained. A revised model was proposed to include the influence of dielectric loss in the analysis. With this model, the relation between ideal and effective inversion factor was obtained; limitation on the effective inversion factor was discussed. Theoretical result of this revised model showed good agreement with the experimental data. In addition, for overall evaluation of PEH systems, instead of merely focusing on the harvesting power, the energy flow including harvested and dissipated energy and also their corresponding evaluating factors were emphasized.

□ End of chapter.

Chapter 7

Self-powered Switching Interface Circuit

To implement SSHI, a displacement / velocity sensor and a controller are usually needed for synchronization and generation of switching commands (Guyomar et al., 2005; Lefeuvre, Badel, Richard, Petit and Guyomar, 2006; Makihara et al., 2006). In the experimental setup introduced in sub-section 3.3.4 and shown in Figure 3.16, an inductive displacement sensor and a PC based controller board (dSPACE DS1104) were used to carry out synchronized switching control. In that setup, both of the sensing and control units need external power, whose amount might be much larger than that of the harvested power. It is acceptable for experiments in laboratory, but unsuitable for practical implementation. The experimental setup shown in Figure 4.6 was used in the experiments introduced in Section 4.4, Section 5.4 and Section 6.3. An electromagnetic velocity sensor and a micro-controller board were used for synchronization and switching control. In the second setup, the velocity sensing was self-powered; while the low power micro-controller was powered by batteries. The self-powered version of micro-controller based PEH system will be investigated in the future work.

Besides using separated sensor and controller to implement SSHI, Lallart and Guyomar (2008); Qiu et al. (2009) investigated the self-powered SSHI, which simultaneously use the piezoelectric element as displacement sensor and power the switching components with the harvested energy. Based on their experiment, Lallart and Guyomar (2008) claimed that the self-powered SSHI can harvest 1.6 times more of power than SEH. They have also considered the influence of voltage gaps, which are produced by diodes and transistors in the circuit, over the harvested power. Yet, the influences of other components, e.g., the capacitance of the envelope detector, have not been pointed out. Besides, two important parameters, i.e., the switching delay phase φ and inversion factor γ were regarded as constants. But in fact,

these two parameters are constants only when the open circuit voltage V_{OC} (related to maximum displacement) and storage voltage V_{store} (voltage across C_{rect}) are constants. A more complete analysis should take these into account, in order to compare the energy harvesting efficiencies under different V_{OC} and V_{store}. Besides, some concerns about the self-powered SSHI were still unanswered, e.g.,

a) Is there any constraint or applicable range for this treatment?

b) Does the self-powered SSHI always outperform SEH?

In this chapter, a modified circuit and an improved analysis for self-powered SSHI are proposed. With the modified circuit, direct peak detection and better isolation among different units within the circuit can be achieved, both of which result in further removal on dissipative components. In the improved analysis, details in open circuit voltage, switching phase lag, and voltage inversion factor are discussed, all of which lead to a better understanding to the working principle of the self-powered SSHI.

7.1 Circuit

The essence of the self-powered SSHI technique proposed by Lallart and Guyomar (2008) is the electronic breaker, which can automatically perform switching action without providing external power when the potential difference across the switch reaches its maximum. Since one breaker can only allow current flow in one direction, replacing the switch *sw* in Figure 4.3 with two of such breakers (one as maximum breaker and the other, which was inversely connected, as minimum breaker), the self-powered SSHI can be achieved. The breaker consists of three parts: envelope detector, comparator, and switch. In their design, the envelope detectors are in series with the clamped capacitance C_p and inductor L. The detected voltage in fact is not v_p, but the voltage sum of v_p and the voltage across L. Even L is connected to C_p for a very short interval in every cycle, the hard switching-off action introduces high frequency components to L. The local maxima or minima produced by these high frequency components may induce misjudgement to the other breaker. Therefore, both

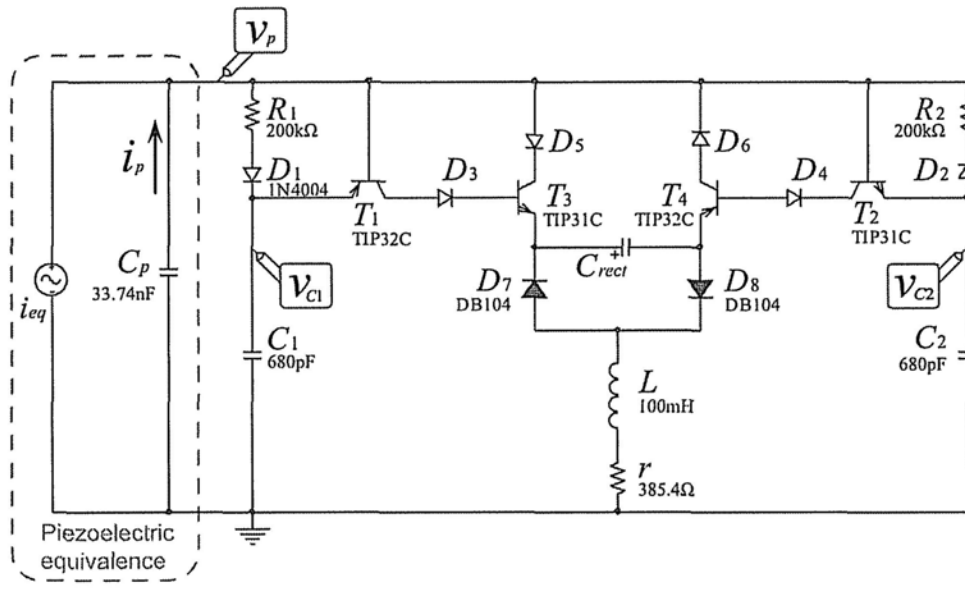

Figure 7.1: Modified self-powered SSHI circuit.

envelope detector and comparator parts should be carefully isolated from the switching path. For the breaker introduced by Lallart and Guyomar (2008), two resistors were connected for isolation purpose. Yet, the principle and design guideline were not clearly addressed.

Taking these envelope detection and isolation issues into consideration, in our self-powered design, we use a complementary transistors topology to achieve both direct envelope detection for v_p and reduction on the interference among different parts in the breakers. With this reformation, all isolating resistors, which are bound to consume some energy, can be removed. The modified circuit is shown in Figure 7.1. We obtain its waveforms (Figure 7.2), as well as the zoom in view to one of the processes of switching on maximum (Figure 7.3) with PSpice simulation. The part values and models given in Figure 7.1 are also corresponding to those in the experimental circuit introduced in Section 7.3 [1].

Accompanying with the vibration, switching actions take places when v_p reaches its maximum or minimum in every cycle. Different from the ordinary SSHI interface, which has only one voltage inversion in each switching action, in the self-powered SSHI circuit, two

[1] Because of the difference between the simulation models and real parts, in simulation, to properly start up the switching processes, C_1 and C_2 are set to be 2 nF.

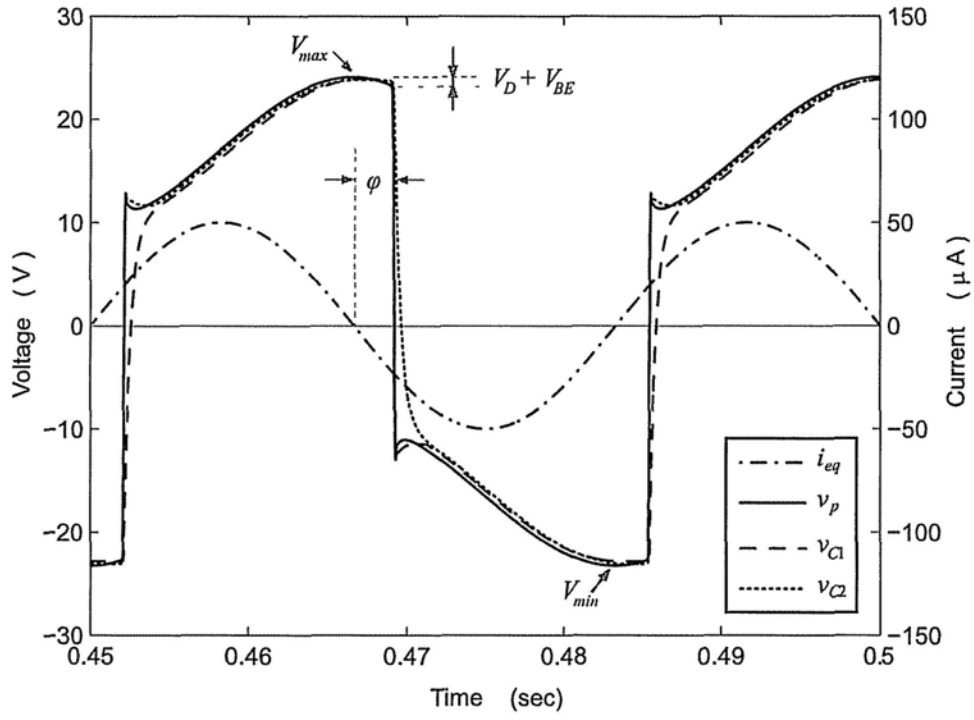

Figure 7.2: Simulation waveforms in modified self-powered SSHI.

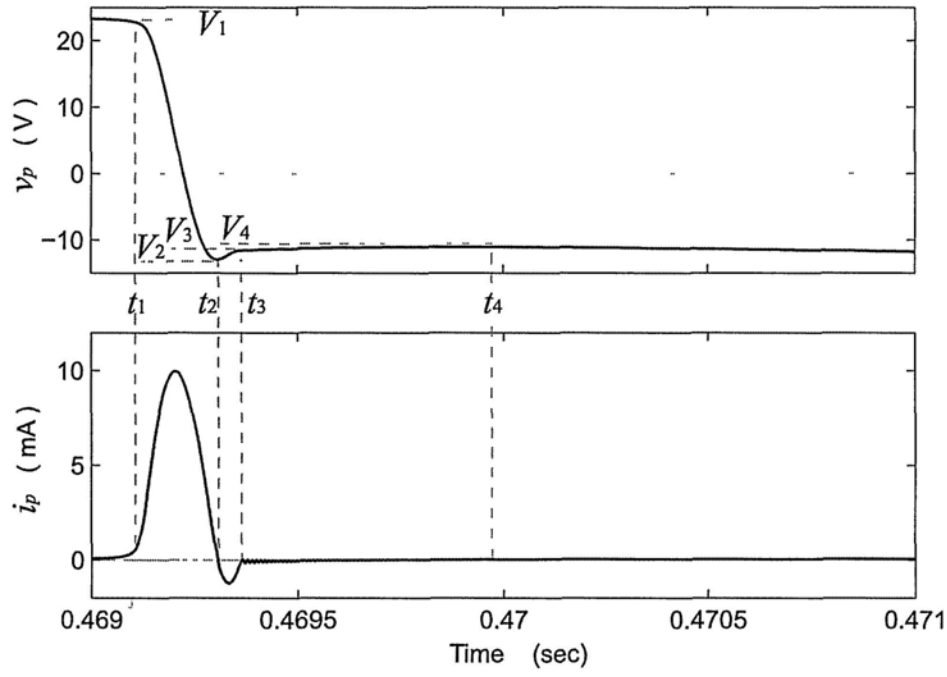

Figure 7.3: v_p and i_p waveforms in the process of switching on maximum.

voltage inversions and one charge neutralization are experienced for exerting each switching action.

Take switching on maximum for example. In switching on maximum, R_1, D_1 and C_1 form an envelope detector. T_1 and T_3 are cut off most of the time in a cycle.

First inversion

When v_p reaches its maximum V_{max}, the voltage across C_1 is $V_{max} - V_D$, where V_D denotes the forward voltage drop of a diode. Then v_p begins to drop. When the decrease reaches $V_D + V_{BE}$, i.e. $v_p = V_1$ (t_1 instant in Figure 7.3), T_1 conducts [2]. C_1 begins to discharge through $T_{1(ec)}$, D_3, $T_{3(be)}$, C_{rect}, D_8, L and r, consequently makes T_3 conduct[3]. The conduction of T_3 switches on the inductive path that consists of D_5, $T_{3(ce)}$, C_{rect}, D_8, L and r, producing a shortcut to the charge in C_p and C_2 (through D_2, R_2). For C_p, it starts a quick discharge from the voltage of V_1 through the RLC loop, until v_p reaches its local minimum V_2 (t_2 instant in Figure 7.3).

Second inversion

The current through L now tends to reverse its flowing direction, but the $T_{3(ce)}$ path is immediately blocked by reverse D_5. Yet, the path consists of D_7, C_{rect}, $T_{4(ec)}$, D_6 is still available. Because even T_4 is cut off, there is a small parasitic capacitance across its emitter and collector, which is uncharged. The current will stop flowing until T_4's emitter-collector capacitance C_{CE} is charged, at which very instant v_p becomes V_3 (t_3 instant in Figure 7.3). This local minimum of v_p, i.e. V_2, may induce misjudgement for the minimum breaker. So R_2 is necessary for making sure that C_2, which is used for minimum detection, discharges slower than C_p, so as to skip over this local minimum.

---

[2] V_{BE} denotes the transistor base-emitter threshold voltage.

[3] r is the equivalent series resistance of L.

Charge neutralization

After t_3, both T_3 and T_4 are cut off; however, C_2 still has not finished its discharging, the rest of the charge in C_2 will flow into C_p and C_1 until they are the same in voltage. This charge neutralization again increases v_p a little bit to V_4 (t_4 instant in Figure 7.3) before v_p enters the following half cycle of minimum detection.

Switching on minimum makes use of the counterparts in the circuit, and its principle is similar to that of switching on maximum.

7.2 Analysis

In Section 7.1, the working principle of the modified self-powered SSHI circuit has been introduced. Based on this, detailed and quantitative analysis is provided in this section.

7.2.1 Open circuit voltage

Regardless of switching on maximum or minimum, the current through C_{rect} is always positive, so C_{rect} acts as energy storage. On the contrary, the average power to C_1 and C_2 is zero. They never sustain energy in themselves, so it is unsuitable to regard them as energy storage as did by Lallart and Guyomar (2008). Rather, C_1 and C_2 can be equivalently regarded as two capacitors connected in parallel to C_p. This approximation is validated from Figure 7.2, since both v_{C1} and v_{C2} are very close to v_p. Given the harmonic displacement excitation as

$$x(t) = X\sin(\omega t) \tag{7.1}$$

where X is the amplitude of maximum displacement, ω is the vibration circular frequency. With (2.22), the equivalent current source should be

$$i_{eq}(t) = \alpha_e X \omega \cos(\omega t) \tag{7.2}$$

With the parallel connections of C_p, C_1 and C_2, at open circuit condition, v_p becomes

$$v_{p,oc}(t) = V_{OC}\sin(\omega t) \tag{7.3}$$

where

$$V_{OC} = \frac{\alpha_e X}{C_p + 2C_{ed}} \tag{7.4}$$

is the open circuit voltage, representing the amplitude of $v_{p,oc}$. Because the capacitances of envelope detecting capacitors C_1 and C_2 are selected to be the same, they are denoted as C_{ed} in (7.4). Without shunt circuit connected, the open circuit voltage of the original piezoelectric element is

$$V_{OC,org} = \frac{\alpha_e X}{C_p} \tag{7.5}$$

Therefore, (7.4) implies that the open circuit voltage in self-powered SSHI will be slightly reduced under the same excitation.

In addition, to effectively drive the switches, there is a constraint for V_{OC}, which is set by the forward voltage gaps of diodes and transistors in the circuit. To figure out the constraint, suppose no any switching action is performed before the connection of the circuit. Once it is connected, the first switching action may start after v_p attains, for example, its maximum, i.e. V_{OC}, and then drop to $V_{OC} - V_D - V_{BE}$. At this time, T_1 will conduct only when v_{C1} is larger than the voltage gap produced by $T_{1(ec)}$, D_3, $T_{3(be)}$, C_{rect}, D_8 in series; and T_3 will conduct only when v_p is larger than the voltage gap produced by D_5, $T_{3(ce)}$, C_{rect}, D_8 in series. Both yield the same constraint for V_{OC} as

$$V_{OC} > V_{CE(sat)} + 3V_D + V_{BE} + V_{store} \tag{7.6}$$

where $V_{CE(sat)}$ is the collector-emitter saturation voltage of corresponding transistors, V_{store} is the rectified voltage, i.e., the voltage across C_{rect}.

On the other hand, given a V_{OC} satisfying (7.6), we can obtain the maximum attainable V_{store} in energy harvesting from (7.6), as follows:

$$V_{store,max} = V_{OC} - V_{CE(sat)} - 3V_D - V_{BE} \tag{7.7}$$

7.2.2 Switching phase lag

From the principle of SSHI (Lefeuvre, Badel, Richard, Petit and Guyomar, 2006), the switching actions should be taken at the right instants when v_p attains its extreme values, i.e., V_{max} or V_{min} in Figure 7.2. In self-powered SSHI, however, to switch at the very instants is impossible; due to the voltage gaps of diode and transistor in envelope detector and comparator, there is always a phase lag between the instants of switching action start and maximum displacement (also $i_{eq} = 0$). The phase lag was defined as φ and regarded as constant in Lallart and Guyomar (2008). Nevertheless, φ in fact changes with V_{OC}, with the relation of

$$\varphi = \cos^{-1}\left(1 - \frac{V_D + V_{BE}}{V_{OC}}\right) \tag{7.8}$$

Considering the constraint on V_{OC} given in (7.6), the range of φ can be obtained as

$$0 < \varphi < \cos^{-1}\left[\frac{V_{CE(sat)} + 2V_D + V_{store}}{V_{CE(sat)} + 3V_D + V_{BE} + V_{store}}\right] \tag{7.9}$$

The lower limit corresponds to infinite V_{OC}; the upper one corresponds to minimum harvestable V_{OC}.

7.2.3 Voltage inversion factor

The voltage inversion factor γ is an important parameter in SSHI. It makes use of the natural oscillation of an RLC circuit, so as to perform a quick inversion for v_p at right instants. The voltage inversion factor was defined in (3.19). This definition includes the sign information,

therefore is more general, compared to that given by Lallart and Guyomar (2008).

As described in Section 7.1 and illustrated in Figure 7.3, the switching process in self-powered SSHI is more complex than that in ordinary SSHI. It might go through two inversion steps and one charge neutralization before the voltage changes from V_1 to V_4. Among these three steps, there are two intermediate values, which were denominated as V_2 and V_3 in Figure 7.3. Taking switching on maximum as example, if $V_1 > V_{ref1}$, where

$$V_{ref1} = V_{CE(sat)} + 2V_D + V_{store} \tag{7.10}$$

is the first reference voltage gap, v_p will experience the first inversion. For the first inversion, i.e. from V_1 to V_2, $C_p + C_1$, L and r form the RLC loop for discharging, with the quality factor of

$$Q_1 = \frac{1}{r}\sqrt{\frac{L}{C_p + C_{ed}}} \tag{7.11}$$

The relation between V_2 and V_1 can be obtained as

$$V_2 - V_{ref1} = \gamma_1 (V_1 - V_{ref1}) \tag{7.12}$$

where

$$\gamma_1 = \begin{cases} -e^{-\pi/(2Q_1)}, & V_1 > V_{ref1}; \\ 1, & \text{others} \end{cases} \tag{7.13}$$

is the inversion factor for the $C_p + C_1$, L and r loop, whose quality factor is Q_1.

After the first inversion, if $V_2 < V_{ref2}$, where

$$V_{ref2} = -2V_D - V_{store} \tag{7.14}$$

is the second reference voltage gap, v_p will experience one more inversion. For the second inversion, i.e. from V_2 to V_3, C_p in series with C_{CE}, L and r form the RLC loop for

discharging, with the quality factor of

$$Q_2 = \frac{1}{r}\sqrt{\frac{L(C_p + C_{CE})}{C_p C_{CE}}} \tag{7.15}$$

The relation between V_3 and V_2 can be obtained as [4]

$$V_3 - \frac{C_p}{C_{CE}}(V_2 - V_3) - V_{ref2} = \gamma_2(V_2 - V_{ref2}) \tag{7.16}$$

where

$$\gamma_2 = \begin{cases} -e^{-\pi/(2Q_2)}, & V_2 < V_{ref2}; \\ 1, & \text{others} \end{cases} \tag{7.17}$$

is the inversion factor for the corresponding RLC loop, whose quality factor is Q_2.

The charge neutralization follows the second inversion. Since the resistor R_2 is used for slowing down the discharging process of C_2, roughly speaking, the time constant of R_2C_2 should be larger than τ, which was given in (3.18). So we can simply assume that the discharge of C_2 starts after the two inversion of v_p. In the charge neutralization, the total charge in C_p, C_1 and C_2 is unchanged. Considering their original voltage, V_4 is related to V_1, V_2 and V_3 with the following equation

$$(2C_{ed} + C_p)V_4 = C_{ed}(V_1 + V_2) + C_p V_3 \tag{7.18}$$

One more relation links V_1, V_4 and the open circuit voltage V_{OC}, i.e.,

$$V_1 + V_4 = 2V_{OC}\cos\varphi \tag{7.19}$$

[4] For detailed analysis on the voltage inversion in double-cap RLC circuit, please refer to Section A.1.

$V_1 \sim V_4$ can be expressed in terms of V_{OC} and V_{store} by solving the linear equations of (7.12), (7.16), (7.18) and (7.19).

Because of the complementary topology, for switching on minimum, the four corresponding voltages are $-V_1$, $-V_2$, $-V_3$, and $-V_4$, respectively.

7.2.4 Harvesting power

Based on the above analyses about the influences of self-powered implementation to the open circuit voltage, switching phase lag and voltage inversion factor in SSHI, the analysis on harvesting power can be carried out.

In each vibration cycle, the harvested energy of the self-powered SSHI is

$$E_{SP-SSHI} = 2V_{store}[C_p(V_1 + V_3 - 2V_2) + C_{ed}(V_1 - V_2)] \tag{7.20}$$

Multiplying $E_{SP-SSHI}$ by the vibration frequency yields the harvesting power of the self-powered SSHI, as

$$P_{SP-SSHI} = f_0 E_{SP-SSHI} \tag{7.21}$$

where $f_0 = \omega/(2\pi)$ is the vibration frequency.

Besides, for SEH and ideal SSHI [5], the harvesting powers are

$$P_{SEH} = 4f_0 C_p V_{store}(V_{OC,org} - V_{store} - 2V_D) \tag{7.22}$$

$$P_{SSHI} = 4f_0 C_p V_{store}(V_{OC,org} - V_{store} - 2V_D)\frac{1-\gamma}{1+\gamma} \tag{7.23}$$

respectively (Lallart and Guyomar, 2008; Lefeuvre, Badel, Richard, Petit and Guyomar, 2006).

[5] In ideal SSHI, the sensing and switching control units do not bring any V_{OC} influence, switching phase delay, and voltage gap to the circuit. However, the voltage gap of bridge rectifier is considered nonzero.

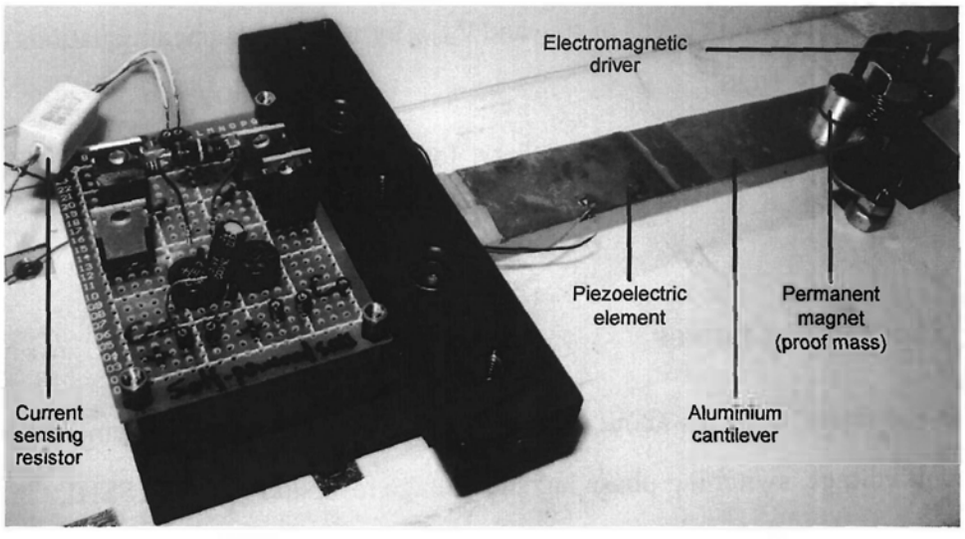

Figure 7.4: Experimental setup of self-powered SSHI.

Table 7.1: Self-powered SSHI circuit parameters.

Name	Symbol	Value
Diode forward voltage drop	V_D	0.5 V
Transistor base-emitter on voltage	V_{BE}	0.5 V
Transistor collector-emitter saturation voltage	$V_{CE(sat)}$	1.2 V *
Transistor emitter-collector capacitance	C_{CE}	150 pF **
Voltage inversion factor	γ_1	-0.52

* & ** The data are from ON Semiconductor (2008).

7.3 Experiments

Experiments are performed in order to evaluate the performance of practical self-powered SSHI. The experimental setup is shown in Figure 7.4. It is built up with a piezoelectric cantilever and the modified self-powered SSHI interface circuitry.

The main mechanical structure is an aluminium cantilever whose fixed end is fixed on the vibration-free table and the free end is driven by an electromagnetic driver. A piezo-

Table 7.2: Measured changes on open circuit voltage.

$V_{OC,org}$ (V)	V_{OC} (V)	$V_{OC}/V_{OC,org}$
10.1	9.7	0.9604
15.2	14.6	0.9605
20	9.2	0.9600

ceramic patch of 49 mm × 24 mm × 0.508 mm (T120-A4E-602, Piezo System, Inc.) is bonded near the fixed end where the largest strain happens along the cantilever. A permanent magnet is attached at the free end of the cantilever, so as to achieve the coupling with the electromagnetic driver; and it also acts as a proof mass to lower the vibration frequency and increase the displacement of the free end. A function generator (33120A, Agilent Co.), following by a power amplifier (2706, B&K Co.), provides a 30Hz sinusoidal excitation to the electromagnetic coil. To perform constant displacement excitation, an inductive displacement sensor (JCW-24SR, CNHF Co.), which is not shown in Figure 7.4, is used to sense the displacement of the cantilever for adjustment under different situations.

For the circuitry, component models and values are the same as those shown in Figure 7.1. Other circuit parameters are given in Table 7.1.

In experiments, firstly, the changes on open circuit voltage before and after the connection of self-powered SSHI circuit are checked under three excitation levels. As shown in Table 7.2, the ratios of $V_{OC}/V_{OC,org}$ in these three situations agree with the ratio of $C_p/(C_p+2C_{ed}) = 0.9613$ in our experiment, which verified the analysis on open circuit voltage in Section 7.2.

Also under those three excitation levels, the harvesting power is measured as function of storage voltage V_{store}. Resistors with different resistance values are connected as loads one by one. With the corresponding measured DC voltage across each resistor, the harvesting power under different V_{store} can be obtained. The experimental results of $P_{SP-SSHI}$ and P_{SEH} under three excitation levels, together with the analyzed $P_{SP-SSHI}$, P_{SEH} and P_{SSHI} are given in

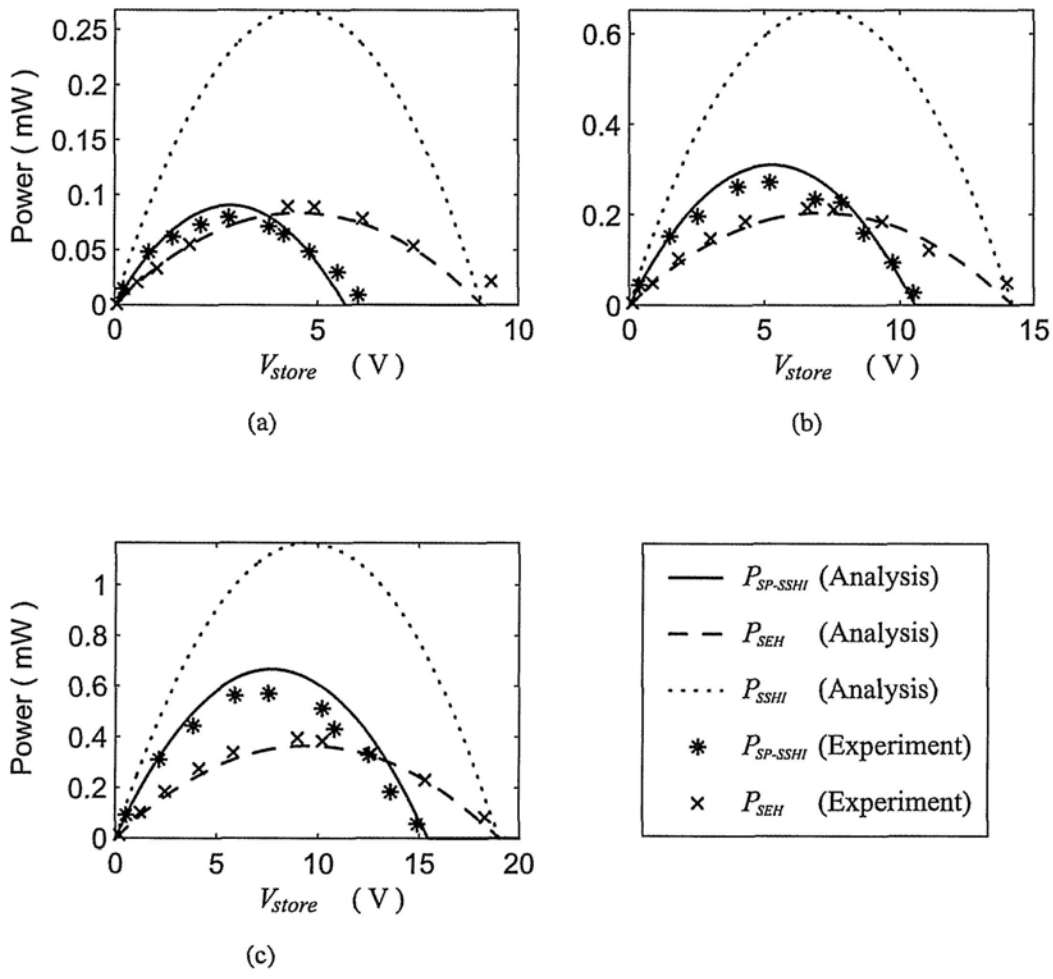

Figure 7.5: Harvesting power under different excitation levels in self-powered SSHI. (a) $V_{OC,org} = 10.1$ V. (b) $V_{OC,org} = 15.2$ V. (c) $V_{OC,org} = 20$ V.

Figure 7.5 for comparison.

From the three sub-figures in Figure 7.5, both analytical and experimental results show good agreement with each other. Comparing the self-powered SSHI to the ideal SSHI, the higher the excitation level, the closer between $P_{SP-SSHI}$ and P_{SSHI}. On the other hand, comparing the self-powered SSHI to SEH, the maximum harvesting power in self-powered SSHI is larger than that in SEH only when the excitation level is high enough. Therefore, rather than claiming that self-powered SSHI always outperforms SEH, we should note that there should be a critical excitation level, below which this claim is unconvincing.

7.4 Summary

The introduction of the self-powered version of synchronized switching harvesting on inductor (SSHI) treatment did open a promising territory for piezoelectric energy harvesting with switching technique. Nevertheless, many issues still lie in further improvements on both circuitry and precise modeling. We proposed a modified circuitry for self-powered SSHI. Compared to the circuitry proposed by Lallart and Guyomar (2008), the modified circuitry not only minimizes the interference among different units in the circuit, so as can enhance the switching performance; but also results in the removal of some resistive components, so as can further diminish the energy dissipation within the switching processes. Improved analysis was carried out considering three aspects of open circuit voltage, switching phase lag, and voltage inversion factor. Unlike the ideal SSHI, which always has better harvesting capability than SEH, it was found from both analyses and experiments that, for self-powered SSHI, only when the excitation level is high enough, it can outperform SEH. Moreover, the higher the excitation level, the more significant the enhancement on harvesting power; therefore, the more beneficial to replace the standard interface with such self-powered switching interface for piezoelectric energy harvesting.

□ End of chapter.

Chapter 8

Conclusion

Systematic investigation and interface circuit analysis were extensively studied in this thesis. These two issues are related, because the introduction of synchronized switching harvesting interface circuits has raised attentions to some previously ignored details in the research of piezoelectric energy harvesting (PEH) systems.

The first issue that has been investigated was the energy flow within PEH systems. The concept on energy flow was discussed in some of the previous literatures, but never discussed in-depth. In this thesis, besides qualitatively understand the possible energy flow within PEH devices, three PEH devices were taken as examples for studying the quantitative relation among different branches of energy flow. In addition, three factors were defined to evaluate of the two functions of energy harvesting, energy dissipation, and their combined effect on structural damping. Besides the evaluation on the performances of these three aspects, this understanding is crucial for specifying the target of PEH devices; while the quantitative studies are necessary towards harvesting power optimization.

The second issue from the systematic point of view is the dynamics of the overall electromechanical system. By converting both the mechanical and electrical parts into the uniform of equivalent impedance, it was managed to model an entire PEH device into equivalent impedance network, with which the power analysis is possible to be carried out. Unlike the ordinary impedance network, the impedance values of some components in the network are constrained, rather than can be arbitrarily set. This feature should be taken into consideration when utilizing the maximum power transfer theorem for power optimization. The impedance based analysis also allowed the clarification on some ambiguities on the design and optimization of PEH devices. Based on the impedance method, the difference on power harvesting performances under displacement and base excitations were also investigated.

Most of the previous studies emphasized the important role of the piezoelectric coupling coefficient for improving PEH. On the other hand, it has been shown that the harvesting performance can be improved significantly by implementing the switching interface circuits. Based on the systematic investigations on the energy flow and equivalent impedance network, the contributions and relations of the mechanical structure, coupling coefficient and interface circuit towards harvesting power improvement in PEH devices were able to be further quantified. These analyses provided a deep insight on the effect of all parts in the system, and hopefully can facilitate the further development of PEH devices.

Besides showing the benefits of switching interface circuits over harvesting improvement, some issues on their practical implementation were also investigated in this thesis. The experimentally observed phenomenon on voltage reversion after every inversion was described. This phenomenon was caused by the dielectric loss of piezoelectric materials. A modified model was proposed to evaluate the effect of this loss. It has been shown that the lossy nature of piezoelectric element induced a small degradation on the effective voltage inversion. This degradation, although small, decreases the magnitude of the voltage across the piezoelectric element and also the harvesting power a lot. Therefore, besides the coupling coefficient, the dielectric loss is another important characteristic of piezoelectric materials that influences the PEH process, in particular, when switching interface circuits are utilized.

How to effectively implement the synchronization and switching control is another importance determining whether this technique can be widely used in practical PEH systems. An improved self-powered switching interface circuit with better isolation among different units and less dissipative components was proposed. This circuit makes use of the information carried by the piezoelectric voltage for synchronization and powers the switching components with the harvested power. The performance between the self-powered switching interface circuit and the standard energy harvesting (SEH) interface circuit, as well as the difference between the self-powered and ordinary switching interfaces were investigated. It has been shown that the larger the vibration magnitude, the more beneficial to replace the SEH with the self-powered switching interface.

In the future work, one task is to construct the comprehensive design procedures of

impedance matched PEH devices by taking all the effects of mechanical structure, piezoelectric material, and interface circuit into consideration. Second is the integration of self-powered PEH devices with intelligent sensing and processing systems.

□ End of chapter.

Appendix A

Derivations

A.1 Voltage Inversion in Double Capacitors RLC Circuit

Given a switching RLC circuit composed of two capacitors, e.g., C_1 and C_2 as shown in Figure A.1(a). The switch is off most of the time. At the zero instant, the switch takes action to invert the voltage across C_1. Denoting the voltages across C_1 before and after inversion as $V_{1,org}$ and $V_{1,end}$, and those across C_2 as $V_{2,org}$ and $V_{2,end}$, the two capacitors can be combined and taken equivalence as a capacitor $C = C_1C_2/(C_1 + C_2)$, whose initial and end voltages are $V_{1,org} - V_{2,org}$ and $V_{1,end} - V_{2,end}$, respectively. The equivalent circuit is illustrated in Figure A.1(b). Two equations can be obtained considering the relations on inversion and the

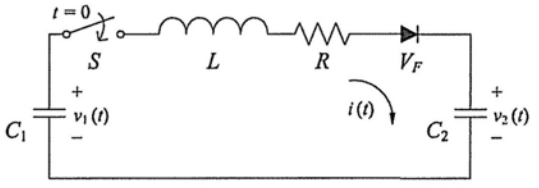

(a)

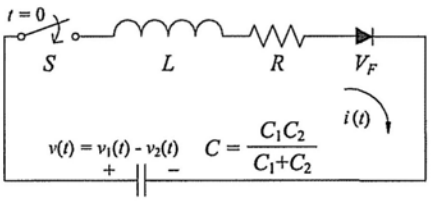

(b)

Figure A.1: Double capacitor RLC circuit. (a) Original. (b) Equivalence.

unchanging total charge, i.e.,

$$\begin{cases} V_{1,end} - V_{2,end} - V_F = \gamma(V_{1,org} - V_{2,org} - V_F) \\ C_1(V_{1,org} - V_{1,end}) + C_2(V_{2,org} - V_{2,end}) = 0 \end{cases} \tag{A.1}$$

Solving the equations gives the expression on the end voltages across C_1 and C_2

$$\begin{cases} V_{1,end} = \dfrac{(C_1 + \gamma C_2)V_{1,org} + C_2(1-\gamma)V_{2,org} + C_2(1-\gamma)V_F}{C_1 + C_2} \\ \\ V_{2,end} = \dfrac{C_1(1-\gamma)V_{1,org} + (\gamma C_1 + C_2)V_{2,org} - C_1(1-\gamma)V_F}{C_1 + C_2} \end{cases} \tag{A.2}$$

The inversion factor is related to the original voltages as well as the characteristic of the RLC circuit.

$$\gamma = \begin{cases} -e^{-\pi/(2Q)}, & V_{1,org} > V_{2,org} + V_F\,; \\ 1, & \text{others} \end{cases} \tag{A.3}$$

where Q is the quality factor of the RLC circuit.

$$\begin{aligned} Q &= \frac{1}{R}\sqrt{\frac{L}{C}} \\ &= \frac{1}{R}\sqrt{\frac{L(C_1 + C_2)}{C_1 C_2}} \end{aligned} \tag{A.4}$$

□ End of chapter.

Bibliography

Adhikari, S., Friswell, M. I. and Inman, D. J. 2009, "Piezoelectric energy harvesting from broadband random vibrations," *Smart Mater. Struct.*, **18**(11), 115005.

Ajitsaria, J., Choe, S. Y., Shen, D. and Kim, D. J. 2007, "Modeling and analysis of a bimorph piezoelectric cantilever beam for voltage generation," *Smart Mater. Struct.*, **16**(2), 447.

Anton, S. R., Erturk, A., Kong, N., Ha, D. S. and Inman, D. J. 2009, "Self-charging structures using piezoceramics and thin-film batteries," *in: Proceedings of the ASME 2009 Conference on Smart Materials, Adaptive Structures and Intelligent Systems.*

Anton, S. R. and Sodano, H. A. 2007, "A review of power harvesting using piezoelectric materials (2003-2006)," *Smart Mater. Struct.*, **16**(3), R1–R21.

Arnold, D. 2007, "Review of microscale magnetic power generation," *IEEE Trans. Magn.*, **43**(11), 3940–3951.

Badel, A., Benayad, A., Lefeuvre, E., Lebrun, L., Richard, C. and Guyomar, D. 2006, "Single crystals and nonlinear process for outstanding vibration-powered electrical generators," *IEEE Trans. Ultrason. Ferroelectr. Freq. Control*, **53**(4), 673–684.

Badel, A., Guyomar, D., Lefeuvre, E. and Richard, C. 2005, "Efficiency enhancement of a piezoelectric energy harvesting device in pulsed operation by synchronous charge inversion," *J. Intell. Mater. Syst. Struct.*, **16**(10), 889–901.

Barton, D. A. W., Burrow, S. G. and Clare, L. R. 2010, "Energy harvesting from vibrations with a nonlinear oscillator," *J. Vib. Acoust.*, **132**(2), 021009.

Beeby, S. P., Tudor, M. J. and White, N. M. 2006, "Energy harvesting vibration sources for microsystems applications," *Meas. Sci. Technol.*, **17**(12), R175–R195.

Bogue, R. 2009, "Energy harvesting and wireless sensors: a review of recent developments," *Sensor Review*, **29**(3), 194 – 199.

Brufau-Penella, J. and Puig-Vidal, M. 2009, "Piezoelectric energy harvesting improvement with complex conjugate impedance matching," *J. Intell. Mater. Syst. Struct.*, **20**(5), 597–608.

Cammarano, A., Burrow, S. G., Barton, D. A. W., Carrella, A. and Clare, L. R. 2010, "Tuning a resonant energy harvester using a generalized electrical load," *Smart Mater. Struct.*, **19**(5), 055003.

CATRENE 2009, *Energy autonomous systems: future trends in devices, technology, and systems*, Technical report, CATRENE (Cluster for Application and Technology Research in Europe on NanoElectronics).

Challa, V. R., Prasad, M. G., Shi, Y. and Fisher, F. T. 2008, "A vibration energy harvesting device with bidirectional resonance frequency tunability," *Smart Materials and Structures*, **17**(1), 015035.

Clark, W. W. 2000, "Vibration control with state-switched piezoelectric materials," *J. Intell. Mater. Syst. Struct.*, **11**(4), 263–271.

Cook-Chennault, K. A., Thambi, N. and Sastry, A. M. 2008, "Powering MEMS portable devices – a review of non-regenerative and regenerative power supply systems with special emphasis on piezoelectric energy harvesting systems," *Smart Mater. Struct.*, **17**(4), 043001.

Cremer, L., Heckl, M. and Petersson, B. 2005, *Structure-Borne Sound: Structural Vibrations and Sound Radiation at Audio Frequencies*, Springer-Verlag Berlin Heidelberg.

de Silva, C. W. 2005, *Vibration and Shock Handbook*, CRC Press.

Donelan, J. M., Li, Q., Naing, V., Hoffer, J. A., Weber, D. J. and Kuo, A. D. 2008, "Biomechanical energy harvesting: Generating electricity during walking with minimal user effort," *Science*, **319**(5864), 807–810.

Dutoit, N. E., Wardle, B. L. and Kim, S.-G. 2005, "Design considerations for mems-scale piezoelectric mechanical vibration energy harvesters," *Integr. Ferroelectr.*, **71**(1), 121–160.

Elvin, N. G. and Elvin, A. A. 2009*a*, "A coupled finite element–circuit simulation model for analyzing piezoelectric energy generators," *J. Intell. Mater. Syst. Struct.*, **20**(5), 587–595.

Elvin, N. G. and Elvin, A. A. 2009*b*, "A general equivalent circuit model for piezoelectric generators," *J. Intell. Mater. Syst. Struct.*, **20**(1), 3–9.

Elvin, N. G., Elvin, A. A. and Spector, M. 2001, "A self-powered mechanical strain energy sensor," *Smart Mater. Struct.*, **10**(2), 293.

Erturk, A., Hoffmann, J. and Inman, D. J. 2009, "A piezomagnetoelastic structure for broadband vibration energy harvesting," *Appl. Phys. Lett.*, **94**(25), 254102 –254102–3.

Erturk, A. and Inman, D. 2008*a*, "On mechanical modeling of cantilevered piezoelectric vibration energy harvesters," *J. Intell. Mater. Syst. Struct.*, **19**(11), 1311–1325.

Erturk, A. and Inman, D. J. 2008*b*, "A distributed parameter electromechanical model for cantilevered piezoelectric energy harvesters," *J. Vib. Acoust.*, **130**(4), 041002.

Erturk, A. and Inman, D. J. 2008*c*, "Issues in mathematical modeling of piezoelectric energy harvesters," *Smart Mater. Struct.*, **17**(6), 065016.

Erturk, A., Renno, J. M. and Inman, D. J. 2009, "Modeling of piezoelectric energy harvesting from an L-shaped beam-mass structure with an application to UAVs," *J. Intell. Mater. Syst. Struct.*, **20**(5), 529–544.

Feenstra, J., Granstrom, J. and Sodano, H. 2008, "Energy harvesting through a backpack employing a mechanically amplified piezoelectric stack," *Mech. Syst. Sig. Process.*, **22**(3), 721 – 734.

Ferrari, M., Ferrari, V., Guizzetti, M., Ando, B., Baglio, S. and Trigona, C. 2009, "Improved energy harvesting from wideband vibrations by nonlinear piezoelectric converters," *Procedia Chemistry*, **1**(1), 1203 – 1206.

Gilbert, J. and Balouchi, F. 2008, "Comparison of energy harvesting systems for wireless sensor networks," *Int. J. Autom. Comput.*, **5**(4), 334–347.

Granstrom, J., Feenstra, J., Sodano, H. A. and Farinholt, K. 2007, "Energy harvesting from a backpack instrumented with piezoelectric shoulder straps," *Smart Mater. Struct.*, **16**(5), 1810.

Guan, M. J. and Liao, W. H. 2007, "On the efficiencies of piezoelectric energy harvesting circuits towards storage device voltages," *Smart Mater. Struct.*, **16**(2), 498–505.

Guan, M. J. and Liao, W. H. 2009, "On the equivalent circuit models of piezoelectric ceramics," *Ferroelectrics*, **386**(1), 77–87.

Guan, M. and Liao, W. 2008, "Characteristics of energy storage devices in piezoelectric energy harvesting systems," *J. Intell. Mater. Syst. Struct.*, **19**(6), 671–680.

Guigon, R., Chaillout, J.-J., Jager, T. and Despesse, G. 2008*a*, "Harvesting raindrop energy: experimental study," *Smart Mater. Struct.*, **17**(1), 015039.

Guigon, R., Chaillout, J.-J., Jager, T. and Despesse, G. 2008*b*, "Harvesting raindrop energy: theory," *Smart Mater. Struct.*, **17**(1), 015038.

Guyomar, D. and Badel, A. 2006, "Nonlinear semi-passive multimodal vibration damping: An efficient probabilistic approach," *J. Sound Vib.*, **294**(1-2), 249–268.

Guyomar, D., Badel, A., Lefeuvre, E. and Richard, C. 2005, "Toward energy harvesting using active materials and conversion improvement by nonlinear processing," *IEEE Trans. Ultrason. Ferroelectr. Freq. Control*, **52**(4), 584–595.

Guyomar, D., Sebald, G., Pruvost, S., Lallart, M., Khodayari, A. and Richard, C. 2009, "Energy harvesting from ambient vibrations and heat," *J. Intell. Mater. Syst. Struct.*, **20**(5), 609–624.

Guyomar, D., Yuse, K., Monnier, T., Petit, L., Lefeuvre, E. and Richard, C. 2006, "Semi-passive vibration control: principle and application," *Annals of the University of Craiova, Electrical Engineering series*, (30), 57–62.

Hagood, N. W. and von Flotow, A. 1991, "Damping of structural vibrations with piezoelectric materials and passive electrical networks," *J. Sound Vib.*, **146**(2), 243–268.

Halvorsen, E. 2008, "Energy harvesters driven by broadband random vibrations," *J. Microelectromech. Syst.*, **17**(5), 1061–1071.

Hamza, R. and Robin, L. 2009, *MEMS energy harvesting devices, technologies and markets*, Technical report, Yole Development.

Harris, C. M. 1996, *Shock and Vibration Handbook*, McGraw-Hill.

Hirose, S., Aoyagi, M. and Tomikawa, Y. 1993, "Dielectric loss in a piezoelectric ceramic transducer under high-power operation; increase of dielectric loss and its influence on transducer efficiency," *Jpn. J. Appl. Phys.*, **32**(5B), 2418–2421.

Howells, C. A. 2009, "Piezoelectric energy harvesting," *Energy Convers. Manage.*, **50**(7), 1847 – 1850.

Hu, Y., Xue, H. and Hu, H. 2007, "A piezoelectric power harvester with adjustable frequency through axial preloads," *Smart Mater. Struct.*, **16**(5), 1961.

Hu, Y., Xue, H., Hu, T. and Hu, H. 2008, "Nonlinear interface between the piezoelectric harvesting structure and the modulating circuit of an energy harvester with a real storage battery," *IEEE Trans. Ultrason. Ferroelectr. Freq. Control*, **55**(1), 148–160.

Hu, Y., Xue, H., Yang, J. and Jiang, Q. 2006, "Nonlinear behavior of a piezoelectric power harvester near resonance," *IEEE Trans. Ultrason. Ferroelectr. Freq. Control*, **53**(7), 1387 – 1391.

Hudak, N. S. and Amatucci, G. G. 2008, "Small-scale energy harvesting through thermoelectric, vibration, and radiofrequency power conversion," *J. Appl. Phys.*, **103**(10), 101301.

IEEE Standard on Piezoelectricity 1988*ANSI/IEEE Std, 176-1987*, .

Jeong, S.-J., Kim, M.-S., Lee, D.-S. and Song, J.-S. 2008, "Properties of a multi-stack type piezoelectric energy harvesting device," *Integr. Ferroelectr.*, **98**(1), 208–215.

Jia, D. and Liu, J. 2009, "Human power-based energy harvesting strategies for mobile electronic devices," *Front. Energy Power Eng. Chin.*, **3**(1), 27–46.

Khaligh, A., Zeng, P. and Zheng, C. 2010, "Kinetic energy harvesting using piezoelectric and electromagnetic technologies – state of the art," *IEEE Trans. Ind. Electron.*, **57**(3), 850 –860.

Kim, H., Priya, S., Stephanou, H. and Uchino, K. 2007, "Consideration of impedance matching techniques for efficient piezoelectric energy harvesting," *IEEE Trans. Ultrason. Ferroelectr. Freq. Control*, **54**(9), 1851–1859.

Kong, N., Ha, D. S., Erturk, A. and Inman, D. J. 2010, "Resistive impedance matching circuit for piezoelectric energy harvesting," *J. Intell. Mater. Syst. Struct.*, doi:10.1177/1045389X09357971.

Kuo, A. D. 2005, "Harvesting energy by improving the economy of human walking," *Science*, **309**(5741), 1686–1687.

Kymissis, J., Kendall, C., Paradiso, J. and Gershenfeld, N. 1998, "Parasitic power harvesting in shoes," *in: Second International Symposium on Wearable Computers, 1998*, pp. 132–139.

Lallart, M., Garbuio, L., Richard, C. and Guyomar, D. 2010, "Low-cost capacitor voltage inverter for outstanding performance in piezoelectric energy harvesting," *IEEE Trans. Ultrason. Ferroelectr. Freq. Control*, **57**(2), 281 – 291.

Lallart, M. and Guyomar, D. 2008, "An optimized self-powered switching circuit for non-linear energy harvesting with low voltage output," *Smart Mater. Struct.*, **17**(3), 035030.

Lallart, M., Inman, D. J. and Guyomar, D. 2010, "Transient performance of energy harvesting strategies under constant force magnitude excitation," *J. Intell. Mater. Syst. Struct.*, doi: 10.1177/1045389X09358334.

Lefeuvre, E., Badel, A., Petit, L., Richard, C. and Guyomar, D. 2006, "Semi-passive piezoelectric structural damping by synchronized switching on voltage sources," *J. Intell. Mater. Syst. Struct.*, **17**(8-9), 653–660.

Lefeuvre, E., Badel, A., Richard, C. and Guyomar, D. 2007, "Energy harvesting using piezoelectric materials: Case of random vibrations," *J. Electroceram.*, **19**(4), 349–355.

Lefeuvre, E., Badel, A., Richard, C., Petit, L. and Guyomar, D. 2006, "A comparison between several vibration-powered piezoelectric generators for standalone systems," *Sens. Actuators, A*, **126**(2), 405 – 416.

Leland, E. S. and Wright, P. K. 2006, "Resonance tuning of piezoelectric vibration energy scavenging generators using compressive axial preload," *Smart Mater. Struct.*, **15**(5), 1413.

Lesieutre, G. A. and Christopher L. Davis, L. 1997, "Can a coupling coefficient of a piezoelectric device be higher than those of its active material?," *in: Smart Structures and Materials 1997: Smart Structures and Integrated Systems*, Vol. 3041, SPIE, pp. 281–292.

Lesieutre, G. A., Ottman, G. K. and Hofmann, H. F., L. 2004, "Damping as a result of piezoelectric energy harvesting," *J. Sound Vib.*, **269**(3-5), 991–1001.

Liang, J. and Liao, W.-H. 2009*a*, "An improved self-powered switching interface for piezoelectric energy harvesting," *in: Proc. International Conference on Information and Automation 2009*, pp. 945–950.

Liang, J. and Liao, W.-H. 2009*b*, "On the influence of dielectric loss in piezoelectric energy harvesting with SSHI interface," *in: Procceding of the 20th International Conference on Adaptive Structures and Technologies*.

Liang, J. and Liao, W.-H. 2010*a*, "Impedance analysis for piezoelectric energy harvesting devices under different excitations," *in: Proc. International Conference on Information and Automation 2010*, pp. 42 – 47.

Liang, J. and Liao, W.-H. 2010*b*, "Impedance matching for improving piezoelectric energy harvesting systems," *in: Active and Passive Smart Structures and Integrated Systems 2010, SPIE*, number 7643.

Liang, J. R. and Liao, W. H. 2009*c*, "Piezoelectric energy harvesting and dissipation on structural damping," *J. Intell. Mater. Syst. Struct.*, **20**(5), 515–527.

Liao, Y. and Sodano, H. A. 2009, "Structural effects and energy conversion efficiency of power harvesting," *J. Intell. Mater. Syst. Struct.*, **20**(5), 505–514.

Lin, J.-T. and Alphenaar, B. 2009, "Enhancement of energy harvested from a random vibration source by magnetic coupling of a piezoelectric cantilever," *J. Intell. Mater. Syst. Struct.*, doi: 10.1177/1045389X09355662.

Lin, J.-T., Lee, B. and Alphenaar, B. 2010, "The magnetic coupling of a piezoelectric cantilever for enhanced energy harvesting efficiency," *Smart Mater. Struct.*, **19**(4), 045012.

Liu, W. Q., Feng, Z. H., He, J. and Liu, R. B. 2007, "Maximum mechanical energy harvesting strategy for a piezoelement," *Smart Mater. Struct.*, **16**(6), 2130–2136.

Liu, Y.-P., Vasic, D., Costa, F., Wu, W.-J. and Lee, C. K. 2009, "Velocity-controlled piezoelectric switching energy harvesting device," *in: International Conference on Renewable Energies and Power Quality 2009, ICREPQ 2009c*.

Liu, Y., Tian, G., Wang, Y., Lin, J., Zhang, Q. and Hofmann, H. F. 2009, "Active piezoelectric energy harvesting: general principle and experimental demonstration," *J. Intell. Mater. Syst. Struct.*, **20**(5), 575–585.

Makihara, K., Onoda, J. and Miyakawa, T. 2006, "Low energy dissipation electric circuit for energy harvesting," *Smart Mater. Struct.*, **15**(5), 1493–1498.

Mann, B. and Sims, N. 2009, "Energy harvesting from the nonlinear oscillations of magnetic levitation," *J. Sound Vib.*, **319**(1-2), 515 – 530.

Mateu, L. and Moll, F. 2005, "Review of energy harvesting techniques and applications for microelectronics (keynote address)," *Proc. SPIE*, **5837**(1), 359–373.

Mathuna, C. O., O'Donnell, T., Martinez-Catala, R. V., Rohan, J. and O'Flynn, B. 2008, "Energy scavenging for long-term deployable wireless sensor networks," *Talanta*, **75**(3), 613 – 623.

Mitcheson, P. D., Reilly, E. K., Toh, T., Wright, P. K. and Yeatman, E. M. 2007, "Performance limits of the three MEMS inertial energy generator transduction types," *J. Micromech. Microeng.*, **17**(9), S211.

Mitcheson, P. D., Yeatman, E. M., Rao, G. K., Holmes, A. S. and Green, T. C. 2008, "Energy harvesting from human and machine motion for wireless electronic devices," *Proc. IEEE*, **96**(9), 1457–1486.

Mitcheson, P., Green, T., Yeatman, E. and Holmes, A. 2004, "Architectures for vibration-driven micropower generators," *J. Microelectromech. Syst.*, **13**(3), 429 – 440.

Mo, C., Radziemski, L. J. and Clark, W. W. 2010, "Analysis of piezoelectric circular diaphragm energy harvesters for use in a pressure fluctuating system," *Smart Mater. Struct.*, **19**(2), 025016.

Moheimani, S. 2003, "A survey of recent innovations in vibration damping and control using shunted piezoelectric transducers," *IEEE Trans. Control Syst. Technol.*, **11**(4), 482–494.

Nakano, K., Elliott, S. J. and Rustighi, E. 2007, "A unified approach to optimal conditions of power harvesting using electromagnetic and piezoelectric transducers," *Smart Mater. Struct.*, **16**(4), 948.

Neubauer, M., Krack, M. and Wallaschek, J. 2010, "Parametric studies on the harvested energy of piezoelectric switching techniques," *Smart Mater. Struct.*, **19**(2), 025001.

Ng, T. H. and Liao, W. H. 2005, "Sensitivity analysis and energy harvesting for a self-powered piezoelectric sensor," *J. Intell. Mater. Syst. Struct.*, **16**(10), 785–797.

ON Semiconductor 2008, *TIP31C, TIP32C Datasheet*, Technical report, ON Semiconductor.

Op het Veld, B., Hohlfeld, D. and Pop, V. 2009, "Harvesting mechanical energy for ambient intelligent devices," *Inf. Syst. Front.*, **11**(1), 7–18.

Ottman, G., Hofmann, H., Bhatt, A. and Lesieutre, G.A., L. 2002, "Adaptive piezoelectric energy harvesting circuit for wireless remote power supply," *IEEE Trans. Power Electron.*, **17**(5), 669–676.

Ottman, G., Hofmann, H. and Lesieutre, G.A., L. 2003, "Optimized piezoelectric energy harvesting circuit using step-down converter in discontinuous conduction mode," *IEEE Trans. Power Electron.*, **18**(2), 696–703.

Paganelli, R. P., Romani, A., Golfarelli, A., Magi, M., Sangiorgi, E. and Tartagni, M. 2010, "Modeling and characterization of piezoelectric transducers by means of scattering parameters. part i: Theory," *Sens. Actuators, A*, **In Press**.

Paradiso, J. A. and Feldmeier, M. 2001, "A compact, wireless, self-powered pushbutton controller," *in: Ubicomp 2001: Ubiquitous Computing," ACM UBICOMP Conference Proceedings*, Springer-Verlag Berlin Heidelberg, pp. 299–304.

Paradiso, J. A. and Starner, T. 2005, "Energy scavenging for mobile and wireless electronics," *IEEE Pervasive Comput.*, **4**(1), 18–27.

Penella, M. and Gasulla, M. 2007, "A review of commercial energy harvesters for autonomous sensors," *in: Proceedings of IEEE Instrumentation and Measurement Technology Conference 2007*, pp. 1 –5.

Peters, C., Maurath, D., Schock, W., Mezger, F. and Manoli, Y. 2009, "A closed-loop wide-range tunable mechanical resonator for energy harvesting systems," *J. Micromech. Microeng.*, **19**(9), 094004 (9pp).

Priya, S. 2007, "Advances in energy harvesting using low profile piezoelectric transducers," *J. Electroceram.*, **19**(1), 167–184.

Priya, S. and Inman, D. J. 2009, *Energy harvesting technologies*, Springer, New York; London.

Qi, Y., Jafferis, N. T., Lyons, K., Lee, C. M., Ahmad, H. and McAlpine, M. C. 2010, "Piezoelectric ribbons printed onto rubber for flexible energy conversion," *Nano Lett.*, **10**(2), 524–528.

Qiu, J., Jiang, H., Ji, H. and Zhu, K. 2009, "Comparison between four piezoelectric energy harvesting circuits," *Front. Mech. Eng. Chin.*, **4**(2), 153–159.

Ramadass, Y. and Chandrakasan, A. 2010, "An efficient piezoelectric energy harvesting interface circuit using a bias-flip rectifier and shared inductor," *IEEE J. Solid-State Circuits*, **45**(1), 189 –204.

Ren, K., Liu, Y., Geng, X., Hofmann, H. and Zhang, Q. 2006, "Single crystal pmn-pt/epoxy 1-3 composite for energy-harvesting application," *IEEE Trans. Ultrason. Ferroelectr. Freq. Control*, **53**(3), 631 – 638.

Renaud, M., Fiorini, P. and van Hoof, C. 2007, "Optimization of a piezoelectric unimorph for shock and impact energy harvesting," *Smart Mater. Struct.*, **16**(4), 1125–1135.

Renaud, M., Fiorini, P., van Schaijk, R. and van Hoofr, C. 2009, "Harvesting energy from the motion of human limbs: the design and analysis of an impact-based piezoelectric generator," *Smart Mater. Struct.*, **18**(3), 035001.

Renno, J. M., Daqaq, M. F. and Inman, D. J. 2009, "On the optimal energy harvesting from a vibration source," *J. Sound Vib.*, **320**(1-2), 386 – 405.

Richard, C., Guyomar, D., Audigier, D. and Bassaler, H. 2000, Vol. 3989, SPIE, pp. 288–299.

Richards, C. D., Anderson, M. J., Bahr, D. F. and Richards, R. F. 2004, "Efficiency of energy conversion for devices containing a piezoelectric component," *J. Micromech. Microeng.*, **14**(5), 717.

Rodig, T., Schonecker, A. and Gerlach, G. 2010, "A survey on piezoelectric ceramics for generator applications," *J. Am. Ceram. Soc.*, **93**(4), 901–912.

Rome, L. C., Flynn, L., Goldman, E. M. and Yoo, T. D. 2005, "Generating electricity while walking with loads," *Science*, **309**(5741), 1725–1728.

Roundy, S., Wright, P. K. and Rabaey, J. M. 2004, *Energy scavenging for wireless sensor networks :with special focus on vibrations*, Kluwer Academic, Boston.

Roundy, Shad, W. 2005, "On the effectiveness of vibration-based energy harvesting," *J. Intell. Mater. Syst. Struct.*, **16**(10), 809–823.

Sanders, S., Noworolski, J., Liu, X. and Verghese, G. 1991, "Generalized averaging method for power conversion circuits," *IEEE Trans. Power Electron.*, **6**(2), 251 –259.

Scruggs, J. 2009, "An optimal stochastic control theory for distributed energy harvesting networks," *J. Sound Vib.*, **320**(4-5), 707 – 725.

Scruggs, J. T. 2010, "On the causal power generation limit for a vibratory energy harvester in broadband stochastic response," *J. Intell. Mater. Syst. Struct.*, doi: 10.1177/1045389X10361794.

Shenck, N. and Paradiso, J. 2001, "Energy scavenging with shoe-mounted piezoelectrics," *IEEE Micro*, **21**(3), 30 –42.

Shu, Y. C. and Lien, I. C. 2006*a*, "Analysis of power output for piezoelectric energy harvesting systems," *Smart Mater. Struct.*, **15**(6), 1499–1512.

Shu, Y. C. and Lien, I. C. 2006*b*, "Efficiency of energy conversion for a piezoelectric power harvesting system," *J. Micromech. Microeng.*, **16**(11), 2429.

Shu, Y. C., Lien, I. C. and Wu, W. J. 2007, "An improved analysis of the SSHI interface in piezoelectric energy harvesting," *Smart Mater. Struct.*, **16**(6), 2253–2264.

Sodano, H. A., Inman, D. J. and Park, G. 2004, "A review of power harvesting from vibration using piezoelectric materials," *Shock Vib. Digest*, **36**(3), 197–205.

Sodano, H. A., Inman, D. J. and Park, G. 2005*a*, "Comparison of piezoelectric energy harvesting devices for recharging batteries," *J. Intell. Mater. Syst. Struct.*, **16**(10), 799–807.

Sodano, H. A., Inman, D. J. and Park, G. 2005*b*, "Generation and storage of electricity from power harvesting devices," *J. Intell. Mater. Syst. Struct.*, **16**(1), 67–75.

Sodano, H. A., Park, G. and Inman, D. J. 2004, "An investigation into the performance of macro-fiber composites for sensing and structural vibration applications," *Mech. Syst. Sig. Process.*, **18**(3), 683 – 697.

Song, H. J., Choi, Y. T., Wang, G. and Wereley, N. M. 2009, "Energy harvesting utilizing single crystal pmn-pt material and application to a self-powered accelerometer," *J. Mech. Des.*, **131**(9), 091008.

Song, H. J., Choi, Y.-T., Wereley, N. M. and Purekar, A. S. 2010, "Energy harvesting devices using macro-fiber composite materials," *J. Intell. Mater. Syst. Struct.*, doi: 10.1177/1045389X10361633.

Stanton, S. C., McGehee, C. C. and Mann, B. P. 2009, "Reversible hysteresis for broadband magnetopiezoelastic energy harvesting," *Appl. Phys. Lett.*, **95**(17), 174103 –174103–3.

Stanton, S. C., McGehee, C. C. and Mann, B. P. 2010, "Nonlinear dynamics for broadband energy harvesting: Investigation of a bistable piezoelectric inertial generator," *Physica D*, **239**(10), 640 – 653.

Starner, T. 1996, "Human-powered wearable computing," *IBM Syst. J.*, **35**, 618 – 628.

Stephen, N. 2006*a*, "On energy harvesting from ambient vibration," *J. Sound Vib.*, **293**(1-2), 409 – 425.

Stephen, N. 2006*b*, "On the maximum power transfer theorem within electromechanical systems," *Proc. Inst. Mech. Eng. Part C J. Mech. Eng. Sci.*, **220**(8), 1261–1267.

Sun, C., Qin, L., Li, F. and Wang, Q.-M. 2009, "Piezoelectric energy harvesting using single crystal Pb(Mg1/3Nb2/3)O 3-xPbTiO3 (PMN-PT) device," *J. Intell. Mater. Syst. Struct.*, **20**(5), 559–568.

Tan, Y., Hoe, K. and Panda, S. 2006, "Energy harvesting using piezoelectric igniter for self-powered radio frequency (RF) wireless sensors," *in: IEEE International Conference on Industrial Technology 2006*, pp. 1711–1716.

Taylor, G., Burns, J., Kammann, S., Powers, W. and Welsh, T. 2001, "The energy harvesting eel: a small subsurface ocean/river power generator," *IEEE J. Oceanic Eng.*, **26**(4), 539–547.

Thomas, J. P., Qidwai, M. A. and Kellogg, J. C. 2006, "Energy scavenging for small-scale unmanned systems," *J. Power Sources*, **159**(2), 1494 – 1509.

Triplett, A. and Quinn, D. D. 2009, "The effect of non-linear piezoelectric coupling on vibration-based energy harvesting," *J. Intell. Mater. Syst. Struct.*, **20**(16), 1959–1967.

Umeda, M., Nakamura, K. and Ueha, S. 1996, "Analysis of the transformation of mechanical impact energy to electric energy using piezoelectric vibrator," *Jpn. J. Appl. Phys.*, **35**(Part 1, No. 5B), 3267–3273.

Umeda, M., Nakamura, K. and Ueha, S. 1997, "Energy storage characteristics of a piezo-generator using impact induced vibration," *Jpn. J. Appl. Phys.*, **36**(Part 1, No. 5B), 3146–3151.

Umeda, M., Nakamura, K. and Ueha, S. 1998, "The measurement of high-power characteristics for a piezoelectric transducer based on the electrical transient response," *Jpn. J. Appl. Phys.*, **37**(9B), 5322–5325.

Wang, D.-A. and Ko, H.-H. 2010, "Piezoelectric energy harvesting from flow-induced vibration," *J. Micromech. Microeng.*, **20**(2), 025019.

Wang, Z., Hu, J., Suryavanshi, A. P., Yum, K. and Yu, M.-F. 2007, "Voltage generation from individual batio3 nanowires under periodic tensile mechanical load," *Nano Lett.*, **7**(10), 2966–2969.

Wang, Z. L. and Song, J. 2006, "Piezoelectric nanogenerators based on zinc oxide nanowire arrays," *Science*, **312**(5771), 242–246.

Warkentin, D. J. and Hagood, N. W. 1997, "Nonlinear piezoelectric shunting for structural damping," *in: Smart Structures and Materials 1997: Smart Structures and Integrated Systems*, Vol. 3041, SPIE, pp. 747–757.

Wickenheiser, A., Reissman, T., Wu, W.-J. and Garcia, E. 2010, "Modeling the effects of electromechanical coupling on energy storage through piezoelectric energy harvesting," *IEEE/ASME Trans. Mechatron.*, **15**(3), 400 –411.

Wikipedia , **URL:** *http://en.wikipedia.org/wiki/Dissipation*

Williams, C. B. and Yates, R. B. 1996, "Analysis of a micro-electric generator for microsystems," *Sens. Actuators, A*, **52**(1-3), 8 – 11.

Wong, S.-C. and Brown, A. 1995, "Analysis, modeling, and simulation of series-parallel resonant converter circuits," *IEEE Trans. Power Electron.*, **10**(5), 605 –614.

Wu, W. J., Wickenheiser, A. M., Reissman, T. and Garcia, E. 2009, "Modeling and experimental verification of synchronized discharging techniques for boosting power harvesting from piezoelectric transducers," *Smart Mater. Struct.*, **18**(5), 055012.

Xue, H., Hu, Y. and ming Wang, Q. 2008, "Broadband piezoelectric energy harvesting devices using multiple bimorphs with different operating frequencies," *IEEE Trans. Ultrason. Ferroelectr. Freq. Control*, **55**(9), 2104–2108.

Yang, Y. and Tang, L. 2009, "Equivalent circuit modeling of piezoelectric energy harvesters," *J. Intell. Mater. Syst. Struct.*, **20**(18), 2223–2235.

Yang, Y., Tang, L. and Li, H. 2009, "Vibration energy harvesting using macro-fiber composites," *Smart Mater. Struct.*, **18**(11), 115025.

Yang, Z. and Yang, J. 2009, "Connected vibrating piezoelectric bimorph beams as a wideband piezoelectric power harvester," *J. Intell. Mater. Syst. Struct.*, **20**(5), 569–574.

Yoon, H.-S., Washington, G. and Danak, A. 2005, "Modeling, optimization, and design of efficient initially curved piezoceramic unimorphs for energy harvesting applications," *J. Intell. Mater. Syst. Struct.*, **16**(10), 877–888.

Zhu, D., Tudor, M. J. and Beeby, S. P. 2010, "Strategies for increasing the operating frequency range of vibration energy harvesters: a review," *Meas. Sci. Technol.*, **21**(2), 022001.

Zhu, M., Worthington, E. and Njuguna, J. 2009, "Analyses of power output of piezoelectric energy-harvesting devices directly connected to a load resistor using a coupled piezoelectric-circuit finite element method," *IEEE Trans. Ultrason. Ferroelectr. Freq. Control*, **56**(7), 1309–1317.